Evaluation of a Radial Flux Air-cored Permanent Magnet Machine Drive with Manual Transmission Drivetrain for Electric Vehicles

by

David Jordaan Groenewald

Thesis presented in partial fulfilment of the requirements for the degree of Master of Science in Engineering at Stellenbosch University

Department of Electrical & Electronic Engineering
University of Stellenbosch,
Private Bag X1, 7602 Matieland, South Africa.

Supervisor: Prof. M.J. Kamper

December 2010

Declaration

By submitting this thesis electronically, I declare that the entirety of the work contained therein is my own, original work, that I am the owner of the copyright thereof (unless to the extent explicitly otherwise stated) and that I have not previously in its entirety or in part submitted it for obtaining any qualification.

Date: .....

Abstract

Due to finite oil resources and its political and economical impact, a renewed interest in energy independence has compelled industry and government to pursue electric vehicle designs. The current worldwide research that is being conducted on drivetrain topologies for EVs, focus mainly on direct in-wheel drive, direct differential drive and fixed-gear differential drive topologies. Furthermore, the control strategy for these type of motor drives require a, so called, field-weakening operation in order to achieve acceptable performance characteristics for the vehicle.

This thesis evaluates the use of a manual gearbox drivetrain topology and a radial flux air-cored permanent magnet (RFAPM) synchronous machine, without flux-weakening operation, as a traction drive application for EVs. For the purpose of this research study, a 2006 model Opel Corsa Lite is converted to a battery electric vehicle, and the Corsa is renamed to the E-Corsa. The Corsa is converted so that all the original functionality, boot space and space inside the vehicle are retained. The original 5-speed manual gearbox is used as drivetrain for the vehicle and a 40 kW, 70 Nm RFAPM traction drive is developed for the manual gearbox. A power electronic converter is designed for RFAPM traction drive and a Lithium ion (Li-ion) battery pack is used as energy source for the traction drive. The battery pack is mounted partially in the front and partially in the back of the vehicle to maintain an even weight distribution in the vehicle.

Acknowledgements

I would like to express my sincere gratitude to the following...

- My promoter Prof. M.J. Kamper for his guidance, in-depth knowledge and patience throughout this project.
- Dr. Wang for his guidance and in-depth knowledge throughout this project.
- Dr. Hugo de Kock for his most admired willingness to always help and offer support.
- Mrs. Daleen Kleyn for her reliability and competence with regard to the administrative arrangements throughout this project.
- Ivan Hobbs for his help with the DSP controller and software development.
- My parents, Kobus and Maureen for their support, love and continuous encouragement.
- My sister, Edith for the love and support.

Contents

List of Figures

List of Tables

Nomenclature

Acronyms

ABC	three phase stationary reference frame
$\alpha\beta$	two axes stationary reference frame
dq	direct quadrature - synchronously rotating reference frame
FE	finite element
FEA	finite element analysis
FOC	field orientated control
EMF	electro motive force
MMF	magneto motive force
PWM	pulse width modulation
SPWM	sinusoidal pulse width modulation
SVPWM	space vector pulse width modulation
BMS	battery management system
EV	electric vehicle
BEV	battery electric vehicle
HEV	hybrid electric vehicle
ICE	internal combustion engine
PM	permanent magnet
RFPM	radial flux permanent magnet
RFAPM	radial flux air-cored permanent magnet
IGBT	insulated gate bipolar transistor
MOSFET	metal-oxide semi-conductor field effective transistor
P	proportional
PI	proportional integral
PID	proportional integral differential
THD	total harmonic distortion

Variables

i_a	instantaneous Phase A current [A]
i_b	instantaneous Phase B current [A]
i_c	instantaneous Phase C current [A]
r_s	per phase stator winding resistance [Ω]

θ_m	mechanical rotor position
ω_m	mechanical rotor speed
θ_r	electrical rotor position
ω_r	electrical rotor speed
Δ	$\frac{1}{2}$ coil side-width angle of the stator coils
r_n	nominal stator radius
p	number of pole pairs
ℓ	active length of the stator coils
ℓ_{ec}	total end-turn lenght of the stator coils
ℓ_g	airgap length
a	number of parallel circuits per phase
N	number of turns per coil
N_p	number of parallel strands per conductor
W	stator coil width
q	number of coils per phase
Q	total number of coils (Q=3q)
k_d	distribution factor
k_{pc}	pitch factor
k_f	fill factor
k_w	winding factor
K_e	end-winding factor
h	stator coil height
h_m	magnet thickness
h_y	rotor yoke thickness
B_c	fluxdensity in the iron core [T]
B_g	fluxdensity in the air core [T]
B_p	peak fluxdensity [T]
B_r	residual magnetic flux density [T]
H_c	coercive magnet field strength [A.m]
e_{coil}	induced coil voltage [V]
E_p	peak phase voltage [V]
T_m	mechanical machine torque [Nm]
T_d	developed machine torque [Nm]
T_L	load torque [N.m]
P_m	mechanical power [W]
P_e	electrical power [W]
P_{eddy}	eddy current losses [W]
I_p	peak phase current [A]
R_{cu}	resistance of a copper wire [Ω]
R_{ph}	phase resistance [Ω]
A_{cu}	area of a copper wire [mm^2]
λ_1	flux-linkage of a single turn
λ	flux-linkage
$\mu_{r_{recoil}}$	relative recoil permeability

μ_{recoil}	recoil permeability ($\mu_0\mu_{r_{recoil}}$)
ρ_{cu}	copper conductance
J	current density $[A/mm^2]$
C_1	machine constant
K_p	proportional gain
K_i	integral gain
K_d	differential gain

Constants

μ_0	permeability of free space ($4\pi \times 10^{-7}$)
Υ_{cu}	density of copper (8900 kg/m^3)
Υ_{NdFeB}	density of Neodymium Iron Boron magnets (7500 kg/m^3)
ρ_t	resistivity of copper (2.1×10^{-8})

Chapter 1

Introduction

1.1 Background

Electric vehicles (EVs) have existed for over a hundred years. When they were first invented, they immediately provided an economical and reliable means of transportation. However, electric vehicles were plagued by poor range and short-lived batteries. Today, due to finite oil resources and its political and economical impact, a renewed interest in energy independence has compelled industry and government to again pursue electric vehicle designs. Besides these economic and political aspects, there are important environmental reasons to change existing transport systems. In comparison with internal combustion vehicles, electric vehicles consume less energy for the same performance and have better ecological characteristics [1].

The ecological characteristics are related to chemical and noise pollution. Sound emission of electric vehicles can be considered to be limited to the rolling and aerodynamic noise of the vehicle, which results in a considerable reduction in noise pollution [5]. Chemical pollution is also considerably reduced, even taking into account the pollution due to electricity production necessary to recharge the batteries.

Electric vehicles have a number of challenges to overcome before they can replace the existing internal combustion engine (ICE). The introduction of electric vehicles is being delayed by the lack of cost effective batteries and manufacturing of permanent magnet synchronous motors. Current high-end battery and motor technologies are capable of providing the necessary performance for EVs. However, the success rate in terms of public acceptance will primarily depend on two factors. Either the EVs' performance and cost will equal or beat that of ICE vehicles, or the depletion of natural resources will leave the public with no other choice.

1.2 Drivetrain systems of EVs

Internal combustion engine vehicles have the engine drivetrain configuration as shown in Fig. 1.1.

Figure 1.1: Typical drivetrain configuration of ICEVs [1].

For EVs, the output characteristics of electric motors differ from those of ICEs. Typically, the electric motor eliminates the necessity for a motor to idle while at standstill, it is able to produce large torque at low speed, and it offers a wide range of speed variations. It may be possible to develop lighter, more compact and more efficient systems by taking advantage of the characteristics of electric motors. The choice of drivetrain systems in an EV mainly include: (a) propulsion mode, such as front-wheel drive, rear-wheel drive, or four-wheel drive; (b) number of electric motors in a vehicle; (c) drive approach, for instance, indirect or direct drive; and (d) number of transmission gear levels. Therefore, the possible drivetrain systems in EVs have the following six configurations [1], [6].

Conventional Type

For the conventional type of the drivetrain system in EVs, the conventional ICE is replaced by an electric motor, as shown in Fig. 1.2. This configuration does not change the typical structure of drivetrain system in ICE vehicles and hence is implemented easily.

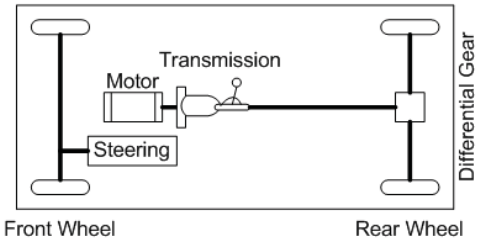

Figure 1.2: Conventional type of drivetrain system in EVs.

Transmission-less Type

The transmission-less type of drivetrain system in EVs simplifies the conventional type, as the transmission is removed. Fig. 1.3 depicts the transmission-less type of drivetrain system.

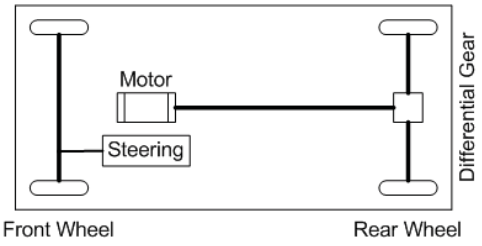

Figure 1.3: Transmission-less drivetrain system.

Cascade Type

The transmission-less type can be simplified to the differential-less type if the differential gear is removed, as illustrated in Fig. 1.4. Two motors are installed on both sides and have joints provided to transmit power to the wheels to give a function equal to the differential. This type is also regarded as the direct-drive type.

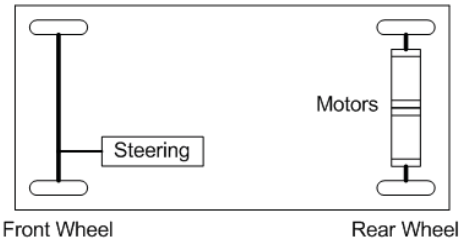

Figure 1.4: Cascade-motors drivetrain system.

In-wheel Type with Reduction Gears

This type is obtained from the simplification of the transmission-less type. Two motors are fixed to the wheel side with reduction gears provided to drive the wheels, as shown in Fig. 1.5.

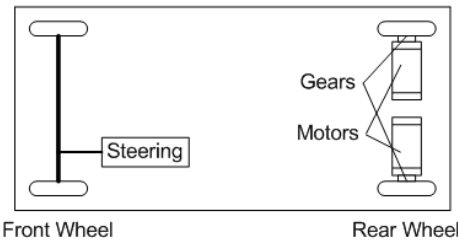

Figure 1.5: In-wheel drivetrain system with reduction gears.

In-wheel Direct-drive Type

In Fig. 1.6, electric motors are integrated into the wheels so that rotations can be caused directly without resort to a gear system. This is the direct-drive type of the in-wheel drivetrain system.

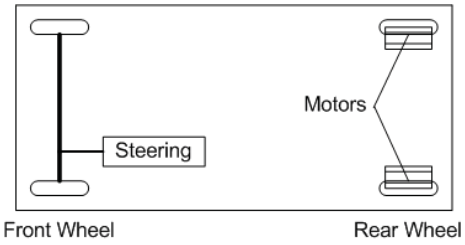

Figure 1.6: In-wheel direct-drive drivetrain system.

Four-wheel Direct-drive Type

Four in-wheel motors are used to directly drive four wheels, respectively, as shown in Fig. 1.7. It is possible that an electric steering is used to control the direction of the EV.

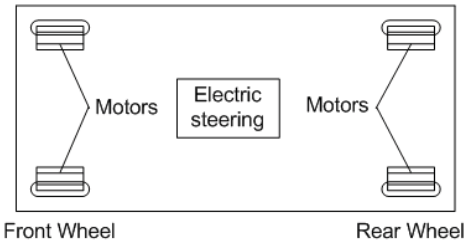

Figure 1.7: Four-wheel drivetrain system.

1.3 Conventional motor drives considered for EVs

There are four types of motor drives that are considered for EV traction drive applications. They are brushed DC motor drives, induction motor (IM) drives, permanent magnet brushless DC (PM BLDC) motor drives, and switched reluctance motor (SRM) drives.

1.3.1 Brushed DC Motor Drives

Brushed DC motors are well known for their ability to achieve high torque at low speed and their torque-speed characteristics is suitable for traction requirement [1]. Brushed DC motors can have two, four or six poles depending on the power output and voltage requirements, and may have series or shunt field windings. Separately excited DC motors are inherently suited for field-weakened operation, due to its decoupled torque and flux control characteristics, which gives the machine an extended constant power operation. However, brushed DC motor drives have a bulky construction, low efficiency, low reliability, and higher need of maintenance, mainly due to the presence of the mechanical commutator and brushes. Furthermore, friction between brushes and commutator restricts the maximum motor speed. An illustration of a typical brushed DC motor with brushes, a commutator and stator field windings is shown in Fig. 1.8.

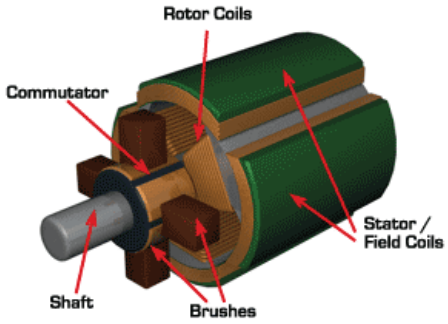

Figure 1.8: Illustration of a brushed DC motor with a wound stator.

1.3.2 Induction Motor Drives

Induction motors are of simple construction, reliability, ruggedness, low maintenance, low cost, and ability to operate in hostile environments [1]. Field orientation control (FOC) of induction motors makes it possible to decouple its torque control from field control. This allows the motor to behave in the same manner as a separately excited DC motor. This motor, however, does not suffer from the same speed limitations as with the DC motor. Extended speed range operation beyond base speed is accomplished by flux-weakening, once the motor has reached its rated power capability. However, the controllers of induction motors are at higher cost than the ones of DC motors. Furthermore, the presence of a breakdown torque limits its extended constant-power operation. In addition, efficiency at a high speed range is inherently lower than that of permanent magnet (PM) motors and switched reluctance motors (SRMs), due to rotor windings and rotor copper losses. An illustration of the rotor of a typical squirrel cage AC induction motor is shown in Fig. 1.9

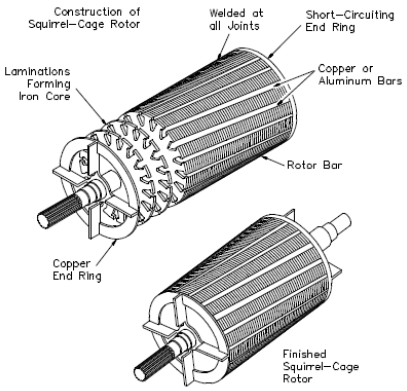

Figure 1.9: Illustration of squirrel cage rotor.

1.3.3 Permanent Magnet Brushless DC Motor Drives

PM BLDC motor drives are specifically known for their high efficiency, high power density, high overload capability, compact size, simple maintenance, regenerative features, and ease of control. Permanent magnet motors have a higher efficiency than DC motors, induction motors and SRMs [1]. PM machines are essentially synchronous machines with performance characteristics of DC shunt machines. Structurally they have three-phase windings placed upon the stator as with synchronous machines, but their rotor excitation is provided by permanent magnets instead of a field winding. This feature eliminates rotor copper losses and mechanical commutator brushes, leading to higher power densities and reduced maintenance. Fig. 1.10 shows an illustration of a typical permanent magnet brushless DC motor.

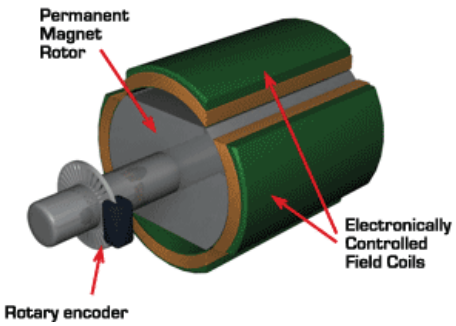

Figure 1.10: Illustration of a permanent magnet brushless DC motor.

1.3.4 Switched Reluctance Motor Drives

SRM drives are gaining much interest and are recognized to have a potential for EV applications. These motor drives have definite advantages such as simple and rugged construction, fault-tolerant operation, simple control, and outstanding torque-speed characteristics. The SRM drive has high speed operation capability with a wide constant power region. The

motor has a high starting torque and a high torque-inertia ratio. The rotor structure is extremely simple without any windings, magnets, commutators or brushes. Because of its simple construction and low rotor inertia, SRMs have very rapid acceleration and extremely high speed operation [1]. Because of its wide speed range operation, SRMs are particularly suitable for operation in EV propulsion. In addition, the absence of magnetic sources (i.e., windings or permanent magnets) on the rotor makes the SRM relatively easy to cool and insensitive to high temperatures. The latter is of prime interest in automotive applications, which demand operation under harsh ambient conditions. The disadvantages of SRM drives are their high torque ripple and acoustic noise levels [1].

1.4 Air-Cored PM machines for EVs

The development of new high energy density and high coercivity magnetic materials has increased the design possibilities of permanent magnet motors. High energy density magnets allow for an increase of the airgap without a reduction in the magnetic field density in the airgap. This has lead to an increase of interest in slotless (coreless) permanent magnet synchronous motors for high performance applications, such as electric vehicles. The slotless configurations has some very interesting properties as compared to traditional cored machines [2] such as:

- No cogging torque
- No teeth losses and hence a significant reduction in core losses
- Linear current-torque relation
- Lower stator inductance
- A near perfect sinusoidal back emf
- No iron saturation in stator teeth

All these properties potentially leads to a higher efficiency machine than regular slotted machines. The drawback is that more permanent magnet material is needed to obtain the same magnetic field density in the airgap. However, should the permanent magnet technology continue to evolve, coreless machines may be designed with much higher magnetic flux densities than slotted machines as they are not limited by iron saturation.

1.4.1 Different topologies of air-cored PM machines

The two main distinct topologies of the air-cored PM machine are the radial flux and axial flux topologies shown in Fig. 1.11. The names are derived upon the flux direction within the machines airgap.

In the axial flux geometry, the stator is placed between two rotor disks with permanent magnets. The magnetic path goes from one disk to the other through the ironless stator and the return path goes through the rotating back yoke of the rotor. This topology is more

appropriate for high pole numbers, short axial length and low speed applications.

The radial flux machine is the most familiar machine type recognised by its cylindrical shape. This machine geometry consists of an inner rotor and an outer rotor with the air-cored stator nested between the two rotors. The back yoke of the two rotor disks provide the return path for the magnetic field. This topology is more appropriate for high speed applications.

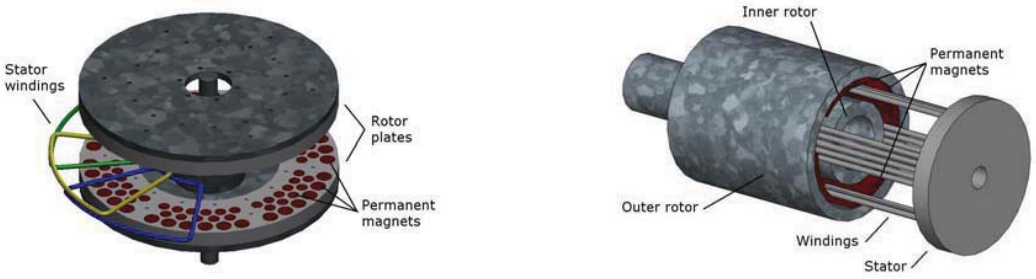

(a) Axial flux topology (b) Radial flux topology

Figure 1.11: Configuration of axial flux and radial flux air-cored PM machines topologies [2].

1.5 Problem statement

With the current research being conducted on EVs worldwide, it is still unclear as to which drive motor and drivetrain system are best suited for the development of a cost effective EV which will gain the public's acceptance. These studies focus mainly on direct in-wheel drive, direct differential drive and fixed-gear differential drive topologies. Furthermore, the control strategy for these type of motor drives require a, so called, field-weakening operation in order to achieve acceptable performance characteristics for the vehicle.

This thesis, therefore, aims to investigate a manual gearbox drivetrain topology and a radial flux air-cored permanent magnet (RFAPM) synchronous machine, without flux-weakening operation, as traction drive for EV applications.

1.6 Approach to problem

For the purpose of this research study, a conventional family vehicle will be converted to a battery electric vehicle. The vehicle that will be used is an 2006 model Opel Corsa Lite which was sponsored by General Motors South Africa (GMSA) to the University of Stellenbosch for this study. The Opel Corsa will be converted with the aim to retain all the functionality of the original vehicle except that, the internal combustion engine will be replaced by an electric motor to drive the 5-speed manual transmission of the Corsa and a battery pack will be used as energy source to drive the electric motor. The Corsa is renamed to the E-Corsa.

The approach that is followed in order to achieve the desired outcome of the project, can be summarised as follows:

- Requirements for the conversion of the Opel Corsa to a battery electric vehicle are reviewed and implemented practically.
- Both analytical and finite element analysis are implemented for the drive motor design of the E-Corsa.
- *MATLAB*® and *Simulink*® are used to assist in the design of the current controllers for the traction drive.
- *Simplorer*® simulations are used to assist in the design of the power electronic converter.
- Tests and measurements are conducted in the lab and on the completed E-Corsa.
- Conclusions and recommendations on the outcome of the project are derived.

1.7 Thesis layout

The layout of this thesis is briefly described as follows:

Chapter 2: In this chapter various drive systems mainly for electric transportation systems are reviewed.

Chapter 3: In this chapter the Li-ion battery cell technology used as the power source for the electric vehicle together with the packaging, maintenance and care of the battery pack is discussed in detail.

Chapter 4: In this chapter the performance characteristics of the RFAPM machine is identified. Both analytical and finite element methods are used to design and evaluate the electric motor.

Chapter 5: In this chapter a complete overview of the power electronic inverter and digital controller is given and the design methodology of this system is discussed in detail.

Chapter 6: In this chapter an accurate dq model for the RFAPM machine is derived. The equivalent dq model is implemented into a *MATLAB*® *Simulink*® model to design and test a current controller for the RFAPM machine.

Chapter 7: In this chapter the test bench measurements and measurements on the E-Corsa are given and discussed in detail.

Chapter 8: This chapter concludes on the outcome of the project and recommendations for future work and improvements are discussed.

Chapter 2

Overview of the E-Corsa conversion

In this chapter aspects concerning the conversion of the Opel Corsa to a battery electric vehicle is described. Also, the various original components and parts of the Corsa that require consideration as whether to retain or to remove them are discussed. The main focus concerning the conversion of the Opel Corsa is to keep the vehicle as standard as possible. The original 5-speed manual transmission of the Corsa is retained and is used as the drivetrain for the vehicle. Fig. 2.1 shows the front and side view of the E-Corsa that is used for the purpose of this study.

(a) (b)

Figure 2.1: Photos of the E-Corsa.

2.1 Considerations for the conversion of the Opel Corsa

There are a multitude of parts and components in the original vehicle that needs consideration as whether to remove or retain them. There are also a number of components that must be added to the vehicle to ensure full integration. A breakdown of the various components of the vehicle which is under consideration are listed below.

- The internal combustion engine
- The exhaust system
- The fuel system
- The instrument cluster
- The spare wheel
- The vehicle's 12 V battery
- The acceleration pedal
- The clutch for the transmission
- The power steering system
- Vacuum pump

From the components listed above, the components that are removed from the vehicle are:

- The internal combustion engine
- The exhaust system
- The fuel system

The remaining components from the list are discussed next.

Instrument cluster

In order to maintain the originality of the Corsa, it is desired to retain the original instrument cluster of the Corsa. In the original Corsa, the instrument cluster is controlled by the engine management system which controls the following systems on the instrument cluster:

- Speedometer
- Tachometer
- Fuel gauge
- Temperature gauge
- Backlight
- Left and right indicator lights
- The oil, battery, brake, high beam and engine warning lights
- Warning buzzer and instrument cluster power

For the E-Corsa it is required that the instrument cluster provides all the original functionality except that the tachometer should display the rotating speed of the electric drive motor, the fuel gauge should display the state of charge (SOC) left on the battery pack and the temperature gauge should display the temperature of the power electronic converter or of the electric drive motor.

To integrate the instrument cluster with the digital controller of the electric motor drive, a Controller Area Network (CAN) interface has been developed as part of a final year project at the University of Stellenbosch. The CAN interface enables the digital controller of the electric motor drive to relay information to the instrument cluster via a CAN bus. For more background on the CAN instrument cluster controller refer to [7]. Fig. 2.2 shows the test setup of the CAN instrument cluster controller.

Figure 2.2: Test setup of the CAN instrument cluster controller.

Spare wheel

The spare wheel could be replaced with a smaller lighter option, or even replaced with products that provide instant repairs to flat tyres. In the aim to retain the seating capacity of the Corsa, the spare wheel is replaced with an instant repair canister and the battery pack is partially mounted in the place of the spare wheel.

12 V Battery

The 12V battery of the Corsa car is intended to provide power to all the additional 12 V systems in the vehicle such as, the lights, the engine management system, the power steering system etc. The 12 V battery is, therefore, retained.

Acceleration pedal

The acceleration pedal of the Corsa is a mechanical system that regulates the amount of fuel injected into the injection system via a steel cable. This pedal is, therefore, replaced by a so called drive-by-wire pedal which is manufactured by Bosch. The resistance felt when the pedal is depressed is designed to give the same feel as a conventional throttle. The throttle pedal, in this instance, has 6 electrical connections, achieving the accuracy required from the pedals movement. Fig. 2.3 shows the drive-by-wire pedal.

Figure 2.3: A photo of the drive-by-wire acceleration pedal.

Clutch

Although a transmission without a clutch is technically feasible it is, however, easier and more pleasant to drive a vehicle with a clutch. In addition, there is a safety that a clutch provides; with a clutch the operator is able to disengage the motor from the gearbox with ease if it should be necessary and also, the retention of the clutch results in less wear on the transmission gears. For safety, ease of operation and a reduction in wear on the transmission gears, the clutch is retained.

Power steering system

The Opel Corsa is fitted with a hydraulic power assisted steering (HPAS) system. The vehicle could function without it and the removal of the power steering provides a small weight loss. However, power assisted steering systems are designed to reduce the input force required by the operator to steer the vehicle by providing additional control. Power steering

provides a safety feature in vehicles since fatigue in drivers is reduced. The vehicle is also easier and more pleasant to drive with a power assisted steering system. For the safety and comfort it provides, the power steering is retained.

With the engine removed the source of power for the power steering pump is removed and an additional source of power must be found. Options available for the replacement of the power steering pump drive are; to run a belt off the motors shaft, use an electric motor to drive the pump, or install a full electric power steering system. Full electric power steering systems provide the ability to operate only on demand as opposed to the original hydraulic system which is always on and the total efficiency of the electric vehicle is thereby increased.

The Toyota MR2 is fitted with a full electric power steering system and this system is used to replace the original hydraulic power steering system of the Corsa. Fig. 2.4(a) shows the power steering pump of the Toyota MR2 and Fig. 2.4(b) shows the power steering pump mounted inside the engine bay of the Corsa.

(a) Power steering pump

(b) Power steering pump mounted inside the engine bay of the Corsa

Figure 2.4: Photos of the electric power steering pump of the Toyota MR2.

Vacuum pump

The braking system on the Corsa utilises a vacuum assist that use pressure generated from the combustion engine. With the removal of the engine an additional source must be found to generate a vacuum in the brake system. An electric vacuum pump is integrated into the engine bay of the Corsa and powered from the 12 V battery to provide the vacuum for the braking system. Fig. 2.5 shows the electric vacuum pump mounted inside the engine bay of the Corsa.

Figure 2.5: Electric vacuum pump.

2.2 Conversion structure of the E-Corsa

An illustration of the conversion structure of the E-Corsa is shown in Fig. 2.6. The battery pack is mounted partially in the front and partially in the back of the vehicle to maintain an even weight distribution in the vehicle. Furthermore, the drive motor is mounted directly onto the original 5-speed manual gearbox. Also, an external charger as opposed to an on-board charger is used for the prototype vehicle. This conversion structure of the E-Corsa is the main focus of the study throughout this thesis.

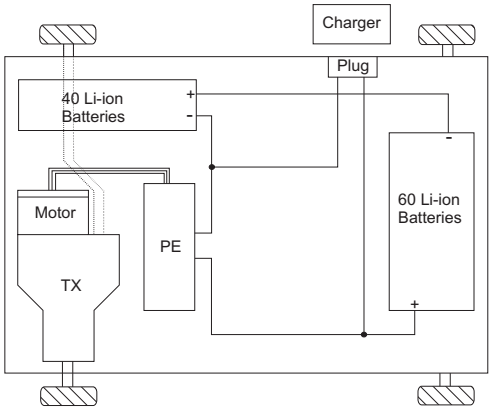

Figure 2.6: Structure of a full electric E-Corsa vehicle with manual transmission.

Chapter 3

Li-ion Battery Pack Design

In this chapter the design of the Li-ion battery pack for the E-Corsa conversion, based upon the desired range and speed requirements of the vehicle, is described. The charging and maintenance of the battery pack is also discussed and the mounting of the battery pack inside the E-Corsa is explained.

3.1 Battery technologies for EVs

The traction battery is the most critical component of the vehicle and in most cases it will also be the most expensive component. Through the years, several battery types have been developed. Only a small number however, can be considered for use in electric vehicles.

Batteries are characterised by their life cycle, energy and power density and energy efficiency. The life cycle represents the number of charging and discharging cycles that the battery can endure before it looses its ability to hold a useful charge (mostly when the available capacity drops under 80% of its initial capacity). The life cycle typically depends on the depth of charge (DOC). The life cycle multiplied by the energy content corresponds with the calender life, which gives an idea how many times the battery is to be replaced during the lifetime of the vehicle.

When charging and discharging a battery not all the stored energy in the battery will be available due to battery losses, which are characterised by the efficiency of the battery. The energy and power density describe the energy content (vehicle range) and the possible power (vehicle performance) as a function of the weight of the battery. A battery can be optimised to have a high energy content or to have a high power capability. The first optimisation is important for battery electric vehicles, while the second is required for hybrid electric vehicles (HEVs).

For electric vehicles, the energy and power ratings of the battery cells, which are specified by the US Advanced Battery Consortium, should be at least 50 Wh/kg and 100 W/kg, respectively. The current long term goals for battery power and energy density capabilities are 400 W/kg and 300 Wh/kg, respectively. Some characteristics of the most important

electric vehicle batteries are summarised in Table 3.1.

Table 3.1: Characteristics of the most important battery types for EVs

Specifications	Lead based	Nickel based	Zinc based	Sodium based	Lithium based
Cell voltage	2 V	1.2 V	1.4-1.6 V	2-2.5 V	3.3-3.7 V
Energy density	30-35 Wh/kg	50-80 Wh/kg	70-80 Wh/kg	90-130 Wh/kg	80-200 Wh/kg
Power density	70-130 W/kg	170-175 W/kg	100-125 W/kg	100-160 W/kg	140-1000 W/kg
Energy efficiency	70-85%	60-85%	65-85%	80-90%	85-95%
Life cycle	600-1000	1500-2000	500-2000	600-1000	>1000

From this table it becomes clear that Lithium based batteries are the most advanced battery technology available. Lithium based batteries are also the most preferred battery technology for use in electric vehicle applications and especially the Lithium-ion (Li-ion) type battery. The composition of a Li-ion cell will be discussed in the following subsection.

3.1.1 Composition of a Li-ion cell

The composition of a Li-ion cell is divided into three basic functional components namely, the anode, the cathode and the electrolyte. The anode of the cell is normally made out of graphite and the cathode is made out of either a layered oxide such as lithium cobalt oxide, a polyanion such as lithium iron phosphate or a spinal such as lithium manganese oxide. The use of different chemical compositions for the cathode results in different cell voltages and gravimetric capacities of a cell. Listed in Table 3.2, are the most common used materials for cathode compositions of a Li-ion cell, along with the average cell voltages and gravimetric capacities of the different compositions. The electrolyte consists of a solid lithium-salt such as lithium hexafluorophosphate ($LiPF_6$) and an organic solvent such as ether. During charging of a Li-ion cell, lithium is extracted from the cathode and inserted

Table 3.2: Li-ion Cathode Compositions

Materials	Average Voltage	Gravimetric Capacity
$LiCoO_2$	3.7 V	140 mAh/g
$LiMnO_2$	3.3 V	100 mAh/g
$LiFePO_4$	4.0 V	170 mAh/g
Li_2FePO_4F	3.6 V	115 mAh/g

into the anode. During discharge of a Li-ion cell the process is reversed so that lithium is extracted from the anode and inserted into the cathode. Therefore, the anode and the cathode are both materials which lithium can migrate into and migrate out from depending on whether the cell is being charged or discharged.

3.2 Battery pack design

There are two possible methods that can be followed in designing the size of the battery pack for the EV. The first method is to design the battery pack according to the specifications of the electric motor. The second method is to design the electric motor according to the specifications of the battery pack. Using the first method, i.e designing the battery pack according to the motor specifications, involve a couple of problems. The first problem is that the battery pack can easily become oversized, which adds unnecessarily to the cost and weight, although the range of the EV is increased. The second problem is that the limitations of the space in which the battery pack can be mounted, cannot be taken into account. The battery pack of the E-Corsa is therefore designed using the second method.

3.2.1 Battery selection

The Chinese manufacturer Thunder Sky was selected as the battery manufacturer of choice, as their products have been used in a number of similar projects internationally. Thunder Sky manufactures Li-ion batteries in three capacities; 40, 60 and 90 Amp hours. The battery of choice is the TS-LFP40AHA, which is the 40 Ah cell. A photo of the TS-LFP40AHA cell is shown in Fig. 3.1 and the manufacturer's specifications for this cell are listed in Table 3.3.

Table 3.3: Manufacturer's specifications of the TS-LFP40AHA Li-ion cell

TS-LFP40AHA Li-ion battery cell	
Current capacity	40 Ah
Minimum voltage	2.5 V
Maximum voltage	4.25 V
Average cell voltage	3.375 V
Maximum charging current	120 A
Maximum continuous discharging current	120 A
Average cell weight	1.6 kg
Operating temperature range	-20°C to 75°C
Maximum number of charge and discharge cycles	3000

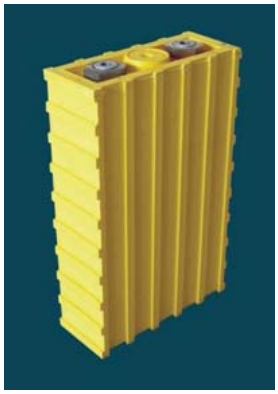

Figure 3.1: TS-LFP40AHA Li-ion battery cell.

3.2.2 Range and speed requirements for the E-Corsa

The desired range and speed requirements for the E-Corsa are as follows:

The E-Corsa should be able to travel at a top speed of 140 km/h on a flat road with a 0% gradient. Furthermore, the E-Corsa should be able drive at 100 km/h, on a 0% gradient road, for a minimum distance of 100 km. From these two specifications, the energy capacity and the minimum power requirements of the battery pack can be determined. From road tests conducted on the Opel Corsa with it's internal combustion engine, the power requirements at different speeds in 5th gear, were determined and are listed in Table 3.4.

Table 3.4: Power requirements at different speeds in 5^{th} gear

Speed	kW Used
80	10
100	15
120	24
140	35

These tests were conducted at sea level, on a warm day with clear skies and a light wind. From the results in Table 3.4, the minimum power rating of the battery pack can be identified as 35 kW and the minimum required energy capacity, as 15 kWh.

3.2.3 Battery pack sizing

As a starting point to the battery pack design, consider that all the cells in the battery pack are connected in series. The maximum continuous current that the pack can deliver is then determined by the maximum continuous current that a single cell can deliver. By using the energy capacity requirement to achieve the desired range, the minimum number of cells needed can be determined as

$$\begin{aligned} n_c &= \frac{W_{min}}{V_c \cdot I_c h} \\ &= \frac{15\ kWh}{3.375\ V \cdot 40\ Ah} \\ &\approx 112 \end{aligned} \tag{3.2.1}$$

where, W_{min} is the minimum required energy capacity of the battery pack, V_c is the average voltage of a single cell and $I_c h$ is the current capacity of a single cell. With 112 cells connected in series, the average battery pack voltage will be

$$\begin{aligned} V_{bus} &= V_c \times n_c \\ &= 3.375\ V \times 112 \\ &= 378\ V \end{aligned} \tag{3.2.2}$$

Finally, from (3.2.2), the average power rating of the battery pack is

$$\begin{aligned} P_{avg} &= V_{bus} \times I_{max} \\ &= 378\ V \times 120\ A \\ &= 45.36\ kW \end{aligned} \tag{3.2.3}$$

where I_{max} is the maximum continuous current, (120 A as listed in Table 3.3), that the battery pack can deliver.

Although the energy capacity demand can be met with an 112 cell battery pack, it is apparent from (3.2.3) that the power rating of this size battery pack will be 10 kW more than is required. Keeping in mind that factors unknown at this stage, such as inverter losses, motor efficiency and the gross weight of the vehicle, have not been accounted for, it would be advantageous not too reduce the battery pack size to much, in order to compensate for such factors. It has therefore been decided to reduce the number of cells to 100. The energy capacity of a 100 cell battery pack will be

$$W = n_c \cdot V_c \cdot I_c h \tag{3.2.4}$$

$$= 100 \cdot 3.375\ V \cdot 40\ Ah$$

$$= 13.5\ kWh$$

With a energy capacity of 13.5 kWh, it will be possible to drive at a constant speed of between 85-90 km/h for distance of 100 km. This is more than satisfactory, as the speed limit in urban areas is rarely above 80 km/h. The average power rating of a 100 cell battery pack will therefore be

$$P_{avg} = n_c \cdot V_c \cdot I_{max} \tag{3.2.5}$$

$$= 100 \cdot 3.375\ V \cdot 120\ A$$

$$= 40.5\ kW$$

The complete specifications of the final battery pack design are listed in Table 3.5.

Table 3.5: Full battery pack specifications of the E-Corsa

Battery cell capacity:	40 Ah
Number of cells:	100 - All connected in series
Energy capacity:	13.5 kWh
Average power rating:	40.5 kW
Nominal bus voltage:	337.5 V
Maximum bus voltage:	425 V
Motor line voltage:	208.8 V_{RMS}
Motor phase voltage:	120.22 V_{RMS}
Front pack weight:	67 kg
Rear pack weight:	120 kg
Combined weight:	187 kg

3.3 Charging and discharging

After the Li-ion battery cells come off the production line, they are charged to 70 % of their maximum capacity. This is also the recommended charge at which the cells should be stored, when they are not used for an extended period of time. It is recommended by the manufacturer that the cells undergo a number of controlled charge and discharge cycles, at 30 % of their maximum charge and discharge current, before being used in the desired application.

During charging and discharging extreme caution should be taken, as the most profound drawback of Li-ion cells is their extreme sensitivity to over charging, over discharging and swelling. Over charging or over discharging results in an irreversable chemical reaction taking place inside the cell, and this process will be explained next.

Over charging of a Li-ion cell will lead to the synthesis of cobalt oxide, through a chemical reaction which changes the chemical composition of the cell permanently. This irreversable reaction is described by

$$LiCoO_2 \longrightarrow Li^+ + CoO_2 \tag{3.3.1}$$

In the case of a cell being over discharged, the lithium cobalt oxide cathode will become supersaturated, which will lead to the production of lithium oxide. This irreversable reaction is described by

$$Li^+ + LiCoO_2 \longrightarrow Li^2 + CoO_2 \tag{3.3.2}$$

The reactions described by (3.3.2) and (3.3.1) are specifically for the TS-LFP40AHA Li-ion cell. Similar reactions will occur in Li-ion cells with different anode and cathode compositions.

Each individual cell of the battery pack come with a slight difference in charge and internal resistance. By closely studying the charging characteristics of the Li-ion cell, shown in Fig. 3.2), it can be noticed that cells with a slightly higher charge than others will reach their maximum charging capacity more quickly. This is also the case for cells with a lower internal resistance. Cells with a higher internal resistance will discharge faster. In both these cases over charging and over discharging can occur. To ensure that all the cells in the battery pack are equally charged, a battery management system (BMS) is used to monitor each individual cell and thereby control the charging process. The BMS and charger system will be discussed in the following two sections.

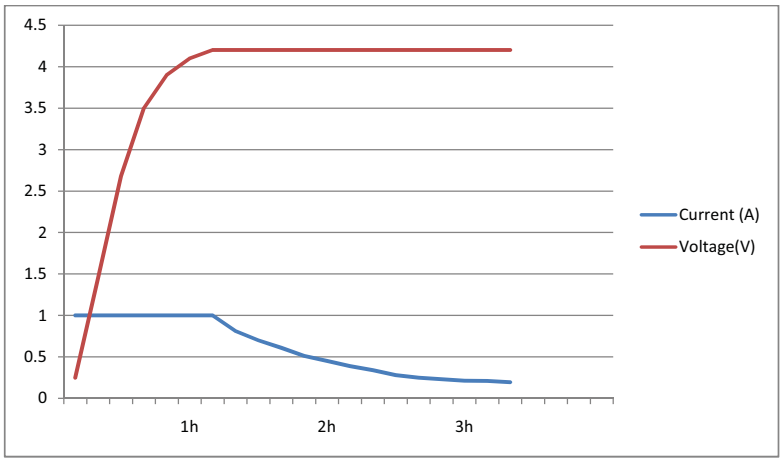

Figure 3.2: Charging curve of the TS-LFP40AHA cell.

During charging and discharging the cells expand or swell as a result of the chemical reac-

tions occurring inside the cell. If the swelling is not constrained, the physical structure of the cells will be damaged, leading to permanent alteration of the chemical composition of the cells. It is therefore required that the batteries be clamped, in a vice like manner, in order to maintain their physical structure. The clamping device that was used for the battery pack of the E-Corsa consists of two 5 mm thick metal plates, placed on either side of a group of 10 batteries, with two full thread rods that pull the plates together to compress batteries as shown in Fig. (3.3).

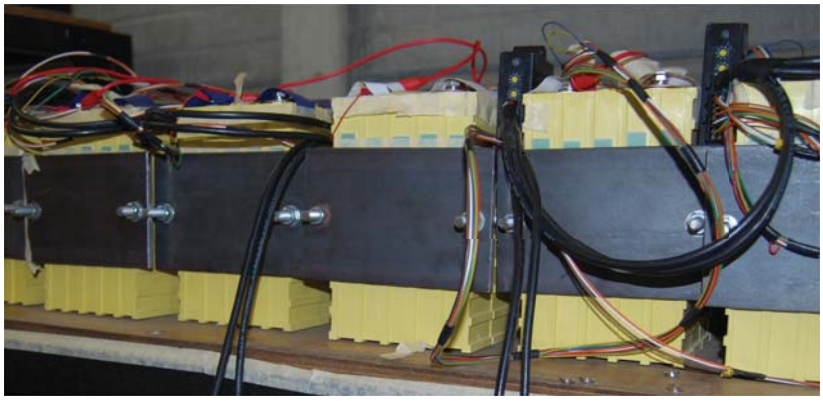

Figure 3.3: Battery clamping device.

3.4 Battery management system

Fig. 3.4 is an illustration of a typical battery management system (BMS). The BMS works together with the charger and is specifically designed for the type of Li-ion cell technology that is being used, as well as, the number of cells that are in the battery pack. The voltage of every individual cell in the battery pack, together with the current at which the battery pack is being charged, is measured by the BMS. These measurements are processed by the BMS and the information is relayed back to the charger, which regulates the charging current accordingly. This will ensure that all the cells are charged equally without any cells being over charged.
The purpose of the BMS is to optimise the functionality of the battery pack and to alert the operator to any faults. The three main objectives of the BMS [5] are as follows:

- To prolong the life of the batteries
- To maintain the batteries in an optimal state
- To protect the batteries from being damaged

For the battery pack of the E-Corsa, a BMS produced by the battery manufacturer for use with up to 100 cells is used. This system includes the following parts:

- A colour LCD, and management computer

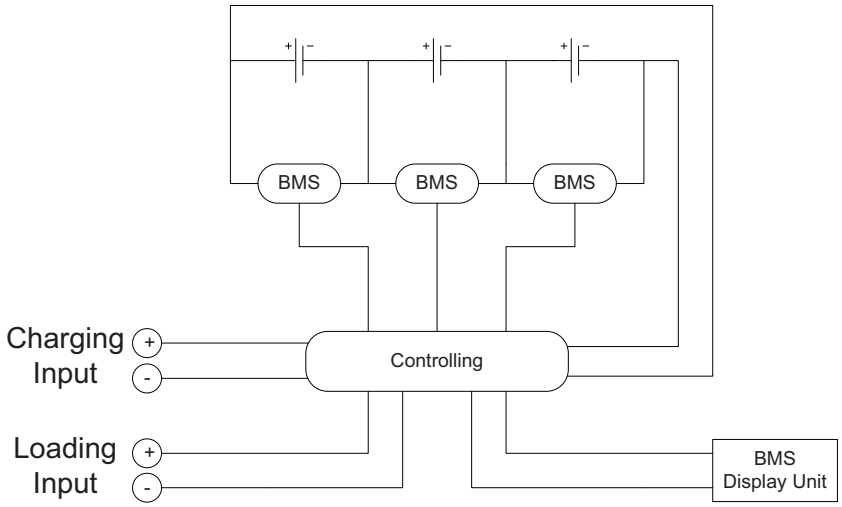

Figure 3.4: Typical BMS schematic.

- Voltage, current and temperature measurement modules

The LCD monitor displays the total voltage, total current, maximum temperature and the storage of power as well as the maximum and minimum voltage of every single cell in a pack. The measurement modules are used to measure cell parameters. The LCD unit is mounted in the centre console of the E-Corsa to provide more detailed information on the status of the battery pack to the driver. The display unit is shown in Fig. 3.5

Figure 3.5: Display unit of the battery management system.

3.5 Battery charger

The battery management system and charger comes as a unit. The charger charges the Li-ion batteries in two phases. In the first stage, the batteries are charged at a controlled constant current until the voltage threshold of the cells is reached. In the second phase,

the voltage is kept constant and the current is systematically reduced over a period of time until it reaches 30% of the cell's maximum current rating, after which the charging cycle is terminated. This charging procedure is controlled by the battery management system (BMS). The charger is shown in Fig. 3.6.

Figure 3.6: Li-ion battery charger

3.6 Battery pack mounting

To maintain an even weight distribution in the vehicle the battery pack is be mounted partially in the front and partially in the back of the vehicle. The partitioning of the battery pack is determined by the physical size of the Li-ion cell, shown in Fig. 3.7.

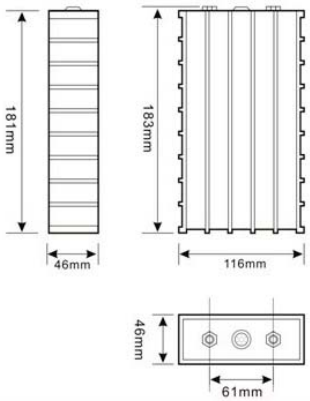

Figure 3.7: Dimensions of a TS-LFP40AHA Li-ion battery cell.

It is determined from these dimensions that a maximum of 60 cells can be fitted in the back of the vehicle and the remaining 40 cells in front. The size of the battery mounting racks are taken into account.

Fig. 3.8 shows the front mounted battery pack, which has a total weight of 67 kg, including the mounting rack. Fig. 3.9 shows the rear mounted battery pack with a total weight of 120 kg. It can be seen from Fig. 3.9 that the rear battery pack is mounted underneath the floor board of the boot, in place of the spare wheel, in such a way that the original boot space is retained. A high voltage and current socket is also installed, in the position of the original filling cap of the Corsa, through which the battery pack is charged as shown in Fig. 3.10.

Figure 3.8: Front mounted battery pack.

(a)

(b)

Figure 3.9: Rear mounted battery pack.

Figure 3.10: Battery pack charging socket.

Chapter 4

Design of the RFAPM Drive Motor

The design of the dual-rotor radial flux air-cored permanent magnet (RFAPM) drive motor of the E-Corsa is described in this chapter. The machine is designed by using analytical methods and the results of the analytical design are verified through a finite element analysis of the RFAPM machine.

4.1 The RFAPM machine topology

The RFAPM machine topology consists of an inner rotor and an outer rotor rotating at the same speed, with an air-cored stator nested between the two rotors. The construction of the RFAPM machine is shown in Fig. 4.1.

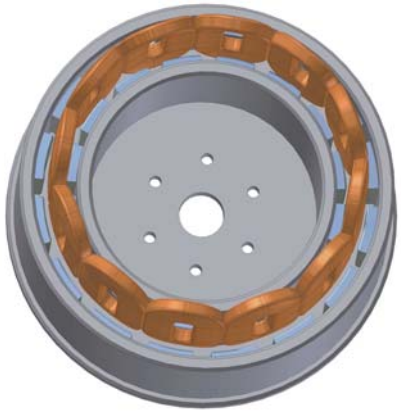

Figure 4.1: A 3D view of a RFAPM machine construction with concentrated coils [3].

Since for constant electrical and mechanical loadings the output torque is proportional to the air-gap surface area, this unique rotor-stator-rotor configuration results in a slightly increased airgap volume which substantially increases the torque density of the machine. The disadvantage of the increased airgap volume is that a higher volume of permanent magnet is required to maintain the desired flux density within the airgaps. This adds to the overall cost and weight of the machine. The unique features of this dual-rotor air-cored

radial flux machine include very short end windings, high overload capability, balanced radial forces, no cogging torque, no stator core losses, high efficiency and low material costs [2].

In the following two subsections the rotor and stator topologies of the RFAPM machine are discussed in more detail.

4.1.1 Rotor topology

The dual-rotor topology consists of two cylindrical disks that are connected by a steel plate, as illustrated in Fig. 4.2. The rotor disks can be manufactured from solid steel, as opposed to laminated iron, since the iron losses in the rotor disks are negligible [8]. The steel rotor disks are multifunctional, as the rigid steel construction maintains the necessary airgap length between the opposing magnet poles while providing a return path for the flux lines.

Figure 4.2: Dual-rotor disks.

High energy NdFeB permanent magnets are mounted on the inner periphery of the outer rotor and on the outer periphery of the inner rotor. The magnets have a North-South polarisation arrangement with adjacent magnets of both the inner and outer rotor magnetized in the opposite direction (as shown in Fig. 4.3(a) and 4.3(b)). This polarisation arrangement causes the flux driven by the magnets to travel radially from the inner rotor to the outer rotor, or vice versa.

There are two possible ways in which the permanent magnets are usually mounted to the rotor disks. The magnets can be either surface-mounted, i.e mounted directly onto the surface of the rotor disks (as illustrated in Fig. 4.3(a)), or they can be embedded into the yoke of the rotor disks (as illustrated in Fig. 4.3(b)). The advantage of using surface-mounted magnets, as opposed to embedded magnets, is that the machining cost of the rotor disks is reduced, thereby reducing the overall cost of the machine. Another advantage of surface-mounted magnets is that the magnets naturally act as fans, assisting in the cooling of heat resulting from stator copper losses. The risk of excessive stator winding temperatures possibly

damaging or demagnetising the permanent magnets is thereby reduced. The magnets of the proposed machine are decided to be surface-mounted.

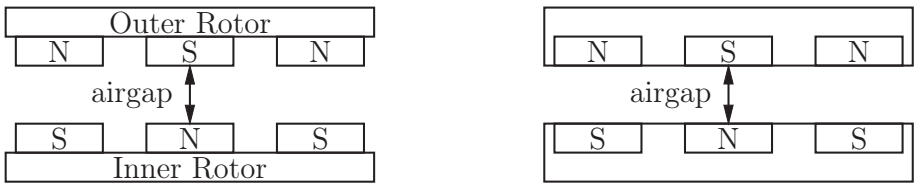

(a) Surface-mounted PMs (b) Embedded PMs

Figure 4.3: PM mounting types.

The spinning of the rotor results in a centrifugal force being exerted on the magnets. Surface-mounted magnets that are used in machines with a high rotational speed are subject to a very high resultant centrifugal force, which may be a cause for concern regarding the magnets that are mounted on the inner rotor. The permanent magnets, therefore, need to be secured by means of through-magnet fastening screws, as illustrated in Fig. 4.4. It is very important in this case to use screws made from a non-magnetic material, such as stainless steel. Machines with a low rotating speed, however, allow for the magnets to be glued on the rotor disk surfaces.

Figure 4.4: Through-magnet fastening.

4.1.2 Stator topology

In an air-cored stator winding the windings are not kept in position within iron slots, but with the use of epoxy resin. Therefore, with the absence of stator teeth and the stator back yoke there is no cogging torque and there are no iron losses in the stator. However, eddy current losses in the stator winding are significantly high at relatively high operating frequencies [9]. High eddy current losses result in an increase of temperature in the stator windings and a lower machine efficiency. The eddy current losses can be minimised by using Litz-wire. Litz-wire involves splitting a single strand conductor into several very thin parallel connected strands and twisting them all together along the axial length.

The different winding layout configurations of the stator coils are divided into two main categories namely, overlapping and non-overlapping. A three-dimensional view of the typical coil configurations of overlapping and non-overlapping stator coil are shown in Fig. 4.5.

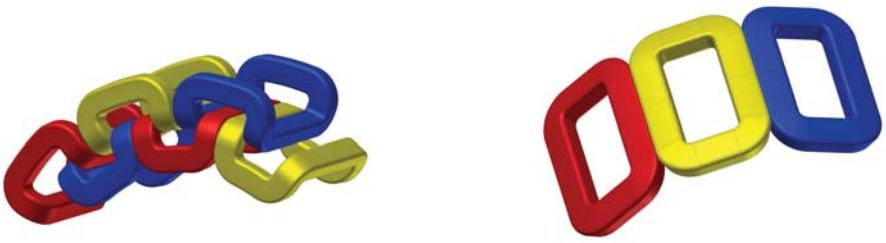

(a) Overlapping stator coils (b) Non-overlapping stator coils

Figure 4.5: A 3D view of the typical stator coil configurations for the RFAPM machine [3].

The winding layout configuration that will be used for the proposed RFAPM machine is that of the non-overlapping type. The windings are arranged in such a way that all adjacent coil sides touch without overlapping, resulting in a maximised flux-linkage due to the coil widths being closer to π electrical degrees. The main reason for using non-overlapping coils rather than over-lapping coils is to reduce the manufacturing costs of the machine while producing the same amount of torque [3]. Using non-overlapping coils has the following advantages:

- a simpler coil construction, which could ultimately lead to automated manufacturing of the stator [3]
- shorter end-turn lengths of the coils result in less copper being used, thereby reducing copper losses and overall cost of the machine

4.2 Design specifications

The internal combustion engine of the Opel Corsa is replaced by the RFAPM drive motor. The drive motor is mounted directly onto the original 5-speed manual gearbox and the clutch is still used. A basic assembly model of the RFAPM machine, clutch and gearbox is shown in Fig. 4.6. The main design criterion for the RFAPM machine is, therefore, that the machine should match the performance specifications of the original internal combustion engine. These specifications are determined next.

The top speed of the E-Corsa is defined in Chapter 3 as 140 km/h. From the engine speed profile of the internal combustion engine, shown in Fig. 4.7, the engine speed at 140 km/h in 5^{th} is 4800 rpm. The RFAPM should, therefore, be designed for a rated speed of 4800 rpm.

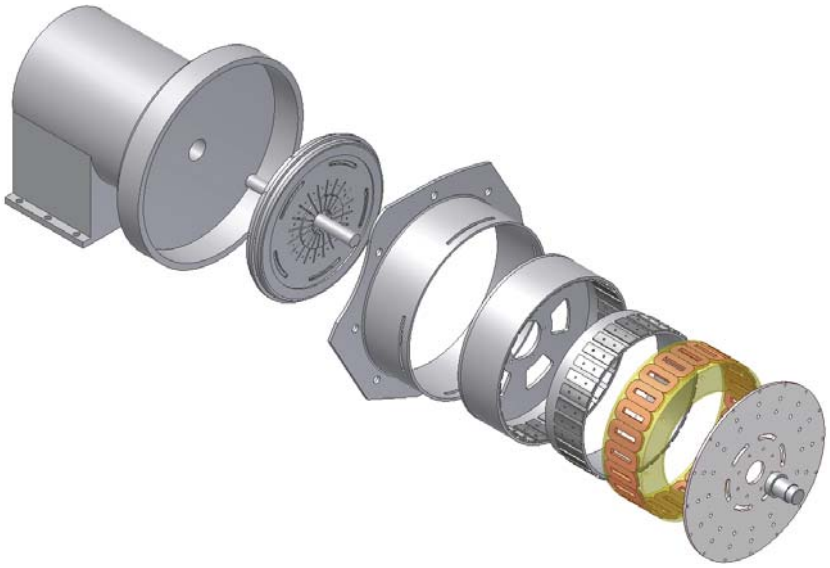

Figure 4.6: Assembly model of the RFAPM machine, clutch and gearbox.

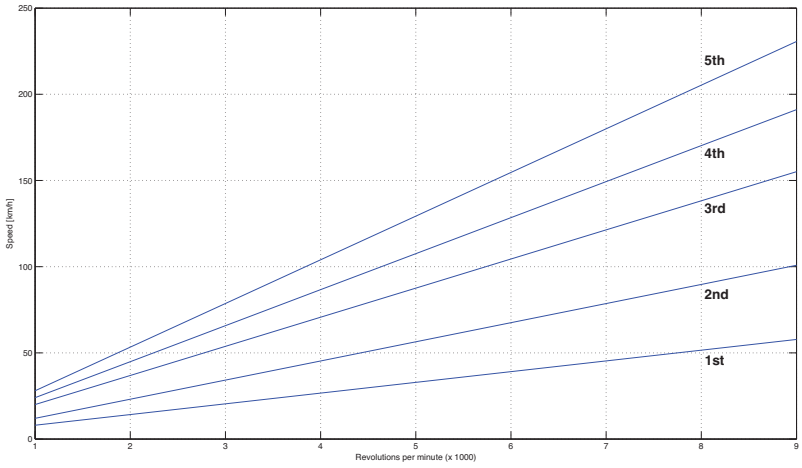

Figure 4.7: Engine speed profile of the internal combustion engine.

The rated torque of the RFAPM machine can be determined from the rated power (determined by the battery pack design in Chapter 3) and rated speed of the machine as

$$\begin{aligned} T &= \frac{P}{\omega} \\ &= \frac{40\ kW}{574.7\ rad/s} \\ &= 69.6\ \text{Nm} \end{aligned} \tag{4.2.1}$$

The final rated design specifications for the RFAPM machine, together with the line and phase voltages obtained from the battery pack design, are summarised in Table 4.1.

Table 4.1: Rated specifications of the RFAPM machine

RFAPM machine design specifications		
Rated power	40	(kW)
Rated torque	70	(N.m)
Rated speed	4800	(r/min)
Rated line voltage	208.8	V_{RMS}
Rated phase voltage	120.2	V_{RMS}

4.3 Analytical design

For the analytical design of the RFAPM machine, a complete analysis of the machine is performed in Appendix A. The analytical design is performed through an iterative process until a desired machine design is obtained. To perform this iterative process manually is time consuming and allows the possibility of calculating errors being made. A Python program has, therefore, been developed to perform this design process automatically. The source code of this design program is listed in Appendix E.1. However, there are many unknown parameters involved in the design of the RFAPM machine. It is, therefore, essential to assign some fixed parameters which can be used by the design program to determine the remaining parameters as part of the design process. The parameters that are desired to be kept constant are defined next.

4.3.1 Constant design parameters

The outer diameter of the machine is, due to the mechanical assembly, constrained by the inner diameter of the gearbox to a maximum of 252 mm. The outer diameter of the machine will, therefore, be fixed to 252 mm and the length of the machine is varied in the design process to obtain the required torque.

With a rated motor speed of 4800 rpm and a desired machine frequency of 960 Hz a total number of 24 poles are required. Furthermore, due to the high rotating speed of the machine the magnet height (h_m) needs to be kept to a minimum to reduce weight. A magnet height of 4 mm has, therefore, been decided on. An average airgap flux density (B_g) of 0.56 T is also desired. With the magnet height and the airgap flux density defined, the airgap length is determined from (A.3.1) as 1 mm.

In eqn. (A.1.16), it is shown that the eddy-current losses in the machine can be minimised by splitting a single-strand conductor into several, thin, parallel-connected strands, which are twisted together. Therefore, to minimise the total eddy current losses in the RFAPM machine, a total number of 36 parallel-connected strands per conductor will be used, i.e ($N_p = 36$).

The constant design parameters are summarised in Table 4.2

Table 4.2: Constant design parameters

Constant Parameters		
$\rho_t = 2.1 \times 10^{-8}$ Ω m	$\Upsilon_{cu} = 8900 \quad kg/m^3$	$\Upsilon_{NdFeB} = 7500 \quad kg/m^3$
$B_g = 0.56$ T	$\ell_g = 1$ mm	$k_f = 0.42$
$k_d = 1$	$k_c = 0.32$	$\tau_m = 0.7$
p = 24	a = q	$N_p = 36$

4.3.2 Analytical design results

From the performance specifications in Table 4.1 and the constant design parameters defined in Table 4.2, the final analytical design results of the machine are summarised in Table 4.3

4.4 Finite element analysis

In this section a finite element analysis (FEA) of the machine is performed in order to verify the effectiveness of the theoretical equations used in the design process and validate the design parameters. A two-dimensional FE analysis is performed on a simplified linear equivalent machine model of the analytical machine design as shown in Fig. 4.8. Table 4.4 gives the comparison results between the FEA and the analytical analysis of the RFAPM machine.

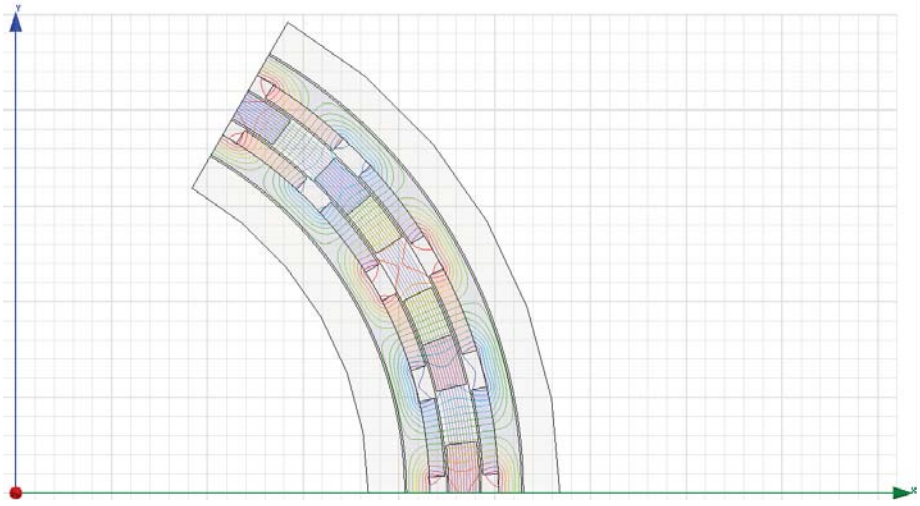

Figure 4.8: Simplified linear equivalent model for the RFAPM machine.

Table 4.3: Optimised design results for the RFAPM machine

Description:	Value:	Unit:
Rated power	40	kW
Rated torque	70	Nm
Rated speed	4800	r/min
Number of poles	24	
Number of stator coils	18	
Number of stator coils per phase	6	
Number of parallel circuits	6	
Radial thickness of coil winding (h)	8	mm
Active coil length (l)	80	mm
Coil width (W)	13.07	mm
Total end-turn length of coils (ℓ_{ec})	66.4	mm
Nominal stator radius (r_n)	117	mm
Air gap length (ℓ_g)	1	mm
Number of turns per coil (N)	36	
Number of strands per conductor	38	
Diameter of single strand conductor	0.2	mm
Magnet-pitch factor (τ_m)	0.66	
Magnet height (h_m)	4	mm
Yoke thickness (h_y)	5	mm
Inner rotor radius	108	mm
Inner rotor magnet width	21.53	mm
Outer rotor radius	126	mm
Outer rotor magnet width	24.28	mm
Line voltage	208.8	V_{RMS}
Phase voltage	120.2	V_{RMS}
Phase Current	97.3	A_{RMS}
Phase resistance	0.024	Ω
Magnetic flux linkage (λ_{pm})	0.03	
Total copper losses	680	W
Eddy current losses	568.31	W
Current density	13.3	A_{RMS}/mm^2
Total input power	36.1879	kW
Total output power	34.9396	kW
Rated efficiency	96.6	%
Total copper mass	1.592	kg
Total magnet mass	3.03	kg

Table 4.4: Comparison between the analytical analysis and the FEA of the RFAPM machine

Description	FEA	Analytical
Induced phase voltage	178 V	169.7 V
Developed torque	73 N.m	70 N.m
Airgap flux density	0.59 T	0.56 T
Phase inductance	27 μH	-

4.5 Cooling design

During the operation of an electrical machine, heat is generated from the electrical and mechanical losses of the machine. Materials in the machine, such as the copper wire and the permanent magnets, have limitations to the maximum temperature that they can be exposed to. By exposing these materials to temperatures in excess of their limitations could lead to, melting of the insulation on the copper wire as well as demagnetisation of the permanent magnets. Excessive heat inside the machine will also deteriorate its performance. A cooling system is therefore required to, effectively remove the heat from the machine, and also, to ensure that the temperature limitation of materials in the machine is never exceeded.

The main cause of concern for the cooling of the RFAPM machine is the high current density. The high current density implies that a large amount of heat is generated per volume which makes it extremely difficult to remove the heat effectively. For this reason both water cooling and air cooling systems were considered. Extensive testing of a water cooling system proved to be unsuccessful. The main reason for this is that a water cooling duct can be mounted only on the one side of the stator end-windings and the volume of heat that this system can remove is less than the volume of heat generated inside the coil, due to the high current density. Since this problem extends beyond the scope of this thesis, a specialist in this field was consulted.

An air cooling system was then proposed in terms of a centrifugal fan that is mounted to the one end of the inner rotor, facing towards the rotor shaft. The fan consists of two disks, separated by 24 radial blades, such that the distance between the two disks is 6 mm. The fan is mounted on the inner rotor so that the fan blades coincide with the leading faces of the magnets. Air is forced by the fan to flow radially between the magnets and around the stator in order to remove the heat. The fan was design to produce a required airflow of 0.028 m^3/s and force air through the clearance gaps at a velocity of 20 m/s.

The constructed cooling fan, which is mounted onto the inner rotor disk, is shown in Fig. 4.9

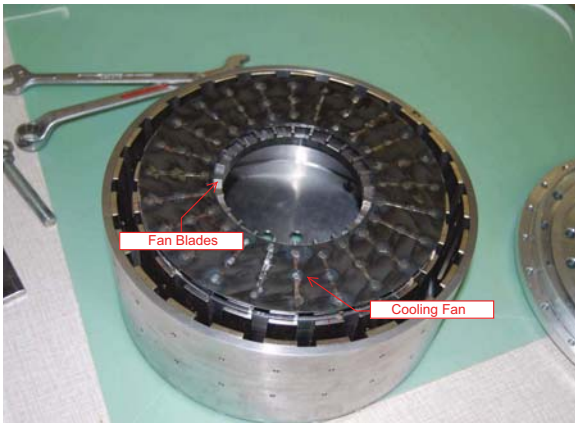

Figure 4.9: The constructed centrifugal cooling fan.

4.6 Machine assembly

Stator construction

To construct the stator, the non-overlapping stator coils are manufactured according to the specifications in Table 4.3 and placed around a stator mould. The spaces between the coils are filled with fibreglass fibres which would bond with the epoxy to give structural integrity to the stator mould. Bobbin is then wound around the coils to secure the coils around the mould. An outer mould was then placed around the coils to form the stator structure. The stator coils are then connected in wye and the stator back plate mounted onto the stator mould. The mould is filled with an epoxy resin and backed overnight. Fig. 4.10 illustrates these basic steps of the stator construction. The complete stator after it has been removed from the mould is shown in Fig. 4.11.

Rotor Assembly

The fully assembled rotor is shown in Fig. 4.12. The rotor disk is manufactured from mild steel, and N48H NdFeB magnets are secured to the rotor disks by means of through-magnet fastening.

Machine assembly

The assembled machine was mounted on a test bench for testing, as shown in Fig. 4.13(a). Fig. 4.13(b) shows the RFAPM machine mounted onto the gearbox.

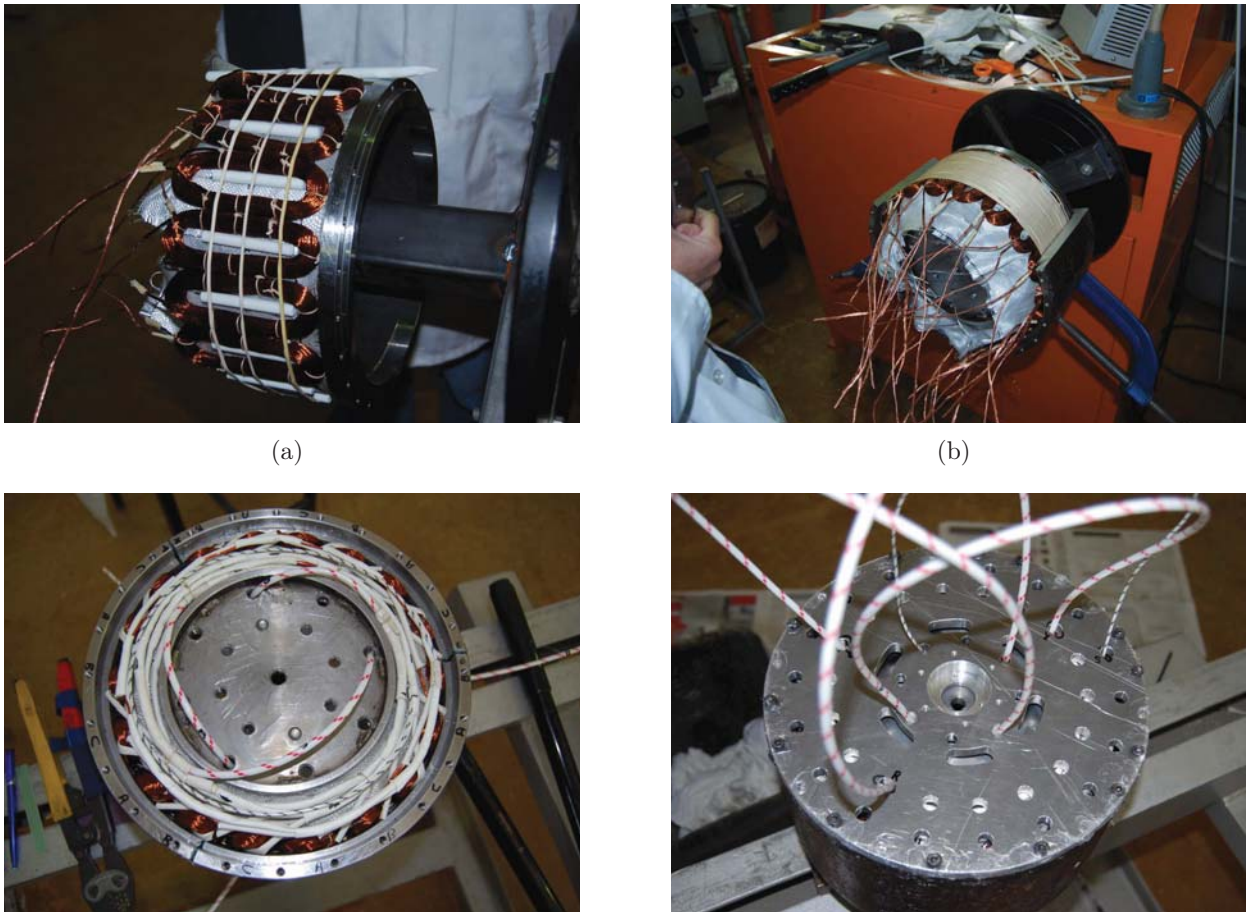

(a) (b)

(c) (d)

Figure 4.10: Manufacturing process of the air-cored stator.

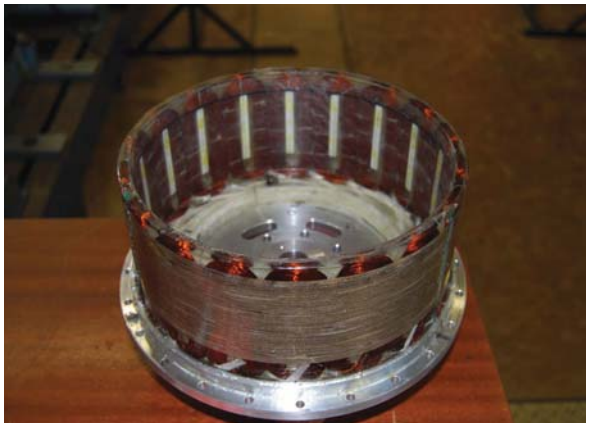

Figure 4.11: The complete manufactured air-core stator.

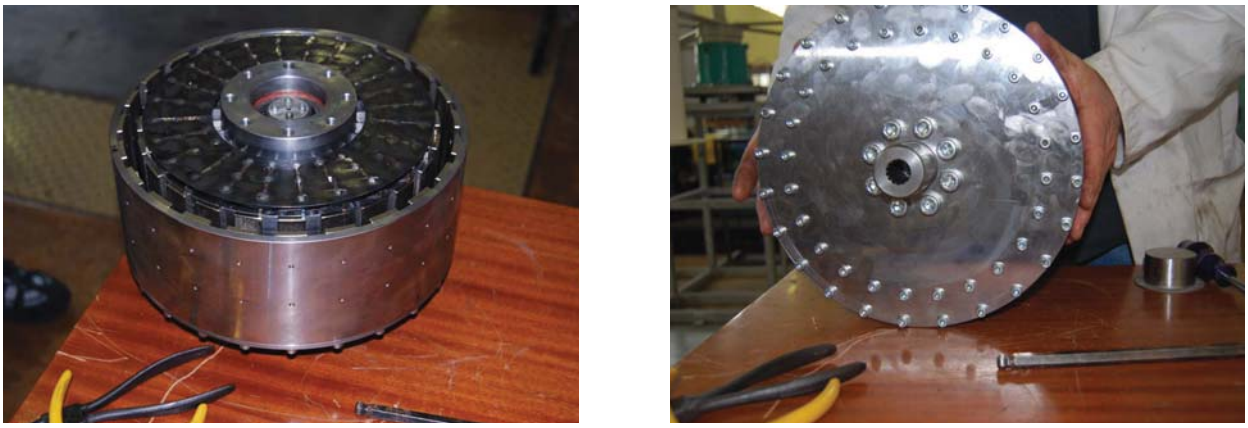

(a) (b)

Figure 4.12: Fully assembled rotor.

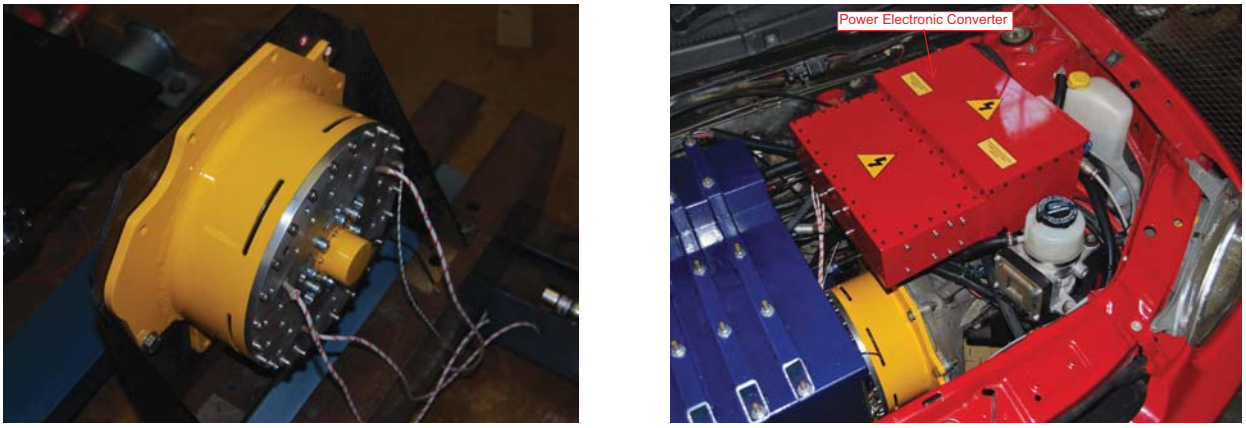

(a) (b)

Figure 4.13: Fully assembled RFAPM machine mounted on a)the test bench and b)the gearbox of the Corsa.

Chapter 5

Power Electronic Inverter and Digital Controller

In this chapter a complete system overview of the power electronic inverter and digital controller is given and the design methodology of this system is discussed in detail.

5.1 System overview

Fig. 5.1 shows a block diagram of the high level system overview of the power electronic inverter and digital controller.

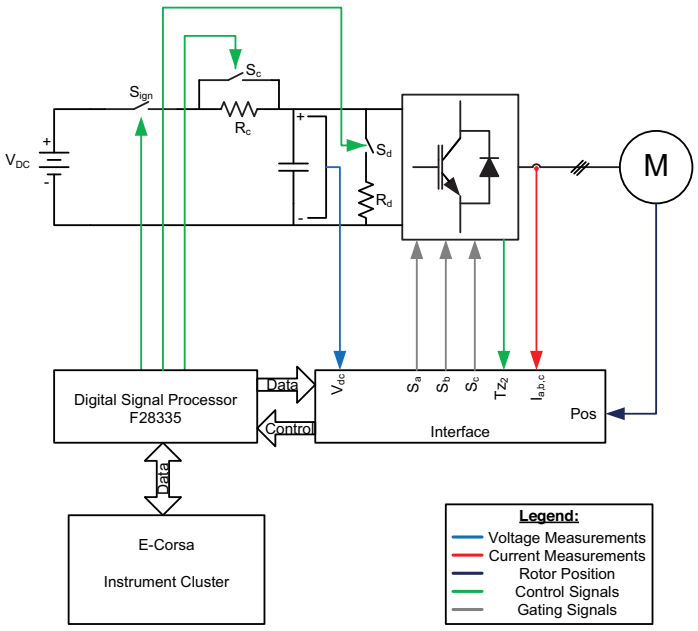

Figure 5.1: High level system overview.

This diagram demonstrates how all the subsystems interact with each other to form a complete drive system for the RFAPM machine. All the main components of the system description are discussed and designed throughout this chapter.

5.2 Switch Gear

5.2.1 Soft start circuit

The purpose of the soft start circuit, shown in Fig. 5.1, is to protect the DC bus capacitors from a sudden in-rush of current when the full DC bus voltage from the battery pack is initially applied. This sudden in-rush of current damages the bus capacitors, thereby, shortening the life span of the capacitors. The principal on which this circuit works will be explained next. Fig. 5.2 shows the layout of the soft start circuit. The ignition of the Corsa is wired in such a way, that when the ignition is turned on, an 45 kW contactor denoted S_{ign} closes to connect the bus voltage of the battery pack to the inverter. The current flowing into the bus capacitors is then limited by a 1 $k\Omega$ resistor, R_c, connected in series with the battery pack. After 20 ms contactor S_c is closed to short out the charging resistor so that normal operation can commence.

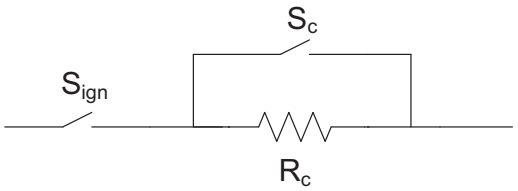

Figure 5.2: Layout of the soft start circuit.

5.2.2 Dumping circuit

Fig. 5.3 shows the layout of the dumping circuit. The purpose of the dumping circuit is serve as protection for the IGBT switches, the DC capacitor bank and the battery pack, in the event of the RFAPM machine operating as generator. The DC bus voltage is constantly measured by the digital controller, and should the DC voltage rise above the allowable 425 V, contactor S_d is closed to discharge the capacitor bank through the dumping resistor R_d. The contactor is again opened as soon as the bus voltage has dropped to 415 V.

The dumping circuit not only serves as protection, but is also responsible for discharging the capacitor bank when the ignition of the vehicle is turned off and S_{ign} opens. The contactor of the dumping circuit is normally closed (NC) so when the ignition is turned off, the contactor automatically closes and the capacitor bank is discharged. The contactor is immediately opened by the digital controller as soon as the ignition of the vehicle is turned on.

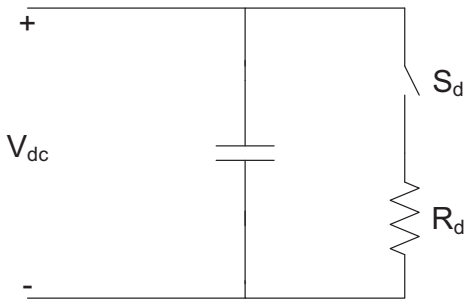

Figure 5.3: Layout of the dumping circuit.

5.3 DC-DC converter

To convert the DC bus voltage of the battery pack to an acceptable voltage that can be used to power the electronic components of the converter, a DC-DC converter is used. For this application, a 600 W Vicor DC-DC converter module is used which has a DC input range of 250-425 V and produces a 24 V DC output. Fig. 5.4 shows the Vicor converter module.

Figure 5.4: 600 W Vicor DC-DC converter module

5.4 Three-Phase DC to AC inverter

A three-phase full bridge inverter topology is used to convert the DC voltage of the battery pack into three-phase AC voltages that is required to drive the RFAPM machine. This full bridge inverter topology is shown in Fig. 5.5. A space vector pulse width modulation (SVPWM) technique (explained in (C.2)) is used to drive the IGBTs of the inverter which generates the desired three-phase output. The voltage and current ratings of the IGBTs needs to be determined to suite the requirements of the drive system. Table 5.1 lists the minimum voltage, current and power requirements of the IGBTs, as determined from the battery pack and RFAPM machine design.

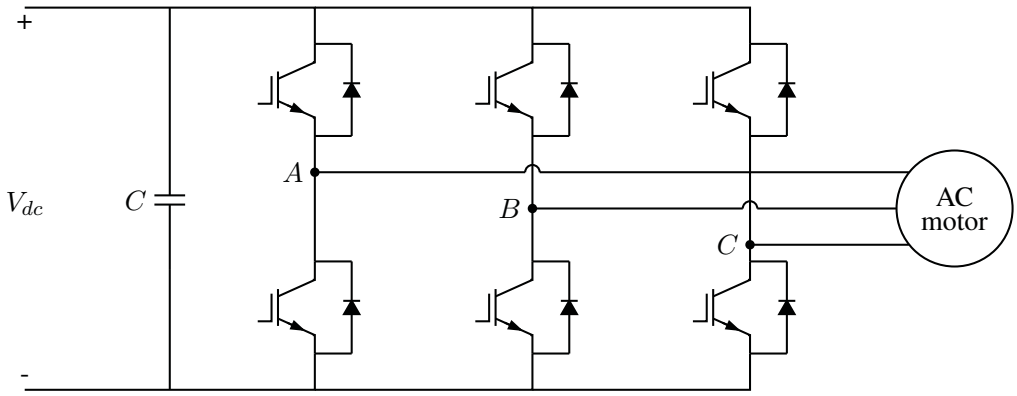

Figure 5.5: Three Phase Inverter.

Table 5.1: Voltage and current ratings for the inverter IGBTs

Inverter Specifications		
Minimum voltage rating	600	(V)
Minimum current rating	100	(A_{RMS})
Minimum power rating	40	(kW)

5.4.1 Intelligent power module (IPM)

To simplify the design process of the inverter, an intelligent power module (IPM) is used. These advance hybrid power modules combine, high speed IGBTs with low losses as well as optimised IGBT gate drive and protection circuitry, into one compact module. The protection circuitry offers under-voltage lockout, short circuit protection, over current protection and over heating protection. IPMs are specifically designed to reduce overall system size, cost and development time. The IPM that was chosen is the PM300CLA060, manufactured by Mitsubishi, which is rated at 600 V and 300 A_{RMS}. The IPM is oversized for the required application, however, this module was the only available IPM at the time to suite the requirements. The IPM is shown in Fig. 5.6.

5.4.1.1 Isolated supply

The IPM has four IGBT gate drive and protection circuits, one for each of the top side switches and one for the low side switches. Each of these four circuits requires an isolated supply voltage of 15-20 V. Isolated supplies are required so that no noise interference, due to high $\frac{dv}{dts}$, exist between these supplies. Therefore, a push-pull converter with a center-tap transformer topology has been chosen for this application. This topology allows for the primary and the four secondary windings to be wound around the same transformer core. The circuit diagram of the push-pull converter is shown in Fig. 5.7. The MOSFETs on the primary side of the transformer are switched by means of a PWM chip at a frequency of 50 kHz with a constant duty cycle of 49%. This high switching frequency is used to minimise

Figure 5.6: The PM300CLA60 IPM.

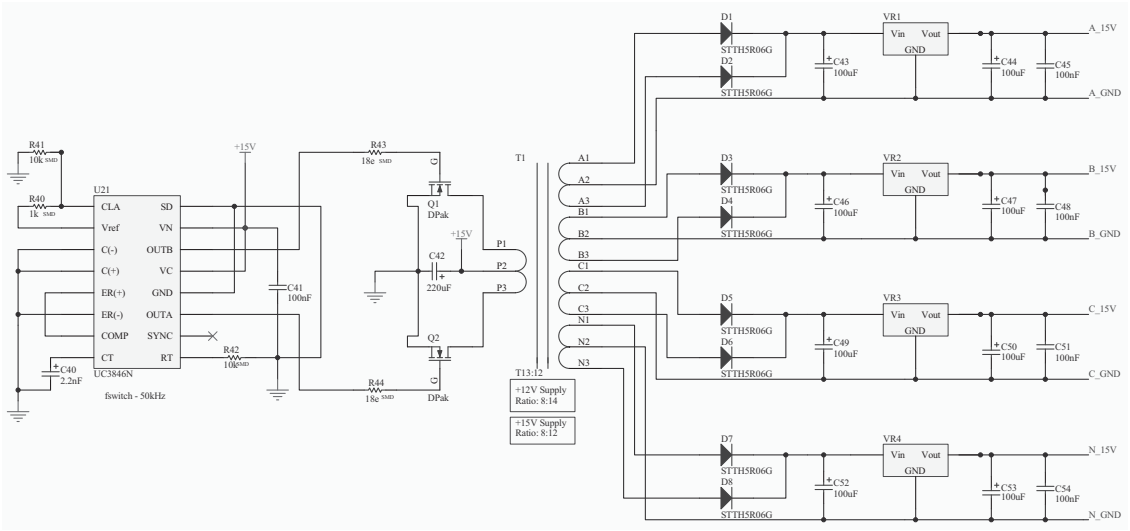

Figure 5.7: Circuit diagram of the push-pull converter.

the size of the transformer. The primary to secondary winding ratio of the transformer is chosen such that a secondary voltage of 20 V is obtained. The number of turns on the primary and secondary windings is 8 and 12 respectively. For the transformer a toroid with N27 core material which has an effective area of 51.26 mm^2 is used. Linear voltage regulators on the secondary side is used to regulate the secondary voltages down to a constant 15 V which is applied to the gate drive and protection circuits of the IPM.

5.4.1.2 Isolation barrier

The PWM switching signals for the IGBTs are generated by the DSP. A direct connection between the DSP and the IPM is not considered due the voltage levels present in the system. An isolation barrier is, therefore, required between the DSP and the IPM. The gate drive signals generated by the DSP are optically transmitted over this isolation barrier with optical gate drivers. The gate driver that was chosen for this application is the HCPL-4506, which has a continuous isolation rating of 1.4 kV

5.4.2 PCB layout of the isolated supply and isolation barrier

Fig. 5.8 shows the PCB layout of the isolated supply and the isolation barrier of the IPM controller circuit.

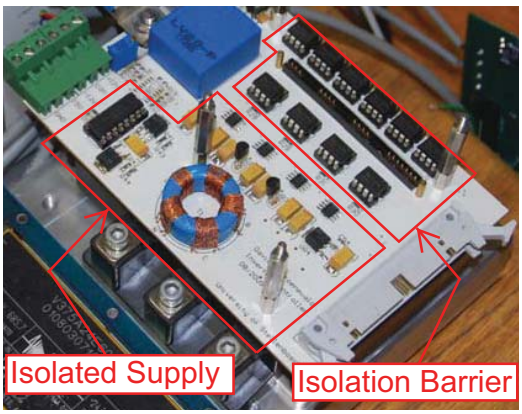

Figure 5.8: PCB layout of the isolated supply and isolation barrier.

5.4.3 DC bus capacitors

As stated before, the role of the inverter is to convert the DC voltage of the battery pack to three-phase AC voltages. This conversion is however not ideal. The operation of a typical switching mode inverter leads to alternating currents on the DC bus at harmonics associated with the switching frequency. The DC bus capacitors of the inverter are required to reduce these ripple currents on the DC supply and keep the DC supply stable. Also, a snubber capacitor which is connected in parallel with IGBTs is required to absorb the voltage spikes which are cause by the circuit inductance when the IGBTs are switching.

For the DC bus capacitor bank, a metallized polypropylene film capacitor, manufactured by iCEL, with a capacitance of 20 μF has been chosen. This capacitor has a voltage rating of 500 V with a peak voltage and current rating of 625 V and 1300 A, respectively. These capacitors have a very low equivalent series resistance (ESR) of 3.2 $m\Omega$ and, therefore, minimum power is dissipated inside the capacitor. The capacitor bank consists of 12 of these capacitors which are all connected in parallel to give a total bus capacitance of 480 μF. For the snubber capacitor, a metallized polypropylene film capacitor has also been chosen which has a capacitance of 1 μF and a voltage rating of 1000 V. The DC bus capacitors and the snubber capacitor which are connected to the IPM is shown in Fig.5.9.

5.4.4 Inverter switching frequency

High switching frequencies in inverters are desirable in AC drive motor applications as it allows for fast current control to be performed, resulting in a high dynamic system performance. Also, higher switching frequencies can drastically reduce load current ripples.

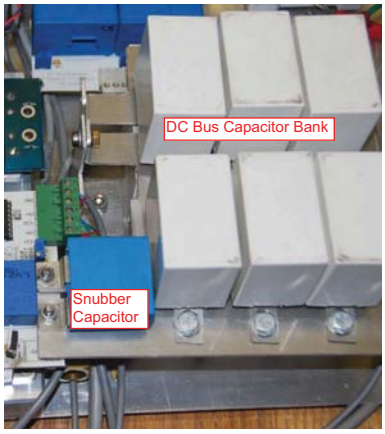

Figure 5.9: Photo of the DC bus capacitors and the snubber capacitor.

However, higher switching frequencies result in higher inverter losses which is discussed in the following subsection.

To investigate the result of various inverter switching frequencies on the ripple current of the RFAPM machine, a simulation model of the inverter with the RFAPM machine as load is implemented in *Simulink*®. The results obtained for 5, 10, 15 and 20 kHz switching frequencies are shown in Fig. 5.10. It is clear from the simulation results that a switching frequency under 20 kHz will result in high load ripple currents. A switching frequency of 20 kHz is, therefore, used.

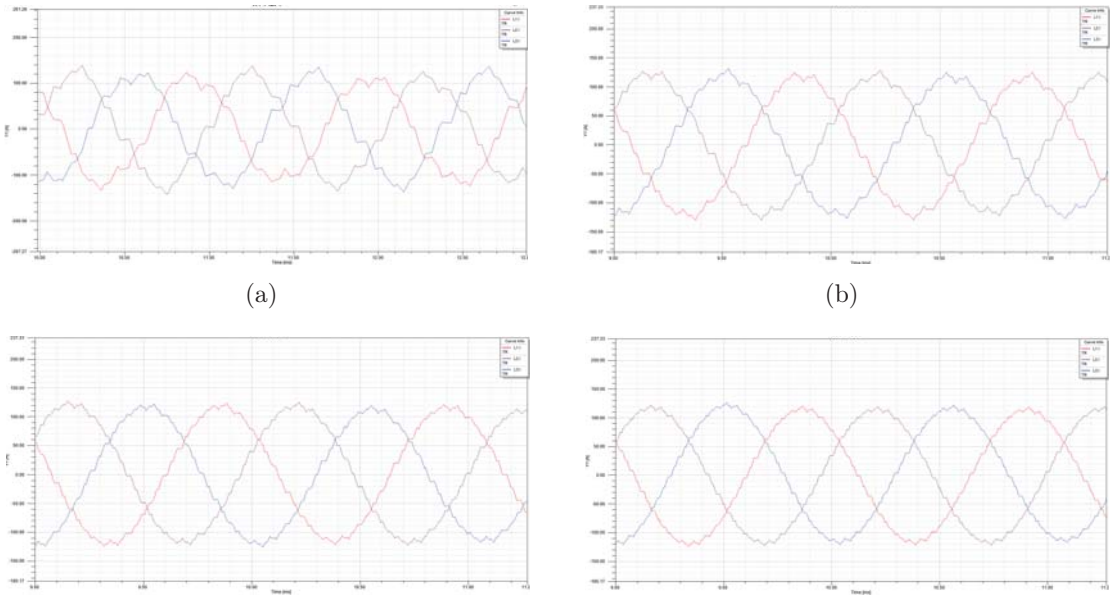

Figure 5.10: Switching frequencies: (a) 5 kHz; (b) 10 kHz; (c) 15 kHz; (d) 20 kHz

5.4.5 Switching and conduction losses of the inverter

The losses in inverters are comprised of passive component losses as well as switching component losses. Passive losses mainly include the conduction losses occurring in the load inductance and capacitance. Switching component losses are the losses dissipated in the diodes and IGBTs [10]. Switching component losses are further subdivided into switching and conduction losses. It is therefore necessary to do a theoretical switching loss calculation for the design of the inverter, as the optimisation of the drive system and heatsink for the inverter is dependant on the accuracy of the loss calculations. The theoretical calculation of the inverter losses are derived in detail in Appendix B.

The design specifications of the three-phase inverter and the IGBT specifications of the PM300CLA060 power module are listed in Table 5.2. By applying the applicable parameters from Table 5.2 to eqns. (B.1.3), (B.2.1) and (B.3.2) yield the losses of the inverter, which are listed in Table 5.3.

Table 5.2: Inverter and IGBT specifications

Inverter Parameters	
$I_{o(RMS)} = 97.3$ A	$I_o = I_{o(RMS)} \cdot \sqrt{2}$ A
$V_{DC} = 338$ V	$m_a = 0.8$
$L_q = L_d = L = 27\ \mu$ H	$f_s = 20$ kHz
IGBT Parameters	
$V_{CE(max)} = 600$ V	$I_C = 300$ A
$V_{on} = 0.6$ V	$V_{f(diode)} = 2$ V
$t_{on} = 55$ ns	$t_{off} = 90$ ns
$E_{RRmax} = 10.6$ mJ	$r_{ce} = 4.2$ mΩ

Table 5.3: Calculated inverter losses

Calculated Inverter Losses		
Loss Component:	Symbol:	Value:
Switching Losses	P_{sw}	21.37 W
Conduction Losses	P_{cond}	37.84 W
Diode Losses	P_{diode}	16.19 W
Total Losses	$P_{inverter}$	580.2 W
Inverter efficiency	$\eta_{inverter}$	98.2 %

5.5 Liquid cooled heatsink

A liquid cooling method has been proposed for the cooling of the inverter power module and the DC-DC converter. Liquid cooling methods have several advantages over air cooling methods such as:

- Higher heat transfer coefficients from the component to the coolant
- Require much smaller space and thus result in compact packaging
- Prevent power components from contamination by humidity and dust
- Reduce the noise level, which is important for the EV.

The design of the heatsink is beyond the scope of this project and a specialist was consulted for the design. Fig. 5.11 shows the two part aluminium water cooled heatsink with the IPM and DC-DC converter mounted on the heatsink.

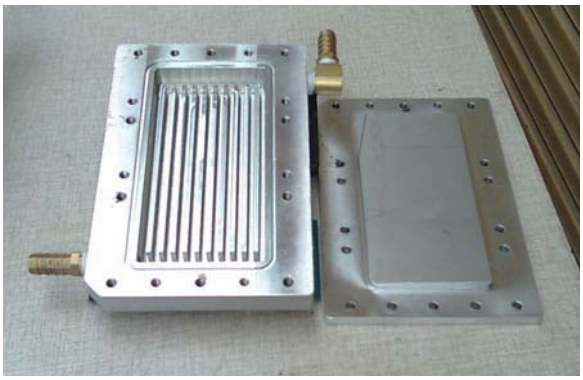

(a) Aluminium water cooled heatsink.

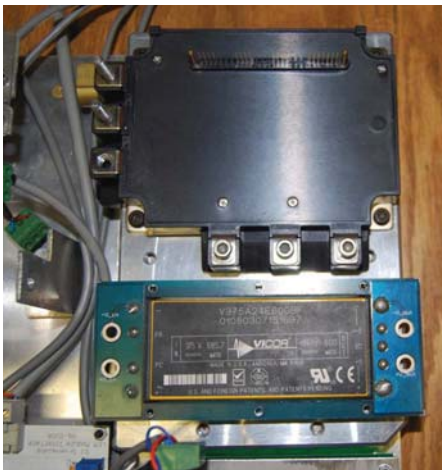

(b)

Figure 5.11: Photo of the water cooled aluminium heasink.

5.6 Voltage, current and rotor position measurement

In this section the components that are use for the voltage, current and rotor position measurement are described. Fig. 5.12 shows the PCB design of the measurement circuits which are discussed next.

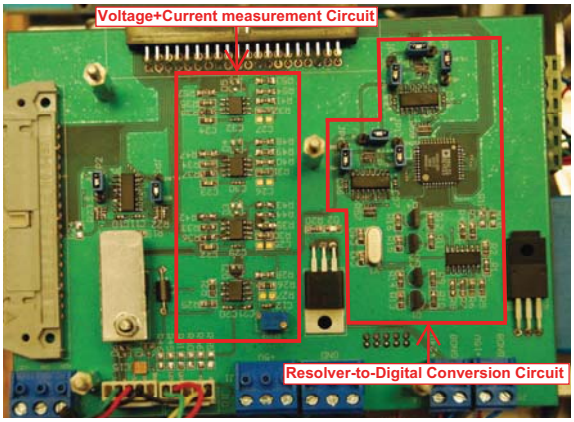

Figure 5.12: PCB of the voltage, current and rotor position measurement circuits.

5.6.1 Voltage and current measurements

Measurement of the three-phase currents are required to perform current control on the RFAPM machine. Due to the RFAPM machine being a balanced three-phase system, it is only necessary to measure two of the phase currents, as the current of the third phase can be calculated from the two measured currents. It is furthermore necessary to measure the DC bus voltage which is required by the space vector modulation algorithm. The DC bus current is also measured and with the DC bus voltage measurement available, it is possible to make a rough estimation of the state of charge (SOC) of the battery pack.

Both voltage and current measurements are measured by means of $LEM^{®}$ hall-effect sensors. These sensors offer galvanic isolation between its primary (high voltage) and secondary (low voltage) of 2.5 kV. For the measurement of the DC bus voltage, a LV 25-P $LEM^{®}$ voltage transducer is used. This voltage transducer is capable of measuring DC and AC voltages upto 500 V. For measuring the DC and AC currents, a LA 125-P $LEM^{®}$ current transducer is used. This current transducer is capable of measuring a nominal current of 125 A_{RMS}. The voltage and current measurement sensors are described in detail in Appendix D.

5.6.2 Rotor position and speed measurement

A resolver is a position sensor which is used to measure the instantaneous mechanical angular position, θ, of a rotating shaft to which it is attached. Resolvers are rotating transformers typically with a primary winding on the rotor and two secondary windings on the stator which are mechanically displaced by 90°, as depicted in Fig. 5.13. Please refer to Appendix D for a complete discussion on the operation of the resolver.

Practical implementation

To simplify the integration between the analog resolver and the digital microcontroller an AD2S1205 12-bit resolution resolver-to-digital converter chip is used. This converter contains an on-board sinusoidal oscillator which generates a 10 kHz primary excitation signal for the

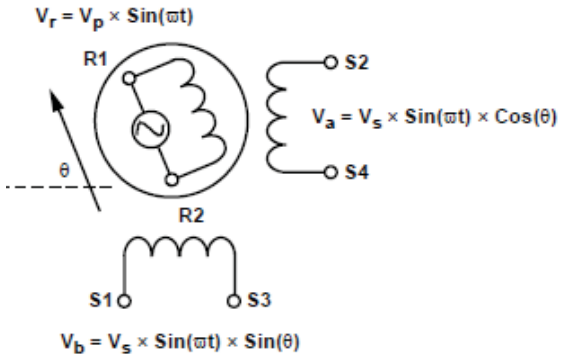

Figure 5.13: Illustration of a conventional resolver [4].

resolver. The return signals from the resolver's secondary output voltages is sampled by the converter at a sampling rate of 64 kHz, which then calculates the absolute angular position and the speed of the rotor shaft. The microcontroller can accesses the 12-bit angular position and speed data via the 12-bit parallel port of the converter chip. The converter also provides noise immunity and tolerance of harmonic distortion on the reference and input signals. The connection diagram of the resolver-to-digital converter chip is shown in Fig. 5.14.

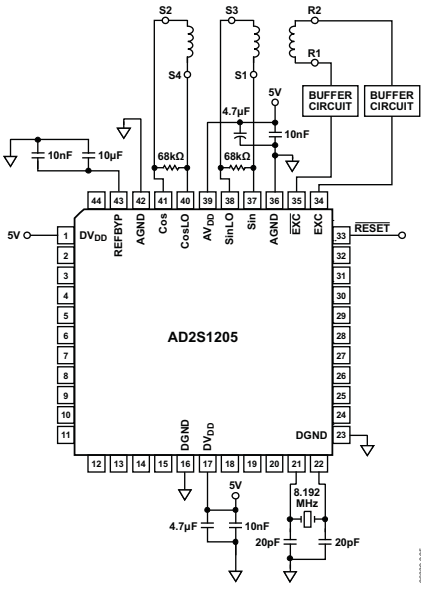

Figure 5.14: Connection diagram of the resolver-to-digital converter.

5.7 Digital Signal Processor (DSP)

The purpose of the DSP is to form an integration platform between all the subsystems described above. The DSP is responsible for taking the voltage, current and rotor position

measurements and execute the control loop for the RFAPM machine, based on these measurements. An $eZdsp^{TM}$ F28335 floating point DSP from Texas Instruments has been chosen for this application. The peripherals of the DSP are listed below.

- 150 MHz operating frequency
- 12 PWM channels which can be configured as 6 complimentary pairs
- Adjustable dead time generation for the PWM signals
- 16 ADC channels with 12-bit resolution
- 2 CAN modules

Fig. 5.15 shows the F28335 floating point DSP. The source code of the DSP control program are listed in Appendix E an can be found on the companion CD.

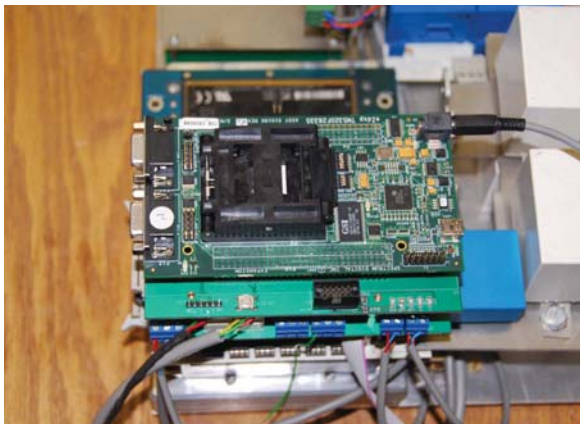

Figure 5.15: Photo of the $eZdsp^{TM}$ F28335 floating point DSP

5.8 Assembly and packaging of the power electronic converter

Fig. 5.16 shows the power electronics which is packaged and mounted inside the engine bay of the E-Corsa. The complete power electronic converter system is designed and developed as part of this project, and the testing of the converter is described in Chapter 7.

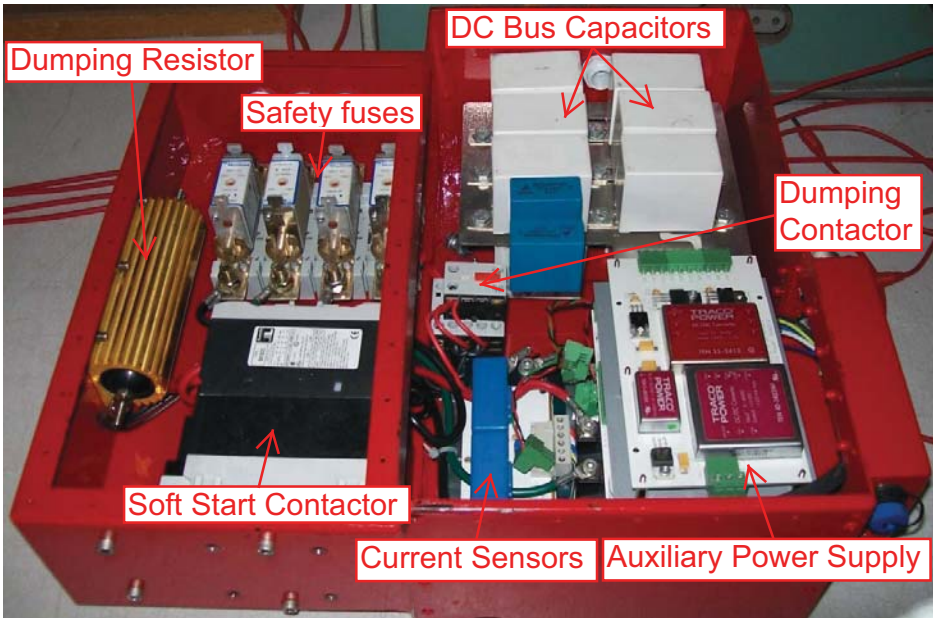

(a)

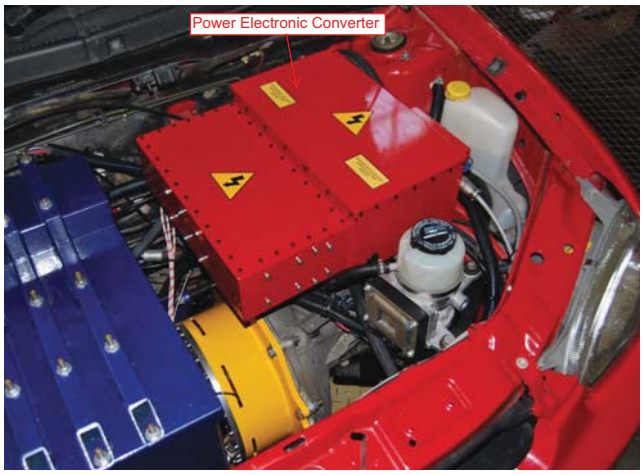

(b)

Figure 5.16: Packaged power electronic converter.

Chapter 6

dq Current Controller Design of the RFAPM Machine Drive

In this chapter the design of a dq current controller for the RFAPM machine is described. An accurate dq equivalent model for the RFAPM machine is derived which is used to design the controller. The current controller is then implemented into a *MATLAB® Simulink®* model to simulate and evaluate the design.

6.1 Overview of the dq current controller design strategy

In this section a brief overview on the dq current control system and the process that will be followed for the current controller design of the RFAPM are given.

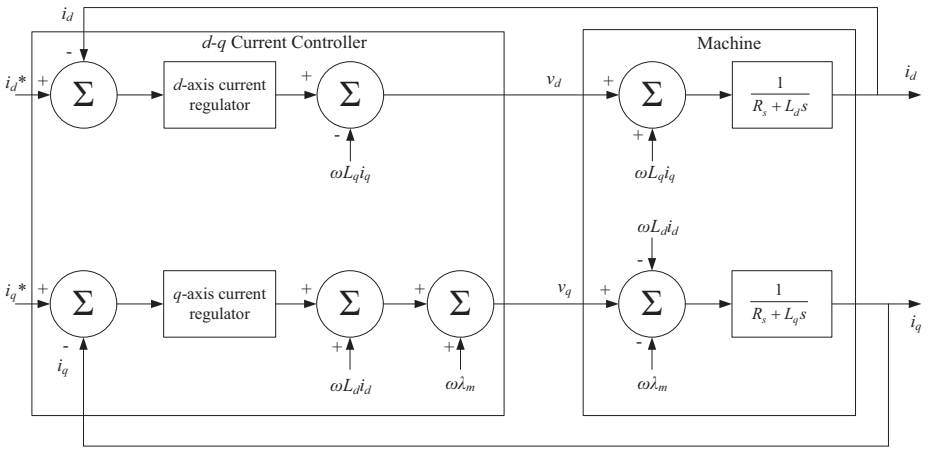

Figure 6.1: Block diagram representation of the dq current control system of the RFAPM machine.

The dq current control system can be represented by the block diagram shown in Fig. (6.1). In the block diagram the dq current regulators respond on the feedback errors between desired and actual (measured) dq currents of the machine. The speed voltage terms are added or subtracted to the outputs of the current regulators to yield the dq machine voltages. Within the machine model the speed voltages are subtracted or added again, hence the regulators respond only on the RL-parts of the equivalent circuits [9].

To design the dq current controllers for the current control system as discussed above, the following steps will be followed

1. Derive the dq equivalent models of the machine
2. Determine the d and q-axis transfer functions
3. Determine the open loop current response from the d and q-axis models
4. Design the dq current regulators to obtain the desired dq current response

6.2 dq Equivalent models of the RFAPM machine

The derivation of a mathematical model for the RFAPM machine, starts with the induced phase voltage equation given by Faraday's law as

$$v_{ABC} = r_s i_{ABC} + \frac{d\lambda_{ABC}}{dt} \tag{6.2.1}$$

where v_{ABC}, r_s, i_{ABC} and λ_{ABC} are the induced phase voltage, armature winding resistance, armature current and stator magnetic flux linkage of phase A, B or C respectively [9]. These circuit variables are expressed in a reference frame that is fixed to the stator or the so-called ABC reference frame. For synchronous machines it is convenient to transform the stator variables from this stationary ABC reference, to a reference frame that is fixed to the rotor. This transformation replaces the stationary ABC stator windings of the machine, with fictitious *dq0* windings that rotate with the rotor and is dependant on the position of the rotor. By using Park transformation (see Appendix C), the voltage equations in the dq0 reference frame, which is fixed to the rotor, are given by [11]:

$$v_d = r_s i_d + \frac{d\lambda_d}{dt} - \omega\lambda_q \tag{6.2.2}$$

$$v_q = r_s i_q + \frac{d\lambda_q}{dt} + \omega\lambda_d \tag{6.2.3}$$

where the d- and q-axis flux linkages, λ_d and λ_q are defined as

$$\lambda_d = L_d i_d + \lambda_f \tag{6.2.4}$$

$$\lambda_q = L_q i_q \tag{6.2.5}$$

with,

- v_d and v_q the d- and q-axis components of the terminal voltage
- λ_f the maximum flux linkage per phase produced by the permanent magnets
- L_d and L_q are the d- and q-axis components of the armature self-inductance, and are referred to as synchronous inductances
- $\omega = 2\pi f$ is the angular frequency of the armature current
- i_d and i_q are the d- and q-axis components of the armature current

From (6.2.4), the magnetic flux linkage λ_f can be further expressed as

$$\lambda_f = L_d i_f = \lambda_{pm} \tag{6.2.6}$$

where i_f is a fictitious magnetising current representing the PM excitation.

By substituting eqns (6.2.4), (6.2.5) and (6.2.6) into eqns (6.2.2) and (6.2.3), the stator voltage equations in the d and q-axis can be written as

$$v_d = r_s i_d + \frac{di_d}{dt} L_d - \omega L_q i_q \tag{6.2.7}$$

$$v_q = r_s i_q + \frac{di_q}{dt} L_q + \omega L_d i_d + \omega L_d i_f \tag{6.2.8}$$

From (6.2.7) and (6.2.8) the complete dq equivalent circuits of the sinusoidal RFAPM machine can be drawn as shown in Fig. **??**. The modelling according to eqns (6.2.7) and (6.2.8) is based on the assumptions that [9]:

- there are no core and eddy current losses
- there is no cross magnetisation or mutual coupling between the d- and q-axis circuits

6.3 Current controller design

6.3.1 Theory on digital controllers

Various methods exists for designing a digital control system. Issues with digital control systems is that the output signal of the digital controller has to be transformed from a discrete signal to a continuous signal. This is accomplished by a sample and hold element at the output of the controller, which holds the output of the controller constant for one sampling period. The zero order hold (ZOH), however, introduces a delay of half the sampling period.

One method for designing a digital control system is, *design by emulation*. This method requires the sampling frequency to be at least ten times that of the closed loop bandwidth of the system. First the controller is designed in the continuous-time domain with an S-plane

representation and then transformed to a discrete-time domain representation in the Z-plane. The transformation between the S-plane and Z-plane is done by using any of the following methods; *Backwards Euler, Tustin's method or Matched pole-zero*. When this method of controller design is used, it is assumed that the delay introduced by the ZOH is negligible.

A second method to design the controller is to design the controller completely in the Z-plane. This method involves transforming both the plant and the ZOH to their respective discrete equivalents. This method introduces no time delay as this is accounted for by the transformation.

The third method involves transforming the discrete equivalent of both the ZOH and the plant to the, so called, W-plane by using a bilinear transformation [12] shown below.

$$z \rightarrow \frac{1 + \frac{T_s}{2}w}{1 - \frac{T_s}{2}w}$$

The W-plane takes the effect of the ZOH into account, which makes it possible to use frequency response techniques such as Bode plots [12]. The whole control system can therefore be designed in the W-plane and then transformed back to the Z-plane by using the inverse W-transform shown below.

$$w \rightarrow \frac{2}{T_s}\frac{z-1}{z+1}$$

A combination of the methods discussed are used to design the current controller for the RFAPM machine.

6.3.2 Open loop current response

Using the decoupled models for the d-axis and q-axis plant, it is possible to determine the open loop current response of the RFAPM machine. The bandwidth of the machine can easily be determined by obtaining the Bode plot or root locus for the plant. Since the d- and q-axis inductances of the RFAPM machine are assumed to be equal (i.e $L_d = L_q$), the open loop current response of the d-axis and q-axis plants are the same. Therefore, by using either of the decoupled d-axis or q-axis plants the step response and Bode plot for the plant can be determined as follows:

Figure 6.2: The d- and q-axis transfer functions.

For example, the decoupled q-axis plant is given by:

$$\frac{i_q}{v_q} = \frac{1}{L_q \cdot s + r_s} \tag{6.3.1}$$

From Table 4.3 in Chapter 4, $r_s = 24m\ \Omega$ and $L_q = 27\ \mu H$. By substituting these values into eqn (6.3.1), yields a single pole at $-\frac{r_s}{L_q} = 888.89$. The open loop step response and Bode plot for this plant is shown in Fig. 6.3. From Fig. 6.3 it can be determined that the response

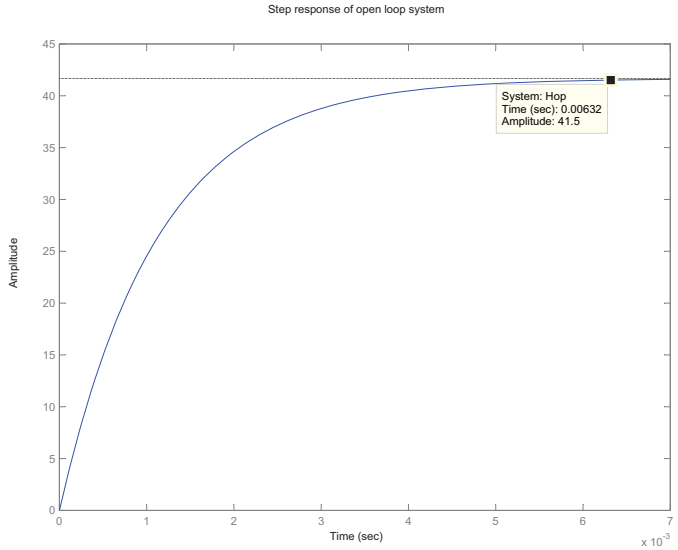

(a)

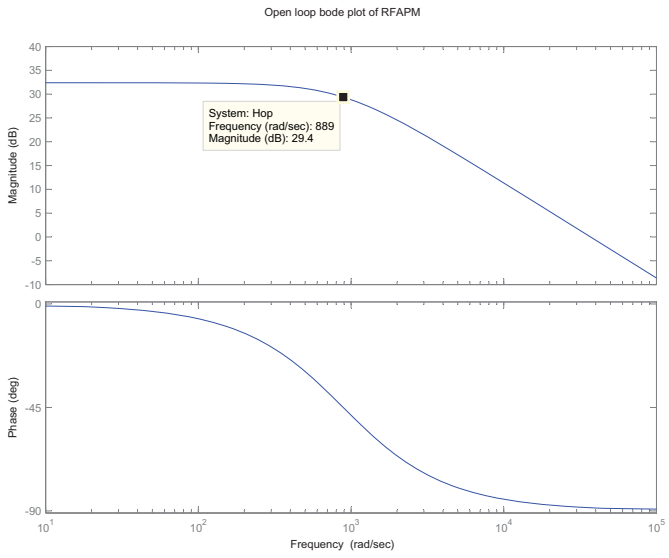

(b)

Figure 6.3: Open loop q-axis plant: (a) step response; (b) Bode plot.

of the plant to a step input is: $\tau_s = 0.00632$ sec and the bandwidth of the open loop system is shown to be 889 rad/sec, which corresponds to the single pole position calculated at 888.89.

The next step is to design a closed loop system, with a feedback from the plant to the controller to increase the bandwidth and the step response of the system.

6.4 Current controller design in the W-plane

Before the current controller can be designed, the concept of controller instability needs to be explained. Designing the current controller in the W-plane it is required that with a sampling frequency of ω_s, the frequency of the input signal to the controller must have a frequency of less than $\frac{\omega_s}{2}$, according to the Nyquist frequency. The single pole determined in Section (6.3.2) introduces a 90° phase delay and another 90° phase delay is introduces by the ZOH at $\frac{\omega_s}{2}$ [11]. This accounts to a total phase delay of 180° at $\frac{\omega_s}{2}$. If the loop gain of the controller is 1 (or 0 dB) at $\frac{\omega_s}{2}$ instability will occur, because the closed loop response of the system will strive to infinity as shown below.

$$\begin{aligned} \frac{1\angle 180}{1+1\angle 180} &= \frac{1}{0} \\ &= \infty \end{aligned}$$

By choosing the loop gain to be -10 dB at $\frac{\omega_s}{2}$ will give a gain margin of 10 dB, and will insure stability of the controller.

The design of the current controller in the W-plane proceeds as follows:

- Start with the transfer function for the open loop plant in the continuous domain.
- Transform the transfer function to a discrete domain transfer function and include the effect of the ZOH.
- Use the W-transform to transform the discrete domain transfer function back to the continuous domain.
- The controller is chosen to be only a proportional (P) controller and not a proportional integral (PI) controller. The controller gain is computed so that the loop gain is -10 dB at $\omega = \infty$ rad/sec.
- The designed controller is transformed back to the discrete domain using the inverse W-transform, but since it is only a constant, no transformation is needed.

The S-plane representation of the continuous plant model is given by:

$$G_{ds}(s) = \frac{1}{L_q \cdot s + r_s} \tag{6.4.1}$$

Transforming the continuous plant model from the S-plane representation to the Z-plane representation, the sampling period of the discrete signal is required. The sampling frequency

is $f_s = 20kHz$ which gives a sampling period of $T_s = 50\ \mu s$. With this, the discrete transfer function of the plant [12] is

$$\begin{aligned} G_{dz}(z) &= (1-z^{-1})Z\left\{ \frac{G_{ds}(s)}{s} \right\} \\ &= (1-z^{-1})Z\left\{ \frac{1}{s}\cdot\frac{1}{r_s+sL_q} \right\} \\ &= \frac{1-e^{-\frac{r_sT_s}{L_q}}}{r_s(z-e^{-\frac{r_sT_s}{L_q}})} \end{aligned} \tag{6.4.2}$$

Using the W-transform, (6.4.2) can be accurately mapped back to the continuous domain because the W-transform is a trapezium approximation to integration. The W-transform [12] is given by

$$z = \frac{1+\frac{T_s}{2}w}{1-\frac{T_s}{2}w} \tag{6.4.3}$$

The plant's open loop transfer function in the continuous domain, which includes the effect of the ZOH is obtained by substituting (6.4.3) into (6.4.2) which yields:

$$G_{dw}(w) = \frac{1-e^{-\frac{r_sT_s}{L_q}}}{r_s\left\{ \frac{1+\frac{T_s}{2}w}{1-\frac{T_s}{2}w} - e^{-\frac{r_sT_s}{L_q}} \right\}} \tag{6.4.4}$$

The behaviour of the system described by (6.4.4) can be evaluated at the Nyquist frequency, $\omega = \frac{\omega_s}{2}$, by letting $w = \infty$.

$$\begin{aligned} G_{dw}(\infty) &= \frac{1-e^{-\frac{r_sT_s}{L_q}}}{r_s\left\{ \frac{1+\frac{T_s}{2}\infty}{1-\frac{T_s}{2}\infty} - e^{-\frac{r_sT_s}{L_q}} \right\}} \\ &= \frac{1-e^{-\frac{r_sT_s}{L_q}}}{r_s(-1-e^{-\frac{r_sT_s}{L_q}})} \end{aligned} \tag{6.4.5}$$

The controller gain K_q, should be chosen such that the loop gain of the controller is -10 dB at the Nyquist frequency. The controller gain can be calculated as follows

$$20\log_{10}\left\{ K_q\cdot\left| \frac{1-e^{-\frac{r_sT_s}{L_q}}}{r_s(-1-e^{-\frac{r_sT_s}{L_q}})} \right| \right\} = -10 \tag{6.4.6}$$

Solving (6.4.6) for K_q yields:

$$\begin{aligned} K_q &= 10^{-10/20}\cdot\left| \frac{r_s(-1-e^{-\frac{r_sT_s}{L_q}})}{1-e^{-\frac{r_sT_s}{L_q}}} \right| \\ &= 10^{-10/20}\cdot r_s\cdot\frac{1+e^{-\frac{r_sT_s}{L_q}}}{1-e^{-\frac{r_sT_s}{L_q}}} \\ &= 10^{-10/20}\cdot r_s\cdot\coth\left\{ \frac{r_sT_s}{2L_q} \right\} \\ \Rightarrow\ K_q &= \frac{10^{-10/20}\cdot r_s}{\tanh\left\{ \frac{r_sT_s}{sL_q} \right\}} \end{aligned} \tag{6.4.7}$$

Evaluating the above controller design from eqn (6.4.1) through to eqn (6.4.7) for $r_s = 24\ m\Omega$, $L_q = 27\ \mu H$ and $T_s = 50\ \mu s$ yields:

The continious transfer function,

$$\begin{aligned} G_{ds}(s) &= \frac{1}{L_q \cdot s + r_s} \\ &= \frac{1}{0.000027s + 0.024} \end{aligned}$$

The discrete transfer function,

$$\begin{aligned} G_{dz}(z) &= \frac{1 - e^{-\frac{r_s T_s}{L_q}}}{r_s(z - e^{-\frac{r_s T_s}{L_q}})} \\ &= \frac{0.9160}{z - 0.9780} \end{aligned}$$

Transformation of the discrete transfer function back to the continuous domain,

$$\begin{aligned} G_{dw}(w) &= \frac{1 - e^{-\frac{r_s T_s}{L_q}}}{r_s \left\{ \frac{1+\frac{T_s}{2}w}{1-\frac{T_s}{2}w} - e^{-\frac{r_s T_s}{L_q}} \right\}} \\ &= \frac{0.9160}{\frac{1+0.0000125w}{1-0.0000125w} - 0.9160} \end{aligned}$$

The continuous plant in the W-plane, at the Nyquist frequency,

$$G_{dw}(\infty) = -\frac{0.02196}{0.05747}$$

$$\angle G_{dw}(\infty) = 180^\circ$$

$$|G_{dw}(\infty)|_{dB} = 20log\left| -\tfrac{0.02196}{0.05747} \right| = -8.35\ dB$$

The controller gain K_q,

$$\begin{aligned} K_q &= \frac{10^{-10/20} \cdot r_s}{\tanh\left\{ \frac{r_s T_s}{s L_q} \right\}} \\ &= 0.6831 \end{aligned}$$

The results obtained above can be verified with the aid of $MATLAB^{®}$. The $MATLAB^{®}$ code is listed below which verifies the results obtained above, followed by the continuous domain Bode plot in the W-plane.

```
>> Gs = tf([1],[27e-6 24e-3])

Transfer function:
        1
------------------
2.7e-005 s + 0.024

>> Gz = c2d(Gs,1/40000,'zoh')

Transfer function:
 0.9157
---------
z - 0.978

Sampling time: 2.5e-005

>> Gw = d2c(Gz,'tustin')

Transfer function:
-0.4629 s + 3.704e004
---------------------
      s + 888.9
```

Create the continuous transfer function of the plant,
Discretize the continuous transfer function and include the effect of the ZOH,
Transform the discrete transfer function back to the continuous domain using Tustin's method,
The Bode plot in Fig. 6.4 shows the plant which is scaled with the controller gain $K_q = 0.6831$. It is clear from this Bode plot that the gain of the system is -10 dB at the Nyquist frequency, which guarantees controller stability as explained earlier in this section.

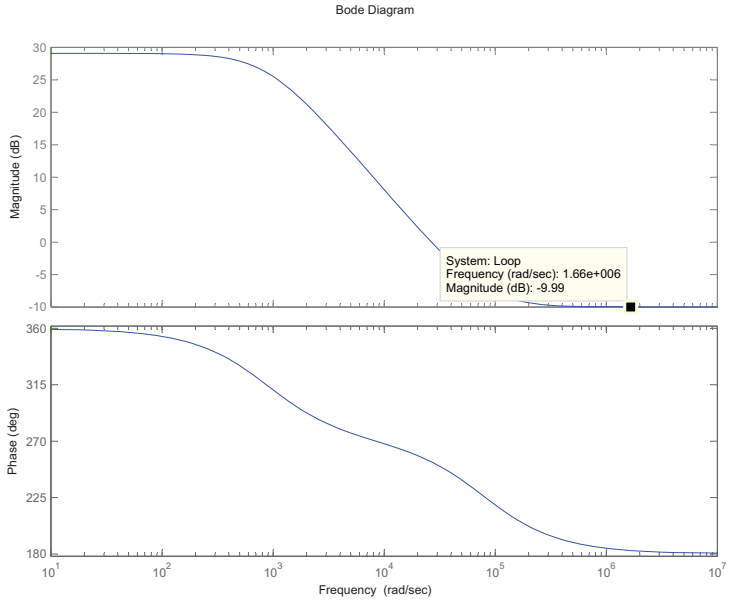

Figure 6.4: Bode plot of the continuous q-axis plant and controller in the W-plane.

6.5 Simulation of the current controller

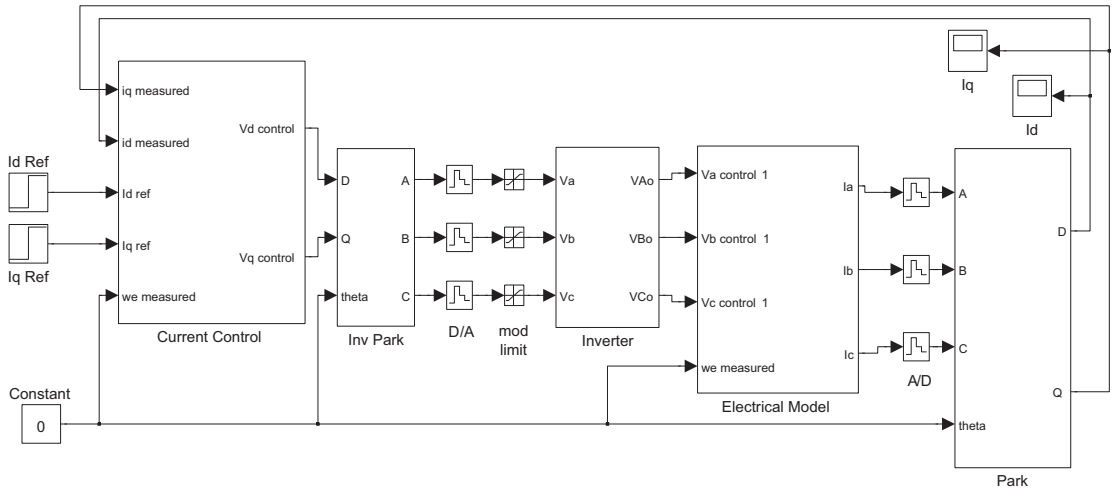

Figure 6.5: Simulation model of the current controller with the inverter and Park transformations.

The complete simulation model of the current controller, which includes the model for the inverter, the electrical model of the RFAPM machine and the Park transformations is shown in Fig. 6.5. The *Simulink*® simulation model can be found on the companion CD. The dead time for the inverter is set to 2 μs, the DC bus voltage is set to 338 V and the modulation index of the inverter is set to 0.9. The speed reference input is set to zero to simulate a lock rotor test.

To obtain the simulation results the d-axis current reference is first set to zero while the q-axis current reference is set to 100 A. In the next step the q-axis current reference is set to zero while the d-axis current reference is set to 100 A. The simulation results are shown in Fig. 6.6. From Fig. 6.6, the current response times for the d and q-axis plants are $\tau_s \simeq 1\ ms$ which is more than satisfactory for an application such as the EV. It can also be seen that both currents respond to their reference inputs.

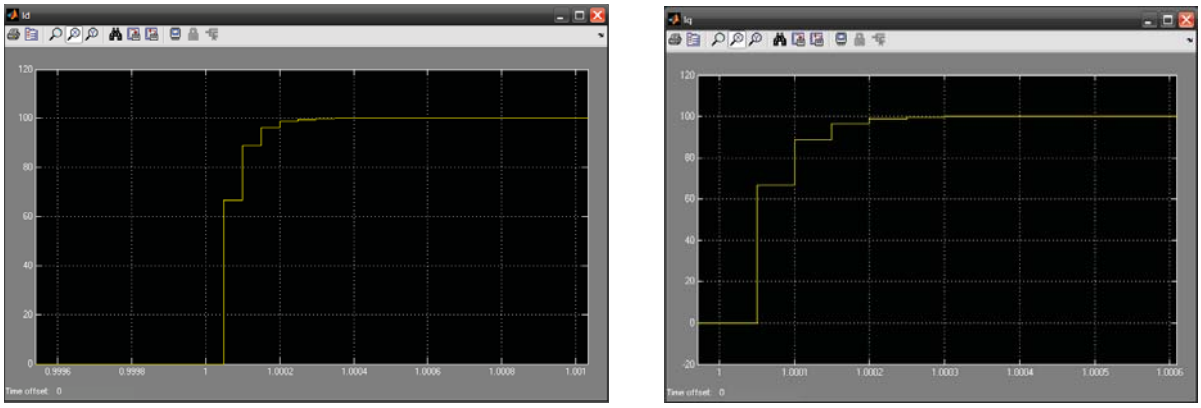

(a) d-axis (b) q-axis

Figure 6.6: Step response of the d and q-axis current controllers.

Chapter 7

Tests and Measurements

In this chapter the experimental results obtained from test bench measurement on both the power electronic converter and the RFAPM drive are presented. Also, a brief interpretation of each result is included.

7.1 Test bench layout

Fig. 7.1 shows the practical setup of the test bench. The RFAPM drive motor is connected via a 200 Nm torque sensor to a dynamometer, which provides the load to the RFAPM drive motor. A DC motor, rated at 2.2 kW and 2800 rpm, is also mounted and connected to the opposite side of the dynamometer, so that certain generator tests can be performed on the RFAPM motor.

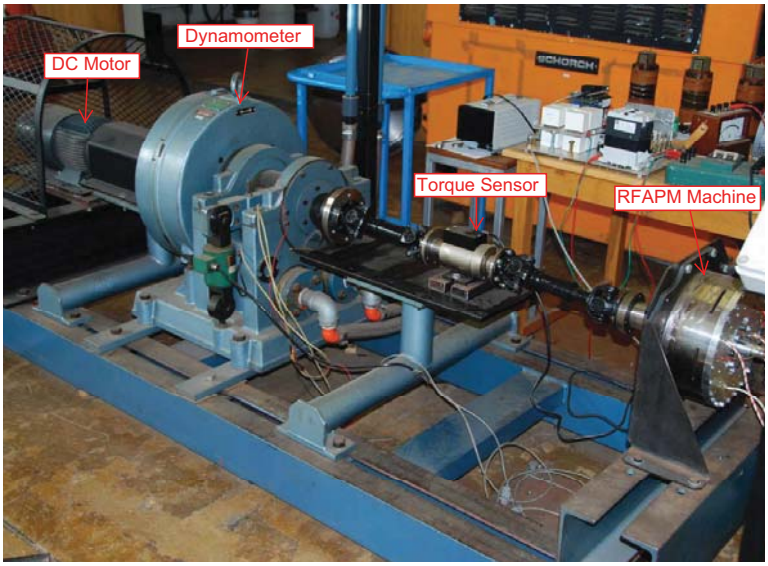

Figure 7.1: Test bench setup in the laboratory.

7.2 Power Electronic Converter Tests

In this section various experimental tests and measurements are performed on the power electronic converter.

7.2.1 Rotor position measurement

The measurements of the mechanical and electrical rotor position are shown in Fig. 7.2. The electrical position of the rotor is obtained by multiplying the mechanical rotor position with the number of pole pairs of the RFAPM drive.

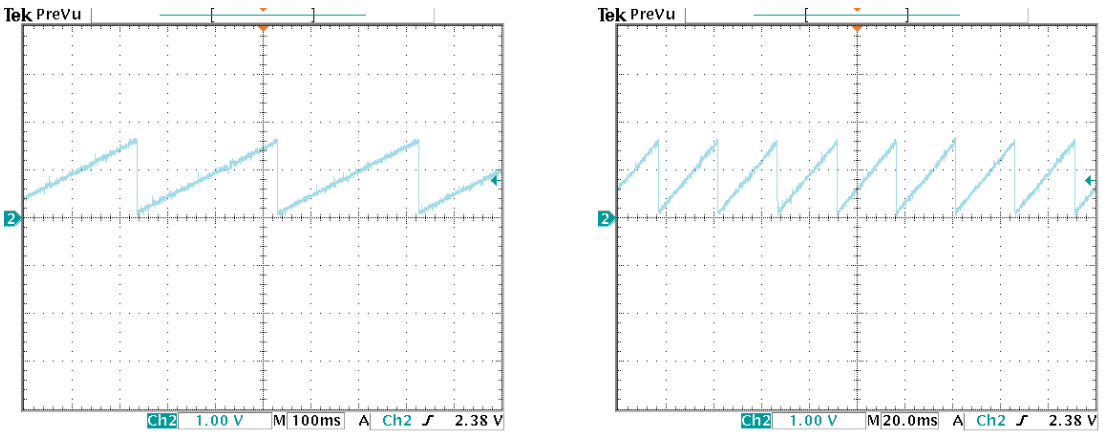

(a) Mechanical position (b) Electrical position

Figure 7.2: Mechanical and electrical position measurement.

7.2.2 PWM switching signals

The first test of the converter is to measure the PWM output signals of phase A, B and C of the inverter. This is to verify that the switching signals, which are generated by the DSP, are generated on the output of the inverter. This will confirm that the interface between the DSP and the inverter controller functions correctly. The PWM output signals of the inverter module along with the PWM duty cycles for each phase are shown in Fig. 7.3. The PWM duty cycles are in agreement with the expected duty cycle waveforms that the space vector modulation scheme is generating. The deformation on the peaks of the duty cycle waveforms are caused by the 3^{rd} harmonic injection of the space vector modulation scheme. This 3^{rd} harmonic injection allows for a 15% increase in the magnitude of the phase voltages as well as a reduction in switching losses. Note that the duty cycle waveforms are measured one at a time and, therefore, they appear to looks the same. This is due to the trigger setting of the oscilloscope.

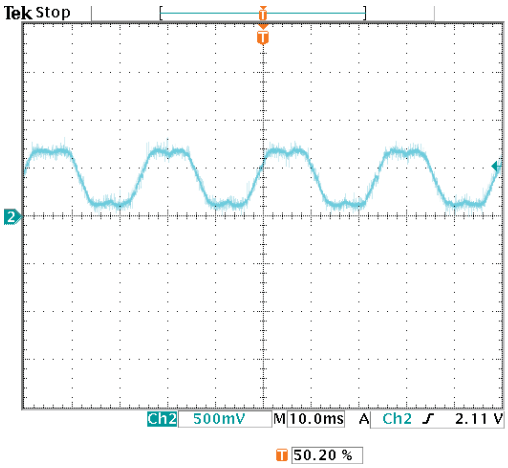

(a) PWM duty cycle for phase A

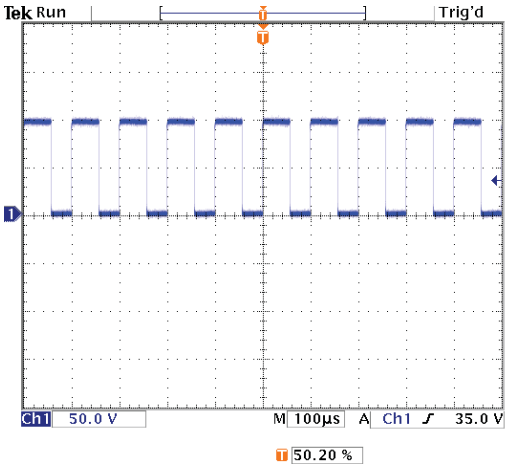

(b) PWM signal for phase A

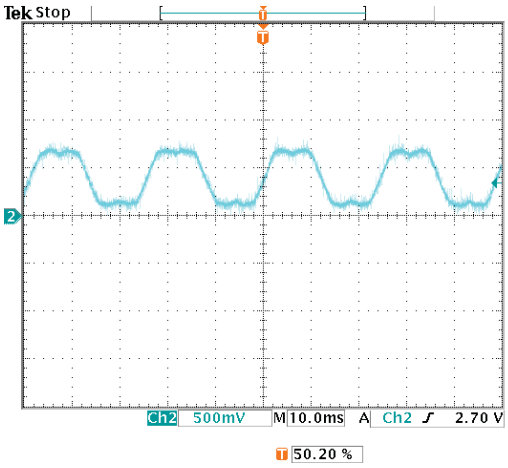

(c) PWM duty cycle for phase B

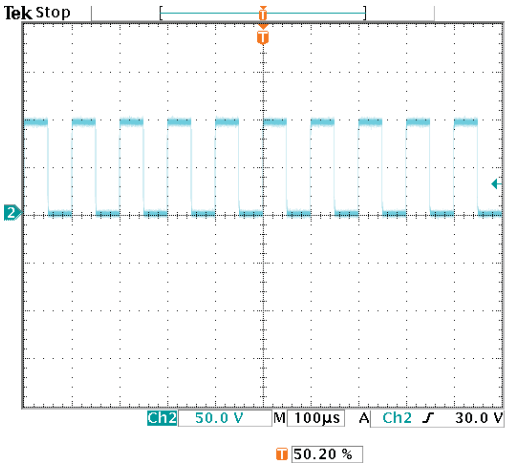

(d) PWM signal for phase B

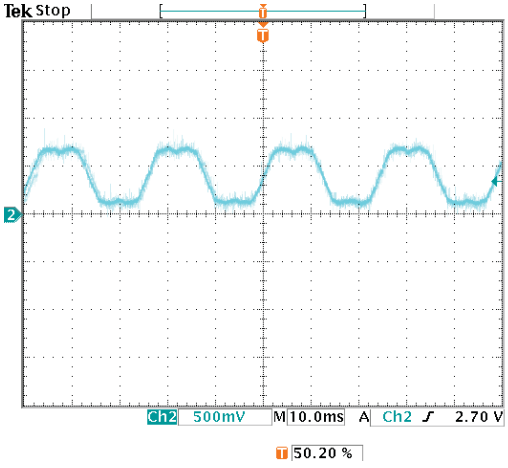

(e) PWM duty cycle for phase C

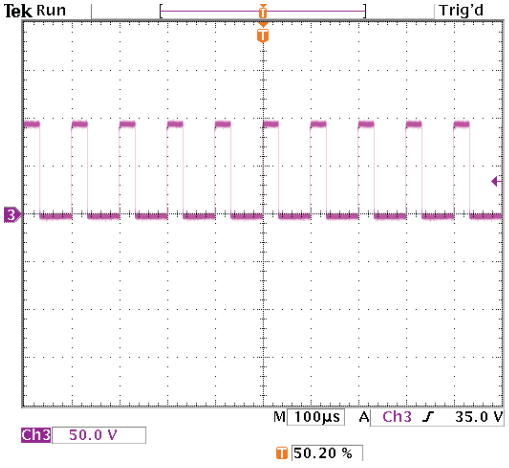

(f) PWM signal for phase C

Figure 7.3: PWM duty cylces and PWM output signals of the inverter for phase A, B and C.

7.2.3 PMSM tests

To test and verify that the converter is working, a no-load test is performed on a permanent magnet synchronous machine which is shown in Fig. 7.4. The DC bus voltage is set to 340 V and a q-axis current reference of 20 A is given. The measured three-phase currents of the machine is shown in Fig. 7.4. It can be observed from the measurement result that the inverter is capable of generating a three-phase sinusoidal output. This confirms that the power electronic converter is working and further test can, therefore, be conducted.

(a) PM synchronous motor

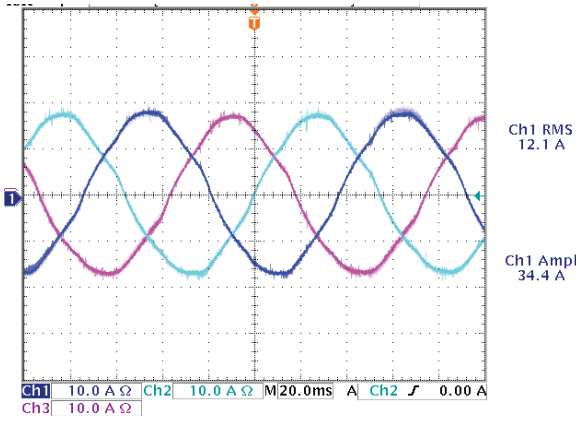

(b) Current controlled three-phase load current for the PMSM

Figure 7.4: Inverter test on a PM synchronous machine

7.2.4 Current controller test

In this test the current controller of the RFAPM drive is tested on an RL-load. The practical setup of the RL-load is shown in Fig. 7.5. The load has a resistance and inductance value of 25 Ω and 5.8 mH, respectively and both the resistors and inductors have a maximum current rating of 6 A. The exact same current controller as the one that is designed in Chapter 6 for the RFAPM drive is used, except that the controller gain is calculated for the inductance and resistance values of the RL-load.

The test is performed at a DC bus voltage of 340 V with the q-axis current reference set to 5 A and the d-axis current reference set to zero. The resolver is turned at a constant speed to feed the vector control algorithm with a position and speed measurement. The step response of the system is measured as 15.2 ms which is in close agreement with the simulated response time of 12 ms. The simulated and the measured step response of the RL-load system is shown in Fig. 7.6. The measured step response, however, shows a small overshoot before the system settles. This overshoot is small enough to be neglected for practical considerations. The measured three-phase load current of the RL-load is shown in Fig. 7.7, and it is clear from this result that the current controller is capable of controlling the

load current according to the current reference input.

Figure 7.5: RL-Load setup

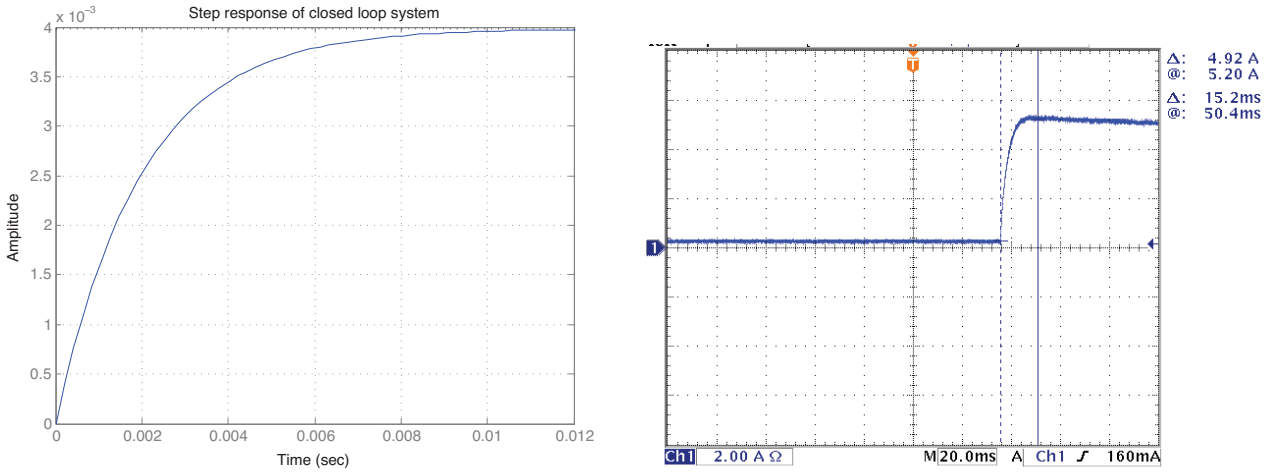

(a) Simulation (b) Measured

Figure 7.6: Step response of the current controller with an RL-load

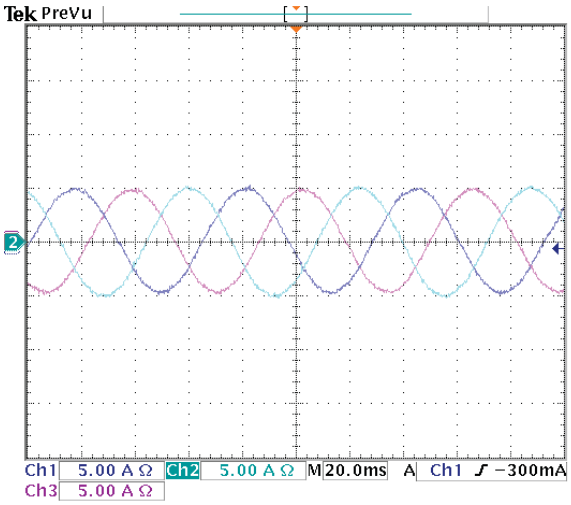

Figure 7.7: RL-load current measurement of the current controller.

7.3 RFAPM drive tests

In this section, various generator and motor tests are performed on the RFAPM drive motor in order to verify the analytical and FE results experimentally.

7.3.1 Induced phase voltage

In order to measure the induced phase voltages of the RFAPM drive an open-circuit test is performed. The DC motor is used to drive the RFAPM machine as a generator and the open-circuit phase voltages are measured. This test is not performed at the rated speed of the RFAPM machine since the DC machine is not able to operate at this speed. Therefore, the DC machine is run at 2000 rpm. The induced phase voltage at this speed is measured as 50 V_{RMS} (70.71 V_{peak}) and this is in good agreement with the FE analysis' result of 51.40 V_{RMS} (72.70 V_{peak}). The measured and FE results of the induced phase voltage is shown in Fig. 7.8. The waveforms show to be very sinusoidal with a very low THD.

7.3.2 Airflow rate measurement of the cooling fan

The airflow measurement of the cooling fan was performed by the specialist who designed the cooling fan. The author has very little information about the measurement procedures and methods, and no documentation in this regard are available. However, the results of the theoretical calculation of the flow rate is confirmed by the measurements. Fig. 7.9 shows a data plot of the calculated and measured airflow rate of the cooling fan, where the straight line shows the calculated flow rate and the diamond markers the measured flow rate.

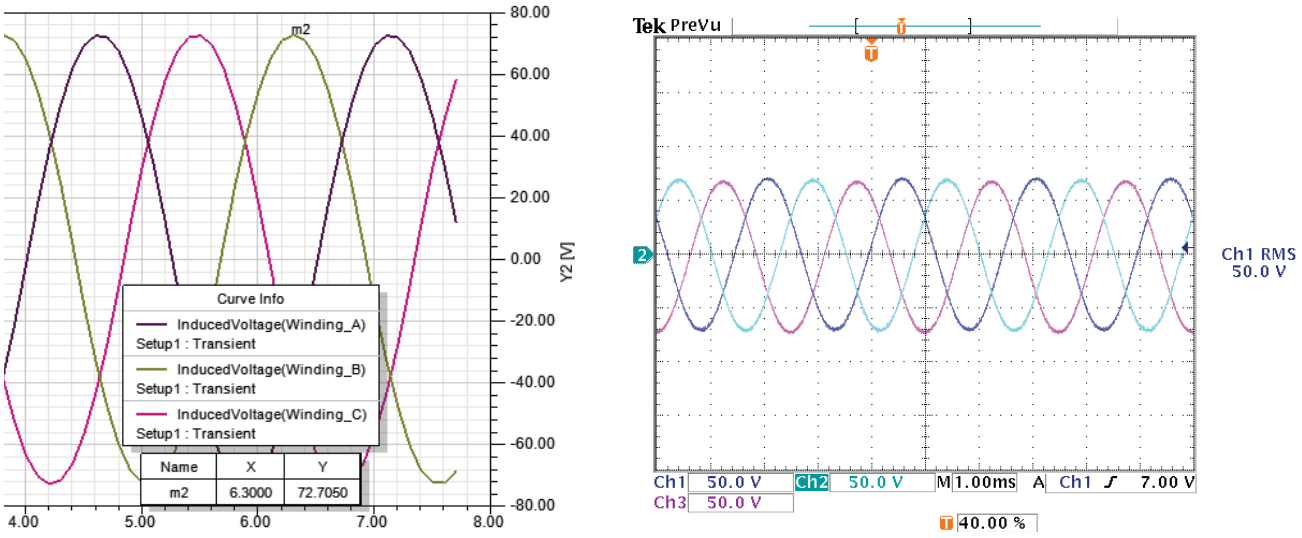

(a) Simulated induced phase voltage from FEA.

(b) Measured induced phase voltage.

Figure 7.8: Induced phase voltage of the RFAPM drive motor.

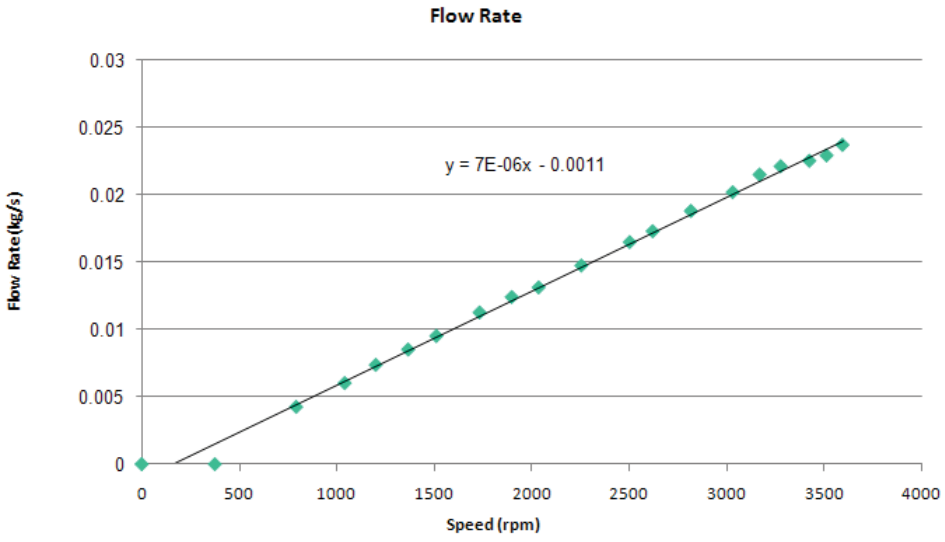

Figure 7.9: Data plot of the calculated and measured airflow rate of the cooling fan.

7.3.3 Eddy current losses

The eddy current losses are measured by driving the RFAPM motor at various incremental speeds with the terminals open-circuited. The measurement is performed as follows:

1. The RFAPM motor is run at various speeds from standstill up to 3000 rpm, and the torque is measured at the various speeds.

2. The total losses inside the machine (i.e eddy current losses, wind and friction losses

and mechanical losses) are then calculated as $P_T = \omega T$.

3. The stator of the RFAPM motor is then replaced with a nylon dummy stator, shown in Fig. 7.10.

4. Step 1) above is repeated, and the mechanical losses of the machine are calculated as $P_m = \omega T$.

5. The measured eddy current losses are then $P_{eddy} = P_T - P_m$.

The measured and calculated eddy current losses are shown in Fig. 7.11. It is clear from the measurement that the calculated eddy current losses are not in agreement with the measured losses since the measured losses are almost 50% higher. This imposes a problem for the cooling of the RFAPM drive as the cooling fan cannot produce a sufficient airflow rate to cool the machine.

Figure 7.10: Dummy stator for eddy current measurements.

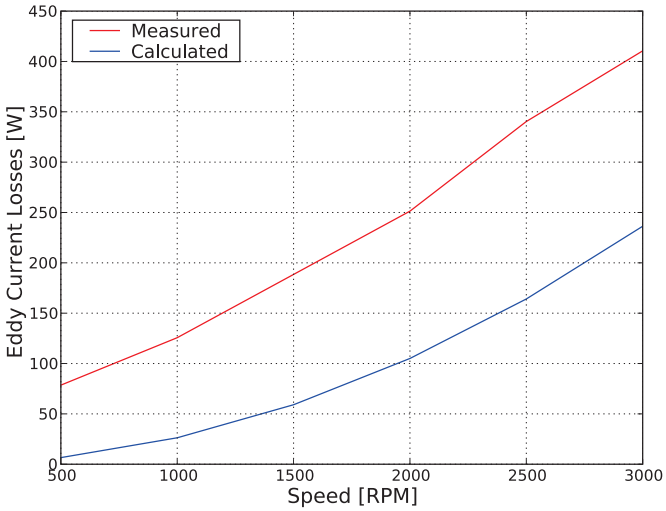

Figure 7.11: Measured and calculated eddy current losses.

7.3.4 Generator load test

A generator load test is performed on the RFAPM motor to verify that the RFAPM motor produces a three-phase sinusoidal current output. The setup of the experiment is shown in Fig. 7.12. The RFAPM drive is connected to a three-phase 90 Ω resistor bank and the DC machine is used to drive the RFAPM drive at a constant speed of 500 rpm. The load current measurements are shown in Fig. 7.13. It is shown that the RFAPM motor has a high quality three-phase sinusoidal output current, as also expected from the sinusoidal measured induced voltages of Fig. 7.8.

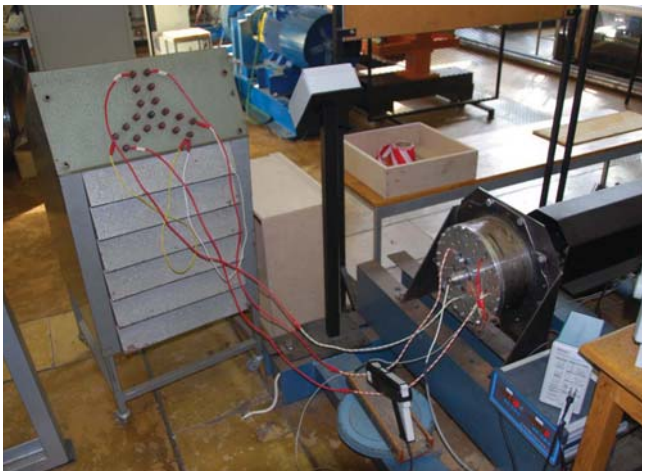

Figure 7.12: Generator load setup.

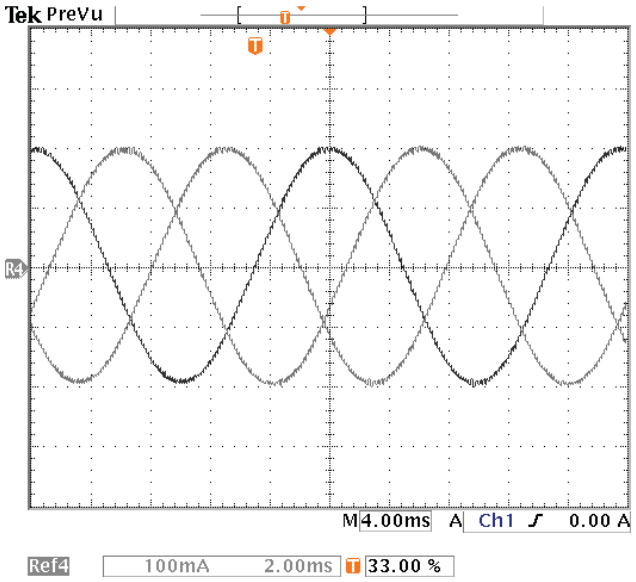

Figure 7.13: Measured current waveforms of the resistive load test.

7.4 Current controller tests of the RFAPM drive

7.4.1 Zero position alignment

The control algorithm of the RFAPM machine is performed in the dq reference frame, which is a reference frame that rotates synchronously with the rotor as explained in Appendix C. The transformation from the ABC reference frame to the dq reference frame requires that the instantaneous rotor position needs to be know. The rotor position is defined as the angle measured from the A-axis to the q-axis. The zero position is where the q-axis is aligned with and in the same direction as the A-axis, as illustrated by the phasor diagram in Fig. 7.14.

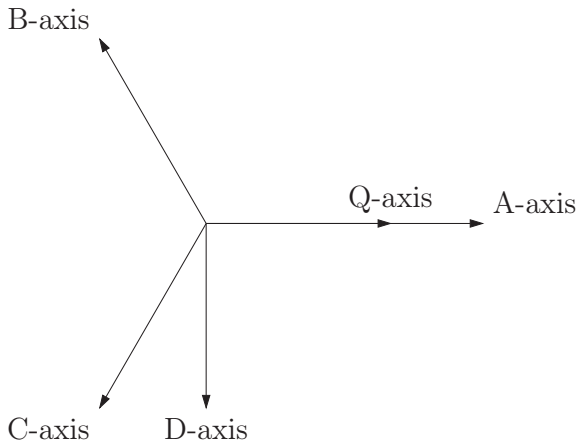

Figure 7.14: Definition of zero position ($\theta_r = 0$).

To obtain the zero position, the DC machine is used to drive the resolver which is mounted on the RFAPM drive motor at a constant speed. The induced voltage in phase A together with the resolver angle are measured. The resolver angle should be "in phase" with the induced phase voltage when correctly aligned. Fig. 7.15(a) shows the resolver angle being out of phase with the induced voltage in phase A and Fig. 7.15(b) shows the resolver angle in phase with the induced phase voltage with the zero offset position set to 74.5°.

7.4.2 Drive motor tests

The RFAPM drive is next operated as a motor and the dynamometer on the test bench acts as a load to the machine. The current controller which is designed in Chapter 6 is implemented to control the d and q-axis current of the RFAPM drive and a DC bus voltage of 340 V is used. The load current waveform of the RFAPM drive is shown in Fig. 7.16. It can be seen from the measurement shown in Fig. 7.16 that the load currents of the RFAPM are not controlled. Through extensive testing and changes made to the current controller, the currents could still not be controlled to be sinusoidal. An external inductance, with a phase value of 30 mH, is added in series with each phase of the drive motor and the same results are obtained. The rated speed and torque of the RFAPM drive, therefore, could not be achieved and due to time constraints on the project, further testing could not be

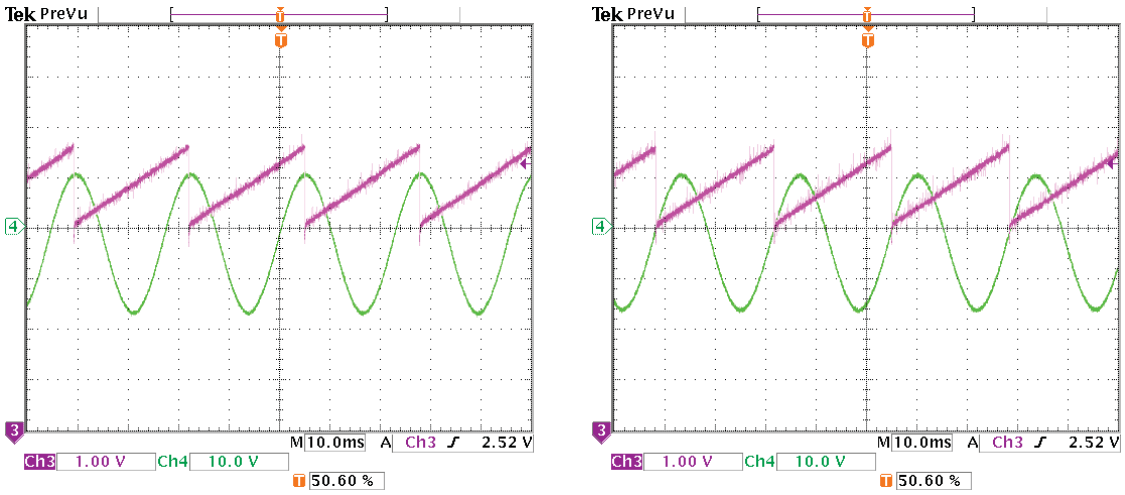

(a) Zero-Position = 0°, not aligned. (b) Zero-Position = 74.5°, aligned.

Figure 7.15: Alignment of the electrical rotor position.

conducted. To determine whether the integrity of the power converter is under question, an exiting converter was used and the same problem occurred.

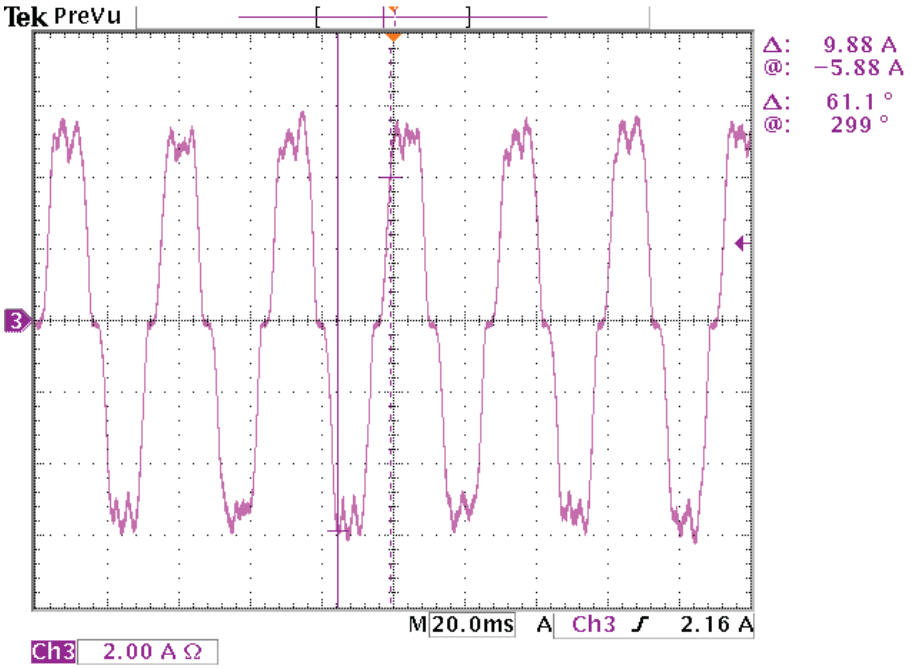

Figure 7.16: Load currents of the RFAPM drive motor.

Chapter 8

Conclusions and Recommendations

This thesis aimed to investigate the use of a manual transmission drivetrain with a radial flux air-cored permanent magnet machine, without flux-weakening, as traction drive for electric vehicle applications. An Opel Corsa Lite is converted to a battery electric vehicle for the purpose of this investigation. This chapter gives a brief discussion on the conclusions that are derived for this study and recommendations are given for possible future work.

8.1 Conclusions

In this section conclusions on the Li-ion battery pack, the RFAPM drive motor, the power electronic converter and the digital current controllers are discussed.

Li-ion battery pack

From the review, design and practical use of the Li-ion battery pack, the following conclusions are derived.

- Li-ion battery technology are the most preferred battery technology for electric vehicle application.
- The most profound drawback of Li-ion batteries are their high sensitivity towards overcharging and over-discharging.
- A battery management system is an essential requirement for Li-ion batteries to ensure a prolonged life of the batteries and to protect the batteries from being damaged.
- The size of the Li-ion battery pack is determined by the desired range and power requirements for the E-Corsa. However, it is found from the calculations in Chapter 3 that the range requirement is the dominating factor which determines the size of the battery pack.

RFAPM motor drive

An analytical method is derived whereby the RFAPM drive motor is designed. The desired performance specifications for the drive motor are obtained from the analytical design and these results are shown to be in good agreement with the results obtained through a FE analysis of the machine. The results obtained through practical measurements performed on the drive motor, are summarised as follows:

- Measurement of the induced phases voltages of the motor are in agreement with the analytical and FEA results. Furthermore, it is shown that the induced phase voltages are very sinusoidal with very low THD.
- From a generator load test performed on the RFAPM motor, it is shown that the motor has a high quality three-phase sinusoidal output current
- The measured phase resistance and inductance of the machine are in close correlation with the calculated values.
- The centrifugal cooling fan achieves the designed airflow rate requirement.
- Measurement of the eddy current losses contradicts the calculated losses, since it is found to be almost 50 % higher than calculated. The RFAPM drive could, therefore, not be cooled effectively by the cooling fan.

Power electronic converter

The power electronic converter for the RFAPM motor is designed and implemented in Chapter 5. Practical tests and measurements confirmed the functionality of the converter.

dq Current controller

In Chapter 6, the dq current controllers for the RFAPM drive motor are designed and a practical implementation of the controllers are performed in Chapter 7. Findings on the practical tests and measurements of the current controllers are summarised as follows:

- The current controller is tested on a RL-load, and from the test results it is shown that the step response of the system is in close agreement with the simulated step response of the system. It is also shown that the current controller is capable of controlling the load current according to a current reference input.
- The test results on the RL-load confirm that, the design methodology of a stable proportional current controller design in the W-plane is valid.
- With the implementation of the current controller on the RFAPM machine, it is found that the controller is not capable of controlling the load currents. Due to the low phase impedance characteristics of the RFAPM machine, external phase inductance are added and the controller is still not capable of controlling the load currents.

- Due to time constraint on the project the current controller problem could not be resolved.

8.2 Recommendations

From the conclusions of the study, the following recommendations are made for possible future work.

- The battery pack of the E-Corsa, could be replaced with the latest and a much lighter type of Li-ion technology in order to, reduce the total weight of the battery pack and increase the range and power capabilities of the vehicle.
- The BMS that is currently used for the battery pack of the E-Corsa could be replaced by a more advanced and reliable management system that is readily available. It could also be considered to develop an advanced modular system in-house. A new BMS should be used if the existing battery pack of the E-Corsa is replaced with a new type of Li-ion battery technology.
- The eddy current losses of the RFAPM motor require further investigation in order to determine the difference between the calculated losses and the measured losses.
- To investigate the current controller problem, an LC-filter could be placed at the output of the inverter to first filter out the PWM carrier signal before it is applied to the machine. Also, a trapezoidal control scheme, as opposed to a space vector control scheme, could be implemented.
- It could be considered to replace the RFAPM drive with a PM iron-cored machine or a reluctance synchronous machine (RSM). RSMs have a rugged construction, fault-tolerant operation, simple control, and outstanding torque-speed characteristics.

Appendices

Appendix A

Analytical analysis of the RFAPM machine

A.1 Concentrated-coil stator winding design

A two-dimensional cross-sectional view of the nominal stator radius with the concentrated-coils spaced so that the adjacent coil sides touch, is depicted in Fig. A.1. This concentrated-coil configuration results in a maximised flux-linkage due to the coil widths being closer to π electrical degrees. From Fig. A.1, r_n represents the nominal radius of the stator, θ_r the radial angle of the coil width in electrical degrees, θ_m the active coil angle in electrical degrees, Δ is $\frac{1}{2}$ of the coil side-width angle of the stator coils, W the coil width and h the coil thickness.

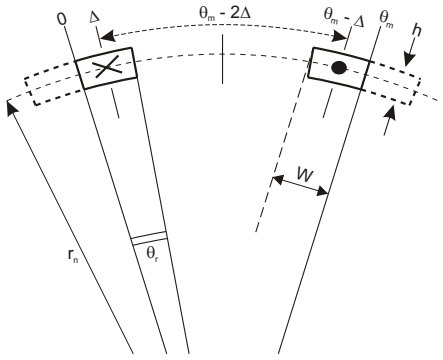

Figure A.1: A 2D cross-sectional view of the concentrated-coil stator windings placed around the nominal radius of the stator, in a radial plane.

For the analysis it is assumed that the stator thickness is much less than the nominal radius of the stator so that h $\ll r_n$, allowing us to consider all the turns as situated around the nominal stator radius. To start the analysis, the flux-linkage of a single turn, with current flowing in at one end of the turn and out at the other end, is considered. Fig. A.2 shows a

single turn situated along the nominal radius of the stator, with a radial sinusoidal airgap flux density.

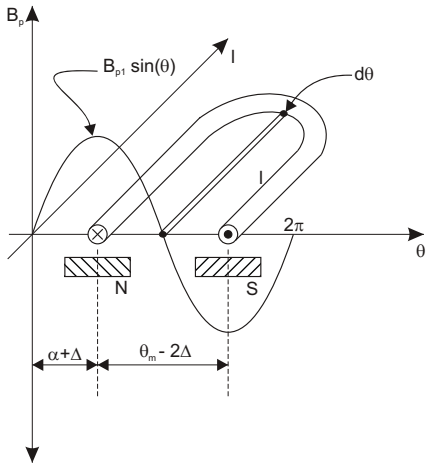

Figure A.2: A 3D cross-sectional view of the stator of a RFAPM machine with non-overlapping stator coils and sinusoidal radial flux distribution.

Flux linkage

The flux-linkage for this single turn at a position Δ inside the coil, can be calculated as

$$\begin{aligned} \lambda_1 &= \frac{2}{p} \cdot B_{p1} \cdot r_n \cdot \ell \cdot \int_{\alpha+\Delta}^{\alpha+\theta_m-\Delta} \sin\theta \, d\theta \\ &= \frac{4}{p} \cdot B_{p1} \cdot r_n \cdot \ell \cdot \sin\left(\frac{\theta_m}{2} - \Delta\right) \cdot \sin\left(\alpha + \frac{\theta_m}{2}\right) \end{aligned} \tag{A.1.1}$$

where p is the number of poles, ℓ is the active coil length, $\alpha = \omega t$ and B_p is the peak flux density.

The next step is to calculate the total flux-linkage of a coil with N number of turns. Before this can be done, the following needs to be considered:

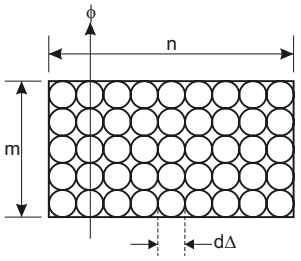

Figure A.3: A 2D cross-sectional view of a coil with m × n conductors with the direction of the magnetic flux being through the conductors.

Illustrated in Fig. A.3 is a cross-sectional view of a coil consisting of N number of turns. As can be seen from this illustration, the total number of turns, N, is made up of m and n conductors, such that N = m × n. The magnetic flux of a magnet passing the coil will travel radially across the conductors in the m direction. It is therefore obvious that the induced voltage of the conductors in the m direction will be the same. However, because the magnetic flux does not travel through the n conductors in the same direction as through the m conductors, the induced voltages in the m and n conductors will not be the same. Thus, to calculate the total flux-linkage of a coil containing N conductors, a correction factor, k_{pc}, needs to be introduced into the calculation. The correction factor involves converting the sum of the flux-linkages in the n conductors into a Riemann sum. The correction factor can be expressed by

$$\begin{aligned}
k_{pc} &= \frac{\sum_{i=1}^{n} \sin\left(\frac{\theta_m}{2} - \Delta_i\right) \cdot d\Delta}{n d\Delta} \\
&\simeq \frac{\int_0^{\theta_r} \sin\left(\frac{\theta_m}{2} - \Delta\right) d\Delta}{\theta_r} \\
&= \frac{1}{\theta_r} \cos\left(\frac{\theta_m}{2} - \Delta\right) \\
&= \frac{1}{\theta_r}\left[\cos\left(\frac{\theta_m}{2}\right) - \cos\left(\frac{\theta_m}{2}\right)\right] \\
&= \frac{1}{\theta_r}\left[-2\sin\left(\frac{\theta_m - \theta_r}{2}\right) \cdot \sin\left(\frac{-\theta_r}{2}\right)\right] \\
&= \frac{2\sin\left(\frac{\theta_m}{2} - \frac{\theta_r}{2}\right)}{\theta_r} \\
&= \frac{2\sin\left(\frac{\theta_m}{2}(1 - k_c)\right) \cdot \sin\left(\frac{\theta_m k_c}{2}\right)}{k_c \theta_m}
\end{aligned} \tag{A.1.2}$$

The flux-linkage in a coil with a total number of N turns, can therefore be calculated as

$$\begin{aligned}
\lambda_N &= \frac{4}{p} \cdot B_{p1} \cdot r_n \cdot \ell \cdot (m \times n) \cdot \sin\left(\frac{\theta_m}{2}\right) \cdot \left[\frac{\sum_{i=1}^{n} \sin\left(\frac{\theta_m}{2} - \Delta_i\right)}{n \sin\left(\frac{\theta_m}{2}\right)}\right] \cdot \sin\left(\omega t + \frac{\theta_m}{2}\right) \\
&= \frac{4}{p} \cdot B_{p1} \cdot r_n \cdot \ell \cdot N \cdot \sin\left(\frac{\theta_m}{2}\right) \cdot k_{pc} \cdot \sin\left(\omega t + \frac{\theta_m}{2}\right)
\end{aligned} \tag{A.1.3}$$

From (A.1.2), $k_c = \frac{\theta_r}{\theta_m}$ is the optimisation factor for θ_r. θ_r is the variable that must be optimised so that $\theta_r = k_c \cdot \theta_m$, with $0 < k_c < \frac{1}{2}$. $\theta_m = \frac{\pi p}{Q}$ is the active coil angle (in electrical degrees).

Induced phase voltage

By applying Faraday's law, the induced coil voltage can be calculated by differentiating the flux-linkage given by (A.1.3). The induced coil voltage is therefore given as

$$\begin{aligned} e_{coil} &= \frac{d}{dt}\lambda_N \\ &= \frac{4}{p} \cdot B_{p1} \cdot r_n \cdot \ell \cdot N \cdot k_{pc} \cdot \omega_e \cdot \cos\left(\omega t + \frac{\theta_m}{2}\right) \\ &= 2 \cdot B_{p1} \cdot r_n \cdot \ell \cdot N \cdot k_{pc} \cdot \omega_m \cdot \cos\left(\omega t + \frac{\theta_m}{2}\right) \end{aligned} \tag{A.1.4}$$

and peak sinusoidal phase voltage, E_p can be expressed as

$$\begin{aligned} E_p &= \frac{q}{a} \cdot \frac{4}{p} \cdot \omega_e \cdot B_{p1} \cdot N \cdot r_n \cdot \ell \cdot k_{pc} \cdot k_d \\ &= 2 \cdot \frac{q}{a} \cdot \omega_m \cdot B_{p1} \cdot N \cdot r_n \cdot \ell \cdot k_{pc} \cdot k_d \end{aligned} \tag{A.1.5}$$

where ω_e is the electrical rotational speed in $\frac{rad}{s}$, ω_m is the mechanical rotational speed. k_d is a distribution factor that takes into account the effect of the induced phase voltage when more than one coil is placed side by side in a phase group, (n $>$ 1). q is the number of coils per phase and a the number of parallel coils per phase. The distribution factor is derived from classical theory as

$$k_d = \frac{\sin\left(0.5n\left[\theta_m - \pi\right]\right)}{n\sin\left(0.5\left[\theta_m - \pi\right]\right)} \tag{A.1.6}$$

It is known that, for radial flux machines, with n = 1 and $\theta_m = \frac{4\pi}{3}$, thus $k_d = 1$, yields the best machine design results. Note that n, from (A.1.6), represents the number of coil groups.

Phase resistance

The torque of an electrical machine can be expressed by

$$T_m = \frac{P_m}{\omega_m} \tag{A.1.7}$$

Ignoring the wind and friction losses in the machine, the mechanical power input will be equal to the electrical power output [3]. The mechanical power of the machine can therefore be expressed as

$$P_m = P_e = \frac{3}{2} E_p I_p \tag{A.1.8}$$

Considering the air-cored permanent magnet machine operating in generator mode, the power that the generator will deliver to an electrical load, P_s, can be calculated as

$$P_s = P_e - P_{cu} \tag{A.1.9}$$

where P_{cu} is the copper losses of the machine, which can be expressed in terms of the peak phase current and phase resistance as

$$P_{cu} = 3\frac{I_p^2}{2}R_{ph} \tag{A.1.10}$$

Furthermore, the resistance of a copper wire is given by

$$R_{cu} = \frac{\rho_{cu}\,(2\ell + \ell_{ec})}{A_{cu}} \tag{A.1.11}$$

For non-overlapping coils the end-turn length, ℓ_{ec}, of a coil can be derived as follows:

$$\begin{aligned}
\ell_{ec} &= 2\left[r_n\frac{2}{p}\theta_m - 2W + 2\sqrt{2\left(\frac{W}{2}\right)^2}\right] \\
&= \frac{4r_n\theta_m}{p} - W\left(4 - \sqrt{8}\right) \\
&= \frac{4r_n\theta_m}{p} - \frac{2r_n\theta_r}{p}(1.1716) \\
&= \frac{4r_n}{p}\left(\theta_m - 0.586\theta_r\right) \\
&= \frac{4r_n\theta_m}{p}\left(1 - 0.586k_c\right)
\end{aligned} \tag{A.1.12}$$

and the area of the copper wire can be approximated [3] by

$$A_{cu} = \frac{(h \times W)k_f}{N} \tag{A.1.13}$$

By substituting (A.1.13) into (A.1.11) the total resistance of a coil with N number of turns can be calculated as

$$R_{cu} = \frac{N^2\rho_{cu}\,(2\ell + \ell_{ec})}{k_f hW} \tag{A.1.14}$$

The phase resistance, with q number of coils per phase and a number of parallel circuits, can be calculated [3] as

$$R_{ph} = \frac{N^2 \cdot \mathrm{q} \cdot \rho_t \cdot (2\ell + \ell_{ec})}{a^2 \cdot k_f \cdot \mathrm{h} \cdot \mathrm{W}} \tag{A.1.15}$$

Eddy current losses

The eddy current losses in the RFAPM machine can be calculated from [8] as follows:

$$P_{eddy} = 2.159\left[\frac{N\ell B_p^2 f^2 Q N_p N_{p_{diam}}^4}{\rho_t}\right] \tag{A.1.16}$$

where N is the number of turns per coil, N_p is the number of parallel strands per conductor, $N_{P_{diam}}$ is the diameter of a single parallel strand, Q is the total number of stator coils, B_p is the peak flux density, f is the motor frequency, ℓ is the active length of the winding and ρ_t is the resistivity of copper.

Stator inductance

The inductance of non-overlapping windings, L_c, is given by [8] as

$$L_c = \frac{q\left(2\ell + \ell_{ec}\right)^2 N^2}{h} 10^{-7} K_n \tag{A.1.17}$$

During operation the coil is magnetised, which results in the magnetic field no longer being uniform in the winding and therefore a correction factor, referred to as the Nagaoka constant, K_n, is required [8]. K_n is given by [8] as

$$K_n = \frac{1}{1 + 0.9\frac{2\ell+\ell_{ec}}{2\pi h} + 0.32\frac{2\pi W}{2\ell+\ell_{ec}} + 0.84\frac{W}{h}} \tag{A.1.18}$$

Peak phase current

From (A.1.10) and (A.1.15), the peak phase current is given as

$$I_p = \sqrt{\frac{2P_{cu}}{3R_{ph}}} \tag{A.1.19}$$

The symbols in (A.1.15) are defined as follows:

q = number of stator coils per phase = $\frac{Q}{3}$

ρ_t = resistivity of copper at a temperature t [Ω m]

ℓ = axial length and active length of the stator coil or winding

ℓ_{ec} = total end-turn length of the stator coil

k_f = fill factor for the stator conductors

W = coil width as depicted in Fig. A.1

The coil width, W, can be expressed with good accuracy as

$$\mathrm{W} = \frac{2 \cdot r_n \cdot \theta_r}{\mathrm{p}} \tag{A.1.20}$$

Developed torque

By substituting eqns (A.1.5, A.1.19, A.1.15) and (A.1.20) into eqn (A.1.7) the developed torque in terms of machine parameters results in

$$T_d = k_w \cdot k_e \cdot C_1 \tag{A.1.21}$$

Remembering from the derivation of the pitch factor, k_{pc}, that θ_r should be optimised so that $\theta_r = k_c \cdot \theta_m$, with $0 < k_c < \frac{1}{2}$, the variables of the developed torque in eqn (A.1.21) are defined as follows:

$$k_w = k_{pc} \cdot k_d \cdot \sqrt{\frac{\mathrm{q} \cdot \theta_r}{\mathrm{p}}} \qquad \text{with} \quad \theta_r < \frac{\theta_m}{2} \tag{A.1.22}$$

$$k_e = (2 + \delta_c)^{-\frac{1}{2}} \qquad \text{with} \quad \delta_c = \frac{\ell_{ec}}{\ell} \tag{A.1.23}$$

$$C_1 = B_p \cdot \sqrt{\frac{12 \cdot \rho_{cu} \cdot k_f \cdot \mathrm{h} \cdot r_n^3 \cdot \ell}{\rho_t}} \tag{A.1.24}$$

where k_w is the winding factor and δ_c is the end-turn to active copper length ratio, which should be optimised so that the end winding factor $k_e < 0.707$. C_1 is the machine constant.

Copper mass

The total copper mass of the stator windings can be calculated as follows

$$M_{cu} = k_m \cdot (2 + \delta_c) \cdot C_2 \tag{A.1.25}$$

where,

$$\begin{aligned} C_2 &= \mathrm{h} \cdot r_n \cdot k_f \cdot \ell \cdot \Upsilon_{cu} && , \Upsilon_{cu} \text{ is the density of copper} \\ k_m &= \frac{k_c \cdot \theta_m \cdot \mathrm{Q}}{p} && , \theta_m = \frac{\pi p}{Q} \\ &= \pi \cdot k_c \end{aligned}$$

A.2 Dual-Rotor Design

Fig. A.4 is a cross-sectional view of the dual-rotor structure, with the air-cored stator situated between the two rotor disks. The symbols in Fig. A.4 are defined as follows

h_m = magnet height

h_y = yoke height

ℓ_{ipg} = inter polar gap lenght

ℓ_g = gap length

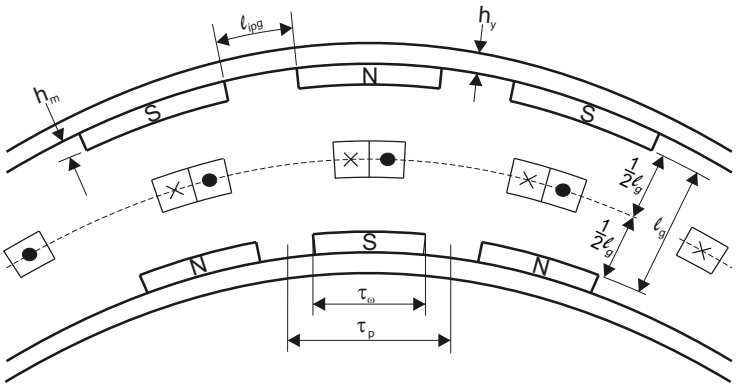

Figure A.4: 2D view of the dual-rotor with surface mounted permanent magnets.

τ_w = pole width

τ_p = shoe pole width

The design of the the dual-rotor structure is considerably more complicated than that of conventional surface mounted PM machines, due to its relatively large airgap. This relatively large airgap results in a greater of leakage of flux. Flux leakage can occur between adjacent magnets, as shown in Fig. A.5, which can cause drastic deterioration of the machine's perfomance. Flux can also leak from the pole edges directly back into the iron yoke, as shown in Fig. A.6. The rotor design is therefore subject to constraints which will be explained next.

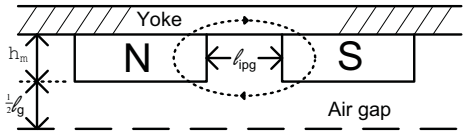

Figure A.5: Flux leakage between adjacent magnets.

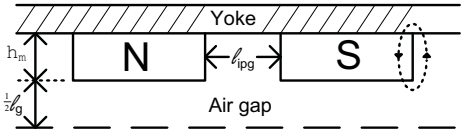

Figure A.6: Flux leakage from pole edges into the iron yoke.

Leakage of flux from the pole edges back into the rotor yoke occurs when the magnet height, or thickness, is less than half of the total gap length. To avoid this happening, the rotor design will need to adhere to the following constraint

$$h_m > \frac{1}{2}\ell_g \tag{A.2.1}$$

The flux path of flux leakage occurring between adjacent magnets is shown in Fig. A.5. In order to limit this flux leakage from occurring, it is required that the inter polar gap length, ℓ_{ipg}, should be greater than half of the total airgap length. This constraint is given by (A.2.2). Due to the curvature of the dual-rotor, the flux leakage will be more severe between the magnets on the inner rotor. The constraint in (A.2.2) should therefore be applied to ℓ_{ipg} of the inner rotor's permanent magnets.

$$\ell_{ipg} > \frac{1}{2}\ell_g \tag{A.2.2}$$

A.3 Magnet height and airgap flux density

The magnet height for a required airgap flux density can be calculated from [13] as follows:

$$h_m = \frac{B_g \ell_g}{2\mu_0 H_c \left[1 - \frac{B_g}{B_r}\right]} \tag{A.3.1}$$

where B_g is the required airgap flux density, ℓ_g is the airgap length, μ_0 is the permeability of free space, H_c is coercive magnet field strength and B_r is the residual magnetic flux density. From this equation the required NdFeB magnet length for a required airgap flux density can be calculated using the specifications of the desired NdFeB magnet.

Appendix B

Analysis of Inverter Losses

The formulation of the inverter losses will be derived from a half bridge inverter topology, shown in Fig. B.1. The assumption will be made that carrier based sinusoidal pulse width modulation (SPWM) is used to control the inverter. It is further assumed that the load current is purely sinusoidal, thus ignoring the ripple current.

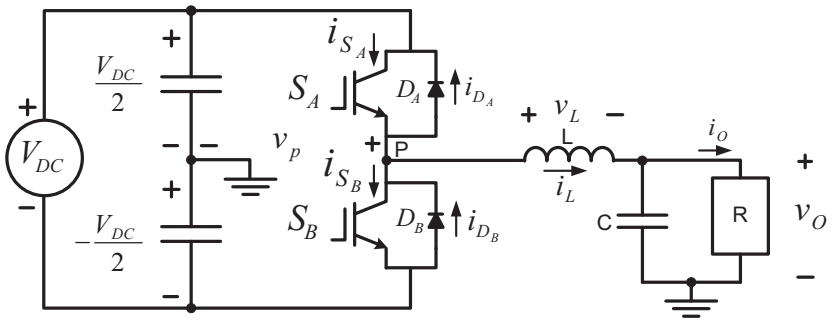

Figure B.1: Half bridge inverter topology.

From Fig. B.1, the bus voltage is defined as V_{DC}, the load current as i_o and the peak load current as I_o. The load inductance and capacitance are defined as L and C, respectively. The carrier wave is defined as $c\,(t)$ and the reference wave as $m\,(t) = m_a \sin\,(\omega_1 t)$, with m_a being the modulation index. The periods of $m\,(t)$ and $c\,(t)$ are defined as $T_1 = \frac{1}{f_1}$ and $T_s = \frac{1}{f_s}$, respectively.

B.1 Switching Losses

The switching losses occuring in the IGBTs can be approximated by calculating the energy that is dissipated in a switch-on and switch-off transition. The energy dissipated within a transition is given by (B.1.1) and (B.1.2)

$$W_{turn(On)} = \frac{1}{2} V_{DC} i_C t_{on} \tag{B.1.1}$$

$$W_{turn(Off)} = \frac{1}{2} V_{DC} i_C t_{off} \tag{B.1.2}$$

where i_C is the collector current of the IGBT, t_{on} is the switch-on rise time and t_{off} the switch-off fall time of the IGBT.

By defining the load inductor current as $i_L = I_o \sin(\omega_1 t - \phi)$, with ϕ the phase angle between the load voltage and current, an assumption is made that the turn-on and turn-off transitions occur at the same current amplitude in each switching cycle. Furthermore, the average switching losses are obtained by converting the sum of the switching energies over a period of T_1 into a Riemann sum. The average switching losses of the top IGBT, S_A, over a period T_1 are determined as

$$\begin{aligned} P_{sw} &= \frac{1}{T_1} \sum_{i=1}^{N} \frac{1}{2} V_{DC} I_o \sin(\omega_1 t_i - \phi)(t_{on} + t_{off}) \\ &= \frac{1}{2T_1 T_s} V_{DC} I_o (t_{on} + t_{off}) \sum_{i=1}^{N} \sin(\omega_1 t_i - \phi) T_s \\ &= \frac{1}{2T_1 T_s} V_{DC} I_o (t_{on} + t_{off}) \int_{\frac{\phi}{\omega_1}}^{\frac{T_1}{2} + \frac{\phi}{\omega_1}} \frac{1}{2T_1 T_s} V_{DC} I_o (t_{on} + t_{off})\, dt \\ &= \frac{f_s}{2\pi} V_{DC} I_o (t_{on} + t_{off}) \end{aligned} \tag{B.1.3}$$

Note from (B.1.3) that the switching losses are independant of the phase angle, ϕ.

B.2 Conduction Losses

A conducting IGBT is modelled by a resistance, r_{ce}, in series with a voltage source with a constant voltage, V_{on}. The conduction losses in S_A are therefore given by

$$P_{cond}(IGBT) = V_{on} \cdot I_{S_A} + I^2_{S_A(RMS)} \cdot r_{ce} \tag{B.2.1}$$

where, I_{S_A} and $I_{S_A(RMS)}$ are defined as the average and RMS current through S_A, respectively. A section of the positive half cycle current that flows through S_A is shown in Fig. B.2.

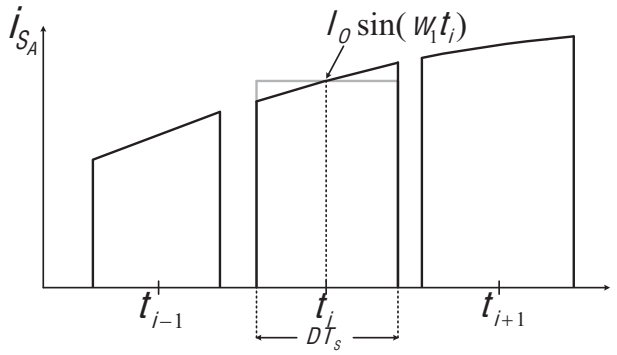

Figure B.2: Average current approximation.

From this figure the energy that is dissipated in the i^{th} pulse can be approximated by

$$\begin{aligned} E_{i(cond)} &\approx V_{on} \cdot DT_s \cdot I_o \sin(\omega_1 t_i) \\ &= V_{on} \frac{1}{2} \left(1 + m_a \sin(\omega_1 t_i)\right) I_o \sin(\omega_1 t_i) T_s \end{aligned} \tag{B.2.2}$$

with the duty cycle of S_A defined as, $D = \frac{1}{2}(1 + m_a \sin(\omega_1 t))$. Furthermore, the middle of the switching period is defined as t_i with the range of i defined as $1 \leq i \leq N$.

The first term in (B.2.1) is obtained by adding all of these pulses together and dividing the sum by T_1. The average current through S_A is then approximated by using a Riemann sum. The first term in (B.2.1) is thus given by

$$\begin{aligned} V_{on}.I_{S_A} &= \frac{1}{T_1} \sum_{i=1}^{N} E_{i(cond)} \\ &= \frac{1}{T_1} \sum_{i=1}^{N} \frac{1}{2} V_{on}(1 + m_a \sin(w_1 t_i)) I_o \sin(w_1 t_i) Ts \\ &\approx \frac{V_{on}}{2T_1} \int_0^{\frac{T_1}{2}} \left(1 + m_a \sin(\omega_1 t)\right) I_o \sin(\omega_1 t) dt \\ &= V_{on} \left(\frac{I_o}{2\pi} + \frac{m_a I_o}{8}\right) \end{aligned} \tag{B.2.3}$$

The RMS current, $I_{S_A(RMS)}$, through S_A is obtained similarly to (B.2.3) by first squaring all the pulses in Fig. B.2. The RMS current is then given by

$$\begin{aligned} I^2_{S_A(rms)} &= \frac{1}{T_1}\sum_{i=1}^{N} I_o^2 \sin^2(w_1 t_i).DT_s \\ &= \frac{I_o^2}{2T_1}\sum_{i=1}^{N} \sin^2(w_1 t_i)\Big(1 + m_a \sin(w_1 t_i)\Big).T_s \\ &\approx \frac{I_o^2}{2T_1}\int_0^{\frac{T_1}{2}} \Big[\sin^2(w_1 t) + m_a \sin^3(w_1 t)\Big]dt \\ &= I_o^2\left[\frac{1}{8} + \frac{m_a}{3\pi}\right] \end{aligned} \tag{B.2.4}$$

B.3 Diode losses

The diode losses can be determined by first calculating the average current flowing through the diode over one switching period, and then multiplying it by the forward diode voltage, $V_{f(diode)}$. The average current flowing through diode d_B is the difference between the average inductor current, I_L, and the average current through S_A. The average current flowing through the diode, over one period, is given by

$$\begin{aligned} I_{D_B} &= I_L - I_{S_A} \\ &= \frac{1}{T_1}\int_0^{\frac{T_1}{2}} I_o \sin(w_1 t)dt - I_{S_A} \\ &= \frac{I_o}{\pi} - \left(\frac{I_o}{2\pi} + \frac{m_a I_o}{8}\right) \end{aligned} \tag{B.3.1}$$

Finally, the conduction losses in the diode are given by

$$P_{diode} = I_{D_B} V_{f(diode)} \tag{B.3.2}$$

Appendix C

Space Vector Control of Synchronous Machines

C.1 Space vector theory

AC motor control structures generally apply three 120° spatially displaced sinusoidal voltages to the three stator phases. In most of the classic AC drives the generation of the three sine waves is based on the electromechanical characteristics of the motor and on an equivalent model for the motor in its steady state. Furthermore, the control looks like three separate single-phase system controls, rather than one control of a three-phase system. Some major common drawbacks [4] are:

- The machine models and characteristics used are valid only in steady state. This causes the control to allow high peak voltage and transients current. These damage not only the drive dynamic performance but also the power conversion efficiency. Additionally, the power components must be oversized in order to withstand the transient electrical spikes.
- Great difficulty is experienced in controlling the variables with sinusoidal references: PI regulators cannot perform a sinusoidal regulation without damaging the sinusoidal reference, and hysteresis controllers introduce high bandwidth noise into the system that is hard to filter out.
- There is no three-phase system imbalance management.
- Finally, the control structure must be dedicated according to motor type (asynchronous or synchronous).

The following sections present the Space Vector Control (SVC) of AC drives. This control solution overcomes each of these drawbacks and thus improves the overall effectiveness of the AC drive.

Space vector control consists of controlling the stator currents, as represented by a vector. This control is based on projections which transform a three-phase time and speed dependent

system into a two co-ordinate (d and q co-ordinates) time invariant system. These projections lead to a structure similar to that of a DC machine control. Space vector controlled machines need two constants as input references: the torque component (aligned with the q co-ordinate) and the flux component (aligned with d co-ordinate). As space vector control is simply based on projections, the control structure handles instantaneous electrical quantities. This makes the control accurate in every working operation (steady state and transient) and independent of the limited bandwidth mathematical model [4]. This transformation can be split into two steps:

- (a,b,c) $\Rightarrow$ (α,β) (the Clarke transformation) which outputs a two co-ordinate time variant system
- (α,β) $\Rightarrow$ (d,q) (the Park transformation) which outputs a two co-ordinate time invariant system

This is explained in the following two subsections.

C.1.1 Clarke Transformation

The first transformation, know as the Clarke transformation, is a transformation of the stationary three-phase system, respresented in the ABC reference frame, into a stationary orthogonal two-dimensional reference frame, called the $\alpha\beta0$ reference frame. A vector representation of the Clarke transformation is shown in Fig. C.1. The forward and reverse transformations between the ABC and the $\alpha\beta0$ reference frames are given in matrix form in (C.1.1) and (C.1.2) respectively. These transformations are given here for stator currents, but they apply to stator voltages and flux linkages as well.

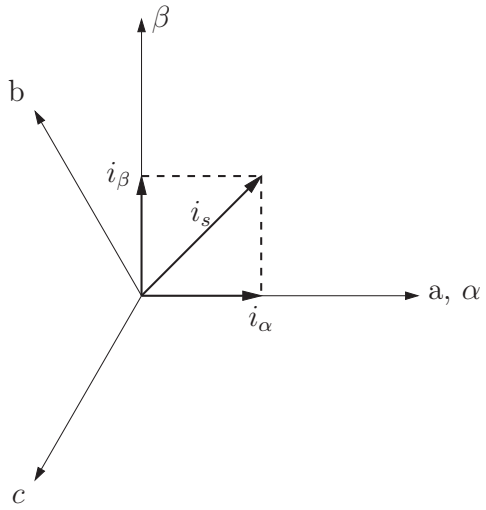

Figure C.1: Vector representation of the Clarke transformation.

$$\begin{bmatrix} i_\alpha \\ i_\beta \\ i_0 \end{bmatrix} = \frac{2}{3} \cdot \begin{bmatrix} 1 & -\frac{1}{2} & -\frac{1}{2} \\ 0 & \frac{\sqrt{3}}{2} & -\frac{\sqrt{3}}{2} \\ \frac{1}{2} & \frac{1}{2} & \frac{1}{2} \end{bmatrix} \cdot \begin{bmatrix} i_a \\ i_b \\ i_c \end{bmatrix} \tag{C.1.1}$$

$$\begin{bmatrix} i_a \\ i_b \\ i_c \end{bmatrix} = \begin{bmatrix} 1 & 0 & 1 \\ -\frac{1}{2} & \frac{\sqrt{3}}{2} & 1 \\ -\frac{1}{2} & -\frac{\sqrt{3}}{2} & 1 \end{bmatrix} \cdot \begin{bmatrix} i_\alpha \\ i_\beta \\ i_0 \end{bmatrix} \tag{C.1.2}$$

From Fig. C.1, the resultant vector of the $\alpha\beta$ vectors, $\overrightarrow{i_s}$, represents the peak value of the three-phase currents. Note that $\overrightarrow{i_s}$ does not contain the zero-sequence current. For a balanced set of three-phase currents, the zero-sequence current $i_0 = 0$.

The $\overrightarrow{i_s}$ vector in the $\alpha\beta$ reference frame is stationary; however, this vector is in actual fact rotating synchronously with the rotor at speed ω_r. Should a current vector controller be used to control $\overrightarrow{i_s}$ in the stationary reference frame, the bandwidth of the controller would have to be greater than the rotating speed, ω_r. This will introduce a phase shift in the current vector $\overrightarrow{i_s}$. It is therefore necessary to make a transformation from the stationary $\alpha\beta$ reference frame, to a rotating reference frame that is fixed to the rotor. This transformation is explained in the next section.

C.1.2 Park Transformation

The Park transformation is a transformation of the stationary $\alpha\beta$ reference frame into a rotating orthogonal two-dimensional reference frame, called the dq reference frame. A vector representation of this transformation is shown in Fig. C.2, with θ being the rotor flux position in electrical degrees. The current vector, $\overrightarrow{i_s}$, in this coordinate system, is fixed to the rotor at a position θ.

The forward and reverse transformations between the $\alpha\beta$ and dq reference frames are given in matrix form in (C.1.3) and (C.1.4) respectively. Again these transformations are given here for stator currents, but apply to stator voltages and flux linkages as well.

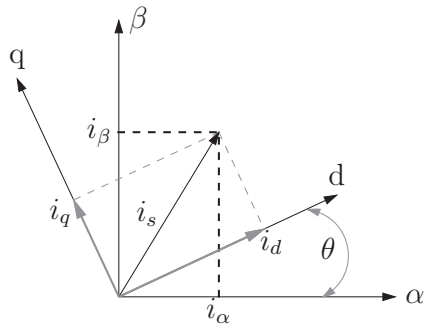

Figure C.2: Vector representation of the Park transformation.

$$\begin{bmatrix} i_d \\ i_q \\ i_0 \end{bmatrix} = \begin{bmatrix} cos\theta & sin\theta & 0 \\ -sin\theta & cos\theta & 0 \\ 0 & 0 & 1 \end{bmatrix} \cdot \begin{bmatrix} i_\alpha \\ i_\beta \\ i_0 \end{bmatrix} \tag{C.1.3}$$

$$\begin{bmatrix} i_\alpha \\ i_\beta \\ i_0 \end{bmatrix} = \begin{bmatrix} cos\theta & -sin\theta & 0 \\ sin\theta & cos\theta & 0 \\ 0 & 0 & 1 \end{bmatrix} \cdot \begin{bmatrix} i_d \\ i_q \\ i_0 \end{bmatrix} \tag{C.1.4}$$

C.2 Space Vector Pulse Width Modulation

Space vector pulse width modulation (SVPWM) makes it possible to simplify the control strategies used in a power electronic converter with an insulated neutral. To implement SVPWM, the instantaneous inverter output needs to be converted to the $\alpha\beta$-plane. This is done by using the Clarke transformation, as explained in subsection C.1.1. The converter states are shown in Fig. C.3. Each of the inverter outputs is referred to node G. This implies that on each of the phases the output can be either equal to the bus voltage or zero. In each phase the IGBTs are switched complementarily. It can be concluded that the output voltage vector of the converter can only be one of eight possible values at a given instant. The idea behind the implementation of SVPWM is to output the desired voltage presented in the $\alpha\beta$-plane plane by superimposing different output vectors onto each other over a modulation period. The average voltage over the modulation period is equal to the desired output voltage.

In Table C.1, the output voltage on each phase is shown for the different states.

State	V_{ag}	V_{bg}	V_{cg}
A	V_{dc}	0	0
B	V_{dc}	V_{dc}	0
C	0	V_{dc}	0
D	0	V_{dc}	V_{dc}
E	0	0	V_{dc}
F	V_{dc}	0	V_{dc}
G	V_{dc}	V_{dc}	V_{dc}
H	0	0	0

Table C.1: SVPWM state voltages.

The different vectors corresponding to each switching state are shown in Fig. C.4.
There are six vectors of the same length and two of zero length. It can be seen that adjacent vectors only differ by the switching of one phase arm at a time. The lengths of the six finite vectors are:

$$|\overline{V_A}| = |\overline{V_B}| = |\overline{V_C}| = |\overline{V_D}| = |\overline{V_E}| = |\overline{V_F}| = V_{dc} \tag{C.2.1}$$

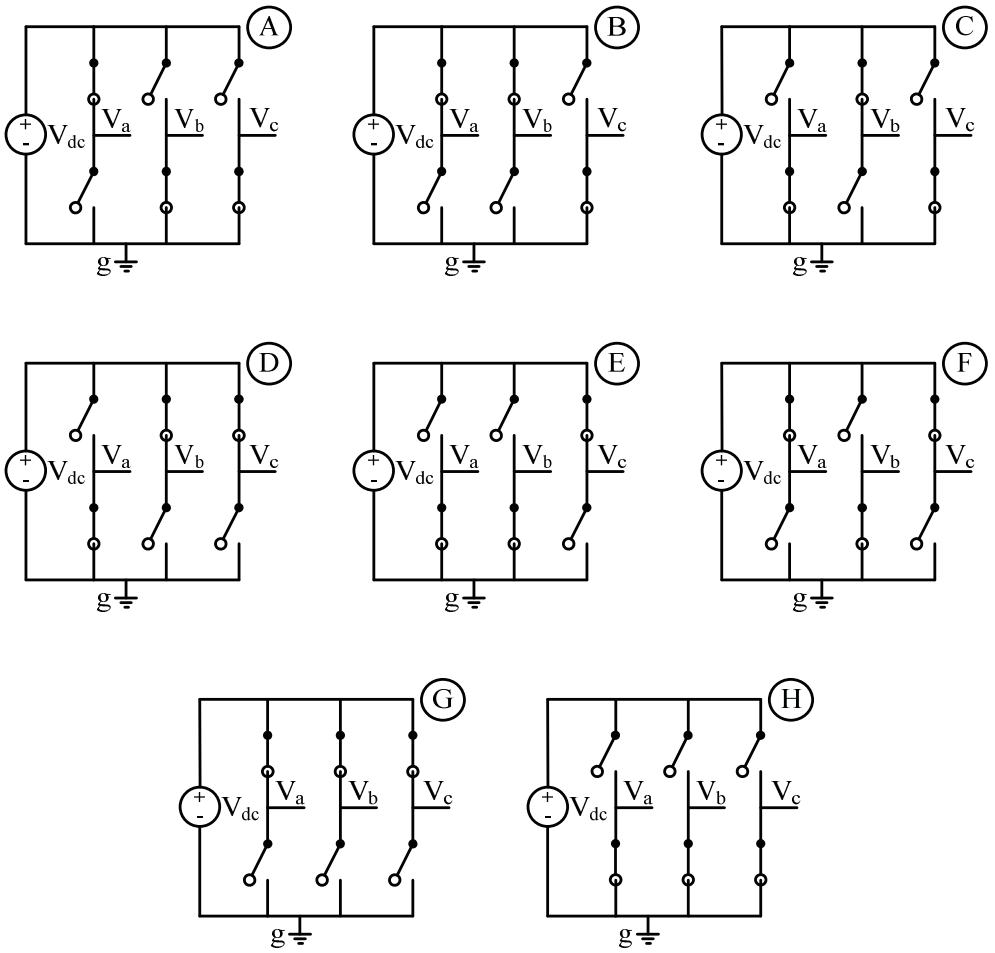

Figure C.3: SVPWM switching states

Also indicated in Fig C.4 are the six sectors within which the desired output vector can be located. To determine the optimal switching pattern it is necessary first to determine in which sector the output voltage is located. This is done by using a sequence of if- statements and some trigonometry. After the sector has been determined, another sequence of trigonometry calculations is done to calculate finally the required duty cycle of each phase that will result in the desired output voltage.

To minimise the amount of switching during a modulation period, an optimal switching period is needed. This can be achieved by noting that in each sector the desired voltage can be obtained by switching only the two vectors adjacent to that sector and two zero vectors. Further optimization can be obtained by switching these vectors in the correct sequence.

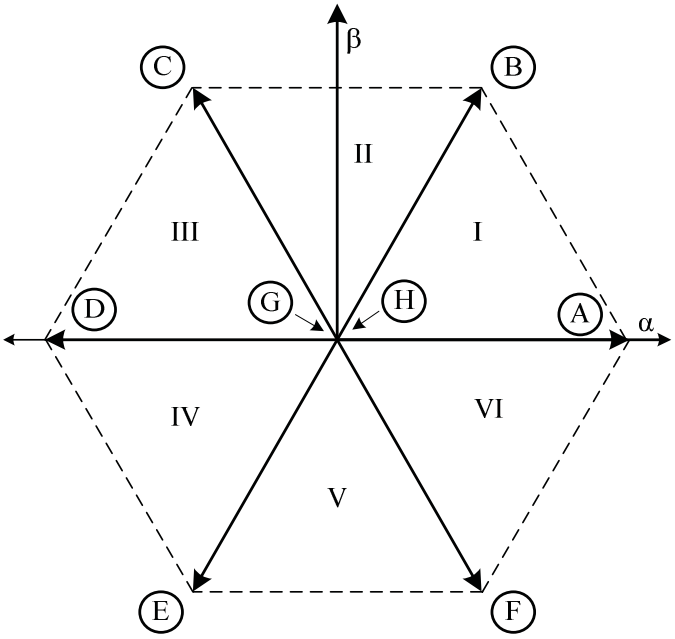

Figure C.4: Converter output vectors and sectors.

C.3 The basic scheme for vector control

The following diagram summarizes the basic scheme of space vector control:

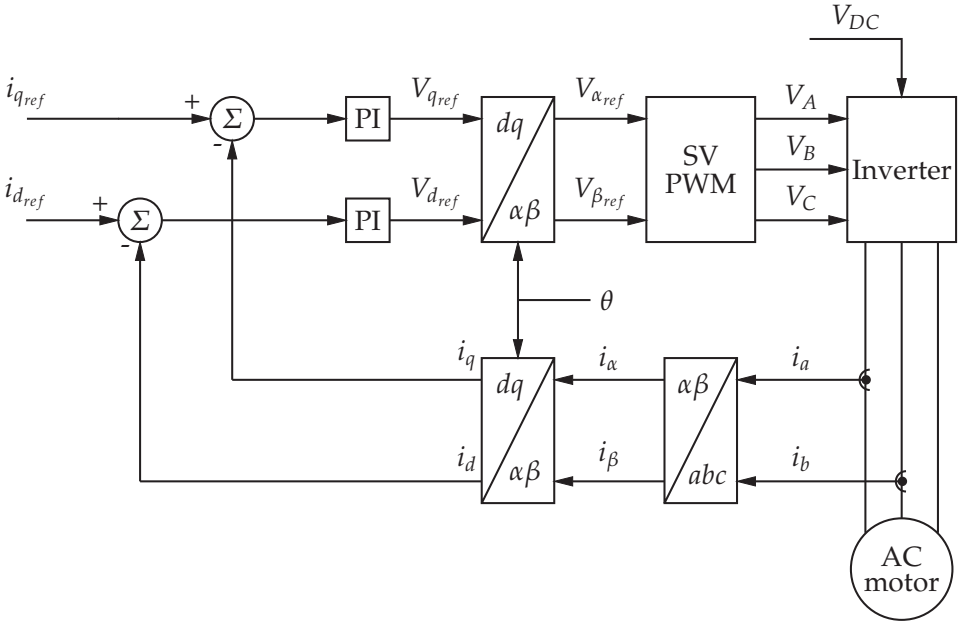

Figure C.5: Basic scheme of space vector control.

Two motor phase currents are measured. These measurements feed the Clarke transformation module. The outputs of this projection are designated i_α and i_β. These two components of the current are the inputs of the Park transformation that gives the current in the d,q rotating reference frame. The i_d and i_q components are compared to the references $i_{d_{ref}}$ (the flux reference) and $i_{q_{ref}}$ (the torque reference). At this point, this control structure shows an interesting advantage: it can be used to control either synchronous or induction machines by simply changing the flux reference and obtaining rotor flux position. As in synchronous permanent magnet motors, the rotor flux is fixed (determined by the magnets) and there is no need to create one. Hence, when controlling a PMSM, $i_{d_{ref}}$ should be set to zero. As induction motors need a rotor flux creation in order to operate, the flux reference must not be zero. This conveniently solves one of the major drawbacks of the "classic" control structures: the portability from asynchronous to synchronous drives. The torque command $i_{q_{ref}}$ could be the output of the speed regulator when we use a speed Space Vector Controller. The outputs of the current regulators are $v_{d_{ref}}$ and $v_{q_{ref}}$; they are applied to the inverse Park transformation. The outputs of this projection are $v_{\alpha_{ref}}$ and $v_{\beta_{ref}}$ which are the components of the stator vector voltage in the α,β stationary orthogonal reference frame. These are the inputs of the Space Vector PWM. The outputs of this block are the signals that drive the inverter.

Appendix D

Voltage, Current and Position measurements sensors

D.1 Voltage Transducer

The principal on which the transducer work is, a current proportional to the measured voltage must be passed through an external resistor R1. This is illustrated in Fig. D.1. This current is the primary current I_p which is transformed to the secondary to give a secondary current I_s which represents the DC bus voltage, V_{DC}, as a small current. From the datasheet

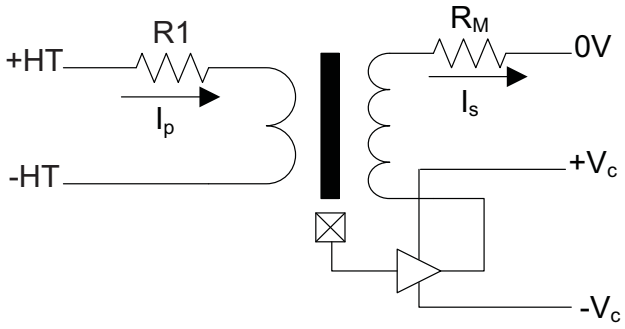

Figure D.1: Connection diagram of a LEM voltage transducer.

of the LV 25-P, it is stated that the nominal primary current $I_{p_{(nom)}}$ should be 10 mA_{RMS} to ensure accurate measurement. With the given winding ratio of $\frac{N1}{N2} = \frac{2500}{1000}$ the secondary nominal current $I_{s_{(nom)}}$ is 25 mA. Therefore, from Table 3.5, the nominal DC bus voltage is approximately 338 V, which yields $R1 = \frac{338}{10m} \approx 34k\Omega$. The measuring resistor, R_M, through which the secondary current passes should be chosen such that the minimum and maximum bus voltage that will be measured is represented by:

$$-1.5\ V \leq V_{measure} \leq 1.5\ V \tag{D.1.1}$$

The reason for the constraint given by (D.1.1) is that the ADC channels on the DSP needs an input voltage of $0V \leq V_{ADC} \leq 3V$. The voltage for the ADC channel is then obtained

by passing the output voltage of the transducer through an OP-AMP level shifting circuit with unity gain, such that $V_{ADC} = V_{measure} + 1.5V$. Considering a maximum bus voltage, as specified in Table 3.5, of 425 V the maximum secondary current will be

$$\begin{aligned} I_{s_{max}} &= \frac{V_{DC_{max}}}{R1} \times \frac{N_1}{N_2} \\ &= 31.25 \text{ mA} \end{aligned} \tag{D.1.2}$$

To adhere to the constraint given by (D.1.1), the measuring resistor R_M can be calculated as

$$\begin{aligned} R_M &= \frac{V_{measure}}{I_{s_{max}}} \leq 1.5V \\ \Rightarrow R_M &\leq 52.8\ \Omega \end{aligned} \tag{D.1.3}$$

From (D.1.2) and (D.1.3), the maximum secondary voltage that will be measured by the DSP will be

$$\begin{aligned} V_{measure} &= 52.8 \times 0.03125 \\ &= 1.5 \text{ V} \end{aligned} \tag{D.1.4}$$

which adheres to the constraint given by (D.1.1). Therefore, for a minimum DC bus voltage of -425 V the minimum secondary voltage that will be measured by the DSP will be -1.5 V, which also adheres to the constraint given by (D.1.1). Finally, the digital representation of the DC bus voltage can be expressed as:

$$V_{DC_{(dig)}} = V_{DC} \left\{ \ \tfrac{1}{R1} \cdot \tfrac{2500}{1000} \ \right\} R_M + 1.5 \tag{D.1.5}$$

D.2 Current Transducer

A basic connection diagram of the current transducer is depicted in Fig. D.2. As opposed to the voltage transducer, the conductor carrying the current to be measured is passed through a hole in the transducer. The current transducer uses the Hall effect to measure the magnetic field induced by the current carrying conductor. A current, I_p, is induced on the primary side of the transducer, due to the magnetic field induced by the current flowing in the conductor, and is transformed to the secondary side of the transducer to give a secondary current, I_s, of As listed in Table 4.3, the maximum phase current, $I_{p_{max}}$, that needs to be measured is 137.6 A. With the winding ratio of the current transducer given as $\frac{N1}{N2} = \frac{1}{5000}$, the secondary current which represents the measured current is given as

$$\begin{aligned} I_{s_{max}} &= I_{p_{max}} \cdot \frac{N1}{N2} \\ &= 28\ mA_{peak} \end{aligned} \tag{D.2.1}$$

As with the voltage transducer the measuring resistor, R_M, through which the secondary current passes should be chosen to adhere to the constraint given by (D.1.1). The measuring resistor is calculated as

$$\begin{aligned} R_M \times I_{s_{max}} &\leq 1.5 \\ \Rightarrow R_M &\leq 53.6\ \Omega \end{aligned} \tag{D.2.2}$$

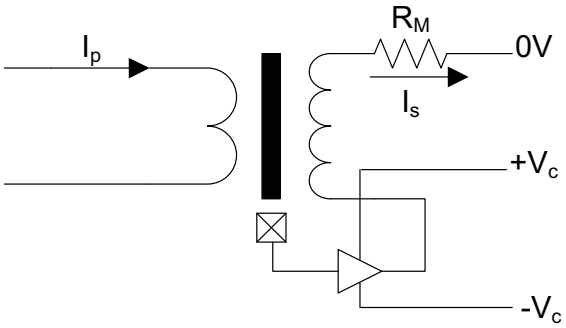

Figure D.2: Connection diagram of a LEM current transducer.

From (D.2.1) and (D.2.2), the maximum voltage that will be measured by the DSP is

$$\begin{aligned} V_{measure} &= 53.6 \times 0.028 \\ &= 1.5 \text{ V} \end{aligned} \tag{D.2.3}$$

which adheres to the constraint given by (D.1.1). Therefore, for a minimum phase-current of -140 A, the minimum secondary voltage that will be measured by the DSP is -1.5 V which also adheres to the constraint given by (D.1.1). Finally, the digital representation of the measured current can be expressed as,

$$I_{peak_{(dig)}} = I_{(peak)} \left\{ \ \tfrac{1}{5000} \times R_M \ \right\} + 1.5 \tag{D.2.4}$$

D.3 Operation of resolver position measurement sensor

The primary winding of the resolver needs to be excited with a sinusoidal AC reference signal. The reference signal can be described by eqn. (D.3.1). The amplitude of subsequent coupling onto the secondary stator windings is a function of the position of the rotor relative to the stator. The resolver produces two output voltages which are modulated by the sine and cosine of the shaft angle. As with any transformer, the resolver has a transformation ratio (TR) between its primary and secondary windings, and is specified at the point of maximum coupling between the primary and secondary. The modulated secondary winding equations can be described by eqns. (D.3.2) and (D.3.3). Since every angle within a 360° revolution has a unique combination of sine and cosine values, the resolver provides absolute position information of its rotor.

$$V_r = V_p \sin(\omega t) \tag{D.3.1}$$

$$V_\alpha = S3 - S1 = V_r \cdot TR \cdot \cos(\theta) = V_s \times \sin(\omega t) \times \sin(\theta) \tag{D.3.2}$$

$$V_\beta = S2 - S4 = V_r \cdot TR \cdot \sin(\theta) = V_s \times \sin(\omega t) \times \cos(\theta) \tag{D.3.3}$$

Fig. D.3 shows the resolver's excitation signal along with the corresponding secondary sine and cosine outputs generated, as a result of the resolver shaft rotating.

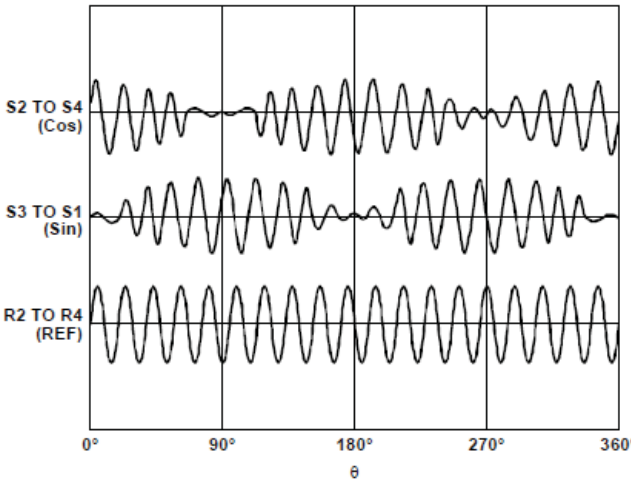

Figure D.3: Resolver format signal representation [4].

Rotor angle and speed extraction

To extract the rotor angle and speed from the resolver's output signals, given by (D.3.2) and (D.3.3), a trigonometric approached is used. This method requires a fast and high accuracy measurement of the output signals. For an accurate rotor angle estimation, the output signals should be sampled simultaneously and close to their period peaks. The shaft angle can thereby be determined by an inverse tangent function of the secondary output voltages as follows

$$\theta = atan\left(\frac{V_\alpha}{V_\beta}\right) \tag{D.3.4}$$

The rotor speed is obtained by differentiating eqn. (D.3.4). The rotor speed can therefore be determined as

$$\omega = \frac{d\theta}{dt} \tag{D.3.5}$$

Appendix E

Source Code Listings

E.1 RFAPM machine design script

```
#!/usr/bin/env python

#import wx
import sys
import os

import pylab
from numpy import *
#from Numeric import *
from math import *
from decimal import *
from scipy import *

PL = pylab

#*****************************************************************************
#                        Global variables & constants:
#*****************************************************************************
P_out_m = 30000.0          #maximum power output of electrical motor
eff = 0.98                          #motor efficiency
B_p = 0.56                          #airgap flux density
Y_cu = 8900.0                  #copper density
Y_NdFeB = 7500.0           #Neodymium Iron Boron density
k_d = 1.0                           #distribution factor = 1 for conventional
    machines
poles = 24.0                   #number of poles
rpm = 4800                          #rated motor speed
freq = (rpm*poles)/120     #calculate the motor output frequency

E_p = 169.7065             #estimation of peak sinusoidal phase voltage

theta_m = (4.0*pi)/3.0     #active coil angle (electrical)
Q = (pi*poles)/theta_m     #number of stator coils
q = Q/3.0                  #number of stator coils per phase
```

```
35 h = 0.0080                          #radial thickness of coil winding
36 l = 0.0                             #length of coils
37 r = 0.0                             #radius of stator
38 a = q                               #number of parallel circuits (max)

40 t = 0.1                             #dummy variable
41 tau = 0.0                           #dummy variable

43 k_f = 0.42                              #copper filling factor
44 Rho_t = 0.0000000215    #resistivity of copper

46 r_1 = 0.0                           #inner rotor radius
47 tau_w = 0.0                         #inner rotor magnet width
48 tau_p = 0.0                         #inner rotor magnet spacing

50 r2 = 0.0             #outer rotor radius
51 tau_w2 = 0.0         #outer rotor magnet width
52 tau_p2 = 0.0         #outer rotor magnet spacing

54 k_c = []                            #optimization factor for theta_r array
55 k_pc = []                           #pitch factor
56 k_w = []                            #winding factor
57 k_e = []                            #end turn winding factor
58 k_m = []

60 theta_r = []                        #radial angle of coil width (electrical)

62 w = (rpm*2.0*pi)/60.0   #mechanical rotational speed in rad/s (4800 rpm)
63 w_e = w*(poles/2.0)                 #electrical ratational speed in rad/s

65 delta_c = []

67 P_cu = ((1.0 - eff)/eff)*P_out_m         #copper losses

69 k_c = arange(t, 0.5, 0.01)           #kappa

71 kappa = 22

73 theta_r = k_c*theta_m                #calculate radial angle of coil width
       (electrical)

75 air_gap = 0.001                         #air gap

77 N_p = 30                         #number of parallel conductors

79 ##########################################################################
80 #   Calculate magnet width and magnet spacing of inner rotor
81 ##########################################################################
82 l_ipg = tau_p - tau_w    #inner rotor interpolar gap length

84 l_g = h + 2*air_gap      #gap length

86 h_m = 0.004
```

```
88  #while h_m<(l_g/2):
89  #    h_m = h_m+0.000001                #PM height

91  while l_ipg<(l_g/2):
92     while r < 0.117:
93        r1 = ((r - h/2) - h_m - air_gap) #inner rotor radius
94        r = r+0.000001                   #stator radius
95        tau_w = (0.7*2*pi*r1)/poles      #inner rotor PM width
96        tau_p = (2*pi*r1)/poles          #inner rotor shoe-pole width
97        l_ipg = tau_p - tau_w            #inner rotor interpolar gap length

99  ratio = tau_w/tau_p

101 d = 2.0*r                            #diameter of stator

103 ##########################################################################
104 #    Calculate magnet width and magnet spacing of outer rotor
105 ##########################################################################
106 r2 = ((r + h/2) + h_m + air_gap)     #gap length

108 tau_w2 = (0.7*2*pi*r2)/poles         #outer rotor PM width

110 tau_p2 = (2*pi*r2)/poles             #outer rotor shoe-pole width

112 l_ipg2 = tau_p2 - tau_w2             #outer rotor interpolar gap length

114 ratio2 = tau_w2/tau_p2

116 if l_ipg2 < (l_g/2):
117     print "Interpolar gap length constraint for outer rotor not met"

119 ##########################################################################
120 #                        Calculate k_pc, M_cu, T_d
121 ##########################################################################
122 while t < 0.5:
123         k_pc.append((2.0*sin((theta_m/2.0)*(1.0 -
               t))*sin(theta_m*t/2.0))/(t*theta_m))
124         t = t + 0.01

126 k_w = multiply(k_pc,k_d)*sqrt((pi*k_c)/3.0)     #calculate winding factor
127 k_w_tmp = k_w[kappa]

129 T_d = 0.0

131 while T_d < 69.5:
132    l = l+0.000001
133    delta_c_tmp = ((2.0*pi*d)/(Q*l))*(1.0 - (0.586*k_c[kappa]))
134    k_e_tmp =  power((2.0 + delta_c_tmp), (-0.5))
135    C_1_tmp = B_p*sqrt((1.5*l*h*k_f*P_cu*(d ** 3.0))/Rho_t)
136    T_d = k_w_tmp*k_e_tmp*C_1_tmp

138 delta_c = ((2.0*pi*d)/(Q*l))*(1.0 - (0.586*k_c))

140 k_e = power((2.0 + delta_c), (-0.5))
```

```
142 C_1 = B_p*sqrt((1.5*l*h*k_f*P_cu*(d ** 3.0))/Rho_t)

144 k_m = pi*k_c

146 C_2 = h*d*k_f*l*Y_cu

148 M_cu = pi*k_c*(2.0 + delta_c)*C_2       #calculate total copper mass

150 T_d_tmp = k_w*k_e*C_1

152 ##############################################################################
153 #                        Calculate number of turns required
154 ##############################################################################
155 N_tmp = (E_p*a*poles)/(multiply((q*4.0*B_p*r*l*k_d*w_e), k_pc))

157 N = N_tmp[kappa]         #number of turns at k_c = 0.4
158 #N = 36.0
159 #E_p = (N*q*4.0*B_p*r*l*k_d*w_e*k_pc[kappa])/(a*poles)  #calibration of peak
        phase voltage
160 E_p_Rated = E_p/sqrt(2)

162 #calculate required copper wire diameter
163 W = (2.0*r*theta_r)/poles       #coil width

165 A_c = (h*W*k_f)/N

167 Diameter_wire = sqrt(A_c*(4/pi))        #minimum diameter of the copper wire

169 ##############################################################################
170 #Calculate flux-linkage, induced coil voltage, phase resistance, phse current
171 ##############################################################################
172 l_ec = (4.0*r*theta_m/poles)*(1.0 - (0.586*k_c))   #end-turn length

174 for t in range (1, 20):
175     #calculate single turn flux linkage at delta=0
176     lambda_s = (4.0/poles)*B_p*r*l*sin(theta_m/2.0)*sin((w_e*t) + (theta_m/2.0))

178     #induced coil voltage
179     e_c = (4.0/poles)*B_p*r*l*N_tmp*k_pc*w_e*cos((w_e*t) + (theta_m/2.0))

181     #calculate flux linkage of coil with N = mxn turns
182     #lambda_c = (4.0/poles)*B_p*r*l*N*k_pc*sin((w_e*t) + (theta_m/2.0))

184 R_ph = ((N_tmp**2)*q*Rho_t*((2.0*l + l_ec)))/((a**2)*k_f*h*W)   #phase
        resistance

186 R_ph_tmp = ((N**2)*q*Rho_t*((2.0*l + l_ec[kappa])))/((a**2)*k_f*h*W[kappa])
        #phase resistance

188 I_p = sqrt((2*P_cu)/(3*R_ph))   #peak sinusoidal phase current

190 I_p_tmp = sqrt((2*P_cu)/(3*R_ph_tmp))   #peak sinusoidal phase current
```

```
192 I_p_Rated = I_p_tmp/(sqrt(2))   #per phase rms current

194 ##########################################################################
195 #                    Calulate current density
196 ##########################################################################
197 Area_conductor = pi*(((Diameter_wire[kappa]*1000)/2)**2)    #calculate area of
        conductor

199 CurrentDensity = I_p_Rated/(Area_conductor*a)

201 ##########################################################################
202 #   Calulate power losses in machine due to Eddy-currents
203 ##########################################################################
204 A_conductor = pi*(Diameter_wire[kappa] ** 2)/4   #area of conductor
205 N_p_conductor = sqrt((A_conductor*4)/(N_p*pi))   #diameter of parallel conductor
206 P_e =
        N_p*1.75*2*Q*N*((pi*l*(N_p_conductor)**4)*(B_p**2)*((2*pi*freq)**2))/(32*Rho_t)
        #calculate eddy currents

208 #for index, value in enumerate(k_c):
209 #   print index, value

211 ##########################################################################
212 #                    Calculate total magnet mass
213 ##########################################################################
214 M_magnets = (Y_NdFeB*tau_w*h_m*l*poles) + (Y_NdFeB*tau_w2*h_m*l*poles)

216 ##########################################################################
217 #                    Power calculations
218 ##########################################################################
219 P_out = 3*E_p_Rated*I_p_Rated  #calculate the output power of the motor
220 P_in = P_out+P_cu+P_e       #calculate the total input power
221 eff_f = (P_out/P_in)*100    #calculate total efficiency of motor

223 ##########################################################################
224 #                              Plot
225 ##########################################################################
226 PL.figure()
227 PL.subplot(111)
228 PL.plot(k_c, (1000.0*Diameter_wire))
229 PL.xlabel(r' Optimization factor for $\theta_r$ array')
230 PL.ylabel('Required copper wire diameter [mm]')
231 PL.title(r' Require copper wire diameter against $k_c$')

233 PL.grid(True)

235 PL.figure()
236 PL.subplot(211)
237 PL.plot(k_c, I_p)
238 PL.title(r' Peak phase current and phase resistance against the optimization
        factor $k_c$')
239 PL.xlabel(r' Optimization factor for $\theta_r$ array')
240 PL.ylabel('Peak phase current [A]')
```

```
242 PL.grid(True)

244 PL.subplot(212)
245 PL.plot(k_c, R_ph)
246 PL.xlabel(r' Optimization factor for $\theta_r$ array')
247 PL.ylabel('Phase resistance')

249 PL.grid(True)

251 PL.figure()
252 ax1 = PL.subplot(111)

254 PL.plot(k_c, M_cu)

256 PL.hold(True)

258 PL.xlabel(r' Optimization factor for $\theta_r$ array')
259 PL.ylabel('Total copper mass [Kg]')

261 ax = PL.gca()
262 ax2 = PL.gcf().add_axes(ax.get_position(), sharex=ax, frameon=False)
263 ax2.yaxis.set_label_position('right')
264 ax2.yaxis.tick_right()

266 PL.plot(k_c, T_d_tmp, 'r')
267 PL.ylabel('Developed torque [N.m]')

269 ax2.yaxis.tick_right()

271 PL.title(r' Total copper mass and the developed torque againt $k_c$')
272 PL.grid(True)

274 PL.figure()
275 PL.subplot(211)
276 PL.plot(k_c, k_e)
277 PL.ylabel(r' $k_e$ factor')
278 PL.xlabel(r' Optimization factor for $\theta_r$ array')

280 PL.grid(True)

282 PL.subplot(212)
283 PL.plot(k_c, k_w)
284 PL.ylabel(r' $k_w$ factor')
285 PL.xlabel(r' Optimization factor for $\theta_r$ array')

287 PL.grid(True)

289 ##########################################################################
290 #       Print motor specifications to latex file
291 ##########################################################################
292 fl = file('specifications.tex', 'w')

294 print >> fl, "Rated power output & %.0f & kW \\\\" %(P_out_m/1000)
295 print >> fl, "Rated efficiency & %.2f & \\\\" %(eff)
```

```
296 print >> fl, "Rated motor speed & %d & rpm \\\\" %(rpm)
297 print >> fl, "Motor frequency & %d & Hz \\\\" %(freq)
298 print >> fl, "Peak phase voltage & %.2f & V \\\\" %(E_p)
299 print >> fl, "Phase voltage & %.2f & $V_{RMS}$ \\\\" %(E_p_Rated)
300 print >> fl, "\\\\"
301 print >> fl, "Density of copper & %.2f & $g/{mm}^3$ \\\\" %(Y_cu)
302 print >> fl, "Density of Neodymium Iron Boron & %.2f & $g/{mm}^3$ \\\\"
        %(Y_NdFeB)
303 print >> fl, "\\\\"
304 print >> fl, "Number of poles & %d & \\\\" %(poles)
305 print >> fl, "Number of stator coils & %d & \\\\" %(Q)
306 print >> fl, "Number of stator coils per phase & %d & \\\\" %(q)
307 print >> fl, "Number of parallel circuits & %d & \\\\" %(a)
308 print >> fl, "\\\\"
309 print >> fl, "Airgap flux density & %.2f & \\\\" %(B_p)
310 print >> fl, "Copper filling factor & %.2f & \\\\" %(k_f)
311 print >> fl, "Distribution factor & %d & \\\\" %(k_d)

313 fl.close()

315 ##############################################################################
316 #                Print all dimensions to latex file
317 ##############################################################################
318 fl = file('dimensions.tex', 'w')

320 print >> fl, "Pitch factor($k_{pc}$) & %.3f & \\\\" %(k_pc[kappa])
321 print >> fl, "Kappa($k_c$) & %.2f & \\\\" %(k_c[kappa])
322 print >> fl, "End-turn winding factor($k_e$) & %.3f & \\\\" %(k_e[kappa])
323 print >> fl, "Copper mass factor($k_m$) & %.2f & \\\\" %(k_m[kappa])
324 print >> fl, "Delta($\delta_c$) & %.4f & \\\\" %(delta_c[kappa])
325 print >> fl, "$C_1$ & %.4f & \\\\" %(C_1)
326 print >> fl, "$C_2$ & %.4f & \\\\" %(C_2)
327 print >> fl, "\\\\"
328 print >> fl, "Radial thickness of coil winding (h) & %.2f & mm \\\\" %(h*1000)
329 print >> fl, "Length of coils (l) & %.2f & mm \\\\" %(l*1000)
330 print >> fl, "Active coil angle ($\\theta_m$) & %.2f & rad \\\\" %(theta_m)
331 print >> fl, "Radial angle of coil width ($\\theta_r$) & %.2f & rad \\\\"
        %(theta_r[kappa])
332 print >> fl, "Width of coils (w) & %.2f & mm \\\\" %(W[kappa]*1000)
333 print >> fl, "Total end-turn length of coils & %.2f & mm \\\\"
        %(l_ec[kappa]*1000)
334 print >> fl, "Radius of stator (r) & %.2f & mm \\\\" %(r*1000)
335 print >> fl, "Airgap & %.2f & mm \\\\" %(air_gap*1000)
336 print >> fl, "Gap length ($l_g$) & %.2f & mm \\\\" %(l_g*1000)
337 print >> fl, "\\\\"
338 print >> fl, "Copper wire diameter & %.2f & mm \\\\"
        %(Diameter_wire[kappa]*1000)
339 print >> fl, "Number of turns per coil & %d & \\\\" %(N)
340 print >> fl, "Number of parallel conductors & %d & \\\\" %(N_p)
341 print >> fl, "Diameter of parallel conductors & %.3f & mm \\\\"
        %(N_p_conductor*1000)
342 print >> fl, "\\\\"
343 print >> fl, "Rotor magnet height ($h_m$) & %.2f & mm \\\\" %(h_m*1000)
344 print >> fl, "\\\\"
```

```
345 print >> fl, "Inner rotor magnet width & %.2f & mm \\\\" %(tau_w*1000)
346 print >> fl, "Inner rotor radius & %.2f & mm \\\\" %(r1*1000)
347 print >> fl, "Ratio of ($\\tau_p$) to ($\\tau_m$) of inner rotor & %.2f & \\\\"
        %(ratio)
348 print >> fl, "\\\\"
349 print >> fl, "Outer rotor magnet width & %.2f & mm \\\\" %(tau_w2*1000)
350 print >> fl, "Outer rotor radius & %.2f & mm \\\\" %(r2*1000)
351 print >> fl, "Ratio ($\\tau_p$) to ($\\tau_m$) of outer rotor & %.2f & \\\\"
        %(ratio2)

353 fl.close()

355 ##########################################################################
356 #               Print output parameters to latex file
357 ##########################################################################
358 fl = file('parameters.tex', 'w')

360 print >> fl, "Developed torque & %.2f & N.m \\\\" %(T_d_tmp[kappa])
361 print >> fl, "Phase resistance & %.3f & $\Omega$ \\\\" %(R_ph_tmp)
362 print >> fl, "Peak phase current & %.2f & A \\\\" %(I_p[kappa])
363 print >> fl, "Phase current & %.2f & $A_{RMS}$ \\\\" %(I_p_Rated)
364 print >> fl, "Induced coil voltage & %.2f & V \\\\" %(e_c[kappa])
365 print >> fl, "\\\\"
366 print >> fl, "Total copper losses & %.2f & W \\\\" %(P_cu)
367 print >> fl, "Eddy current losses & %.2f & W \\\\" %(P_e)
368 print >> fl, "Current density & %.2f & $A_{RMS}/{mm}^2$ \\\\" %(CurrentDensity)
369 print >> fl, "\\\\"
370 print >> fl, "Total input power & %.2f & Kw\\\\" %(P_in/1000)
371 print >> fl, "Total output power of motor & %.2f & Kw \\\\" %(P_out/1000)
372 print >> fl, "Motor efficiency & %.1f & \\\\" %(eff_f)
373 print >> fl, "\\\\"
374 print >> fl, "Total copper mass & %.3f & kg \\\\" %(M_cu[kappa])
375 print >> fl, "Total mass of NdFeB magnets & %.2f & kg \\\\" %(M_magnets)

377 fl.close()

379 #os.system('pdflatex /home/davidg/Documents/Motor_Specificaions.tex')
380 #os.system('kpdf Motor_Specificaions.pdf &')

382 #PL.show()
```

E.2 Resolver Position and Speed Calculation

```
1 /*
2         File Name       :       Resolver.c
3         Description     :       In this file the rotor position and speed is
              calculated.
4         Programmer      :       Ivan Hobbs and David Groenewald
5         Date Created:   21-Aug-2010
6 */

8 #include "DSP2833x_Device.h"     // DSP2833x Headerfile Include File
9 #include "variables.h"
```

```
10 #include "controlcmd.h"
11 #include "Mode.h"
12 #include "Math.h"
13 #include "setupSPI.h"

15 int32 dtime = 10;

17 void readResolver(){

19         clearSample();
20         ResolverDelay(dtime);

22         setRD();                //Disable output buffer
23         ResolverDelay(dtime);

25         setRDVel();             //Select Angular Position Register
26         ResolverDelay(dtime);

28         clearRD();              //Transfer position data to output buffer
29         ResolverDelay(dtime);

31    // Sample angular position from resolver-to-digital chip
32         Position = (GpioDataRegs.GPBDAT.all&0xFFF00000)>>20;

34         ResolverDelay(dtime);

36         setRD();                //Disable output buffer
37         ResolverDelay(dtime);

39         clearRDVel();   //Select Velocity Register
40         ResolverDelay(dtime);

42         clearRD();              //Transfer angular data to output buffer
43         ResolverDelay(dtime);

45    // Sample angular speed from resolver-to-digital chip
46         Velocity = (GpioDataRegs.GPBDAT.all&0xFFF00000)>>20;
47         ResolverDelay(dtime);

49         setSample();    //Reset data registers
50         ResolverDelay(dtime);

52    // Calculate speed
53         we = (4096-Velocity)*29.296875;
54         if(Velocity == 0) {we = 0;}
55         if(Velocity > RPM_Max) {Velocity = RPM_Max;}

57    // Calculate electrical rotor position
58         Position *= 12;
59         ePos_rad = fmod(Position, 4095);

61    // Scale electrical postion between 0-2pi
62         ePos_rad = ((double)(ePos_rad/4095))*6.28318531;
63 }
```

E.3 Variable Declarations for Current Controller

```
1  /*
2  File Name:              variables.c
3  Description:    General viriable declaration
4  Created on:             07/05/2010
5  Created by:             Ivan Hobbs & David Groenewald
6  */

8  #include "DSP2833x_Device.h"     // DSP2833x Headerfile Include File
9  #include "main.h"

11 int ClosedLoop = 0;

13 //Resolver Values
14 int32 Position          = 0;
15 int32 Velocity          = 0;
16 int32 RPM_Max           = 4800;

18 int32 mPos_rad          = 0;
19 double ePos_rad = 0.0;
20 double Pos_zero = 3.50741;
21 double we                       = 0.0;

23 //ADC Values
24 int32 Ia_adc            = 0;
25 int32 Ib_adc            = 0;
26 int32 Idc_adc           = 0;
27 int32 Vdc_adc           = 0;
28 int32 Accel_adc = 0;
29 int32 Brake_adc = 0;

31 //Actual Values
32 double mIa                      = 0.00;
33 double mIb                      = 0.00;
34 double mIc                      = 0.00;
35 double mIdc                     = 0.00;
36 double mVdc                     = 0.00;
37 double Iq_ref           = 0.00;
38 double Id_ref           = 0.00;
39 double mBrake           = 0.00;

41 //DQ Values
42 double Ialpha   = 0.0;
43 double Ibeta    = 0.0;
44 double Iq                = 0.0;
45 double Id                = 0.0;

47 Uint16 Duty_a = 1875;
48 Uint16 Duty_b = 1875;
49 Uint16 Duty_c = 1875;

51 /*****************************************************************************/
```

```
52 /*              Current controller varibles                                 */
53 /*************************************************************************/
54 double K          = 0.68;       // Q-axis current controller constant gain
       factor
55 double Lq         = 27e-6; // q-axis machine inductance
56 double Ld                  = 27e-6;     // d-axis machine inductance (same as
       q-axis)
57 double Rs                  = 0.024;     // Stator resistance
58 double QFlux      = 0.0;   // Q-axis flux
59 double DFlux       = 0.0;       // D-axis flux
60 double PMFlux      = 0.03;      // PM Flux
61 double Vq_control = 0.0;   // Q-axis output voltage from controller
62 double Vd_control = 0.0;   // D-axis output voltage from controller

64 //SPIA Variables
65 Uint16 sdata    = 0x0000;
66 double DAC_Data = 0.00;

68 //Digital-to-Anlalog converter variables
69 Uint16 DAC_Gain = 0x0003;

71 //Last 3 Error Codes
72 int Error1 = 0;
73 int Error2 = 0;
74 int Error3 = 0;

76 //Calibrate

78 double mIa_calsum       = 0;
79 double mIb_calsum       = 0;
80 double mVdc_calsum      = 0;

82 double mIa_offset       = 0;
83 double mIb_offset       = 0;
84 double mVdc_offset      = 0;

86 int cal_complete = 0;
87 int cal_count = 0;
```

E.4 Current Controller Algorithm

```
1 /*
2         File Name       :       controlCalc.c
3         Description     :       In this file the control calculation of the
              converter is executed.
4         Programmer      :       Ivan Hobbs and David Groenewald
5         Date Created:   13-Feb-2009
6 */

8 /*___File Headers___*/
9 #include "DSP2833x_Device.h"     // DSP2833x Headerfile Include File
10 #include "DSP2833x_Examples.h"   // DSP2833x Examples Include File
11 #include "variables.h"
```

```
12 #include "parm_const.h"
13 #include "math.h"
14 #include "space.h"
15 #include "Resolver.h"
16 #include "setupSPI.h"
17 #include "Mode.h"
18 #include "controlCalc.h"
19 #include "writeDAC.h"

21 /*___Dead Time Compensation Variables___*/
22 double  dtIa    = 0.00;
23 double  dtIb    = 0.00;
24 double  dtIc    = 0.00;

26 double  dtIAlpha = 0;
27 double  dtIBeta  = 0;

29 double fVdc        = 0.00;
30 double fIq_ref     = 0.00;
31 double OneBySq3 = 0.57735027;
32 double TwoBySq3 = 1.15470054;
33 double Iq_test     = 0.0;
34 double sample      = 0.0;

36 //---------------------------------------------------------------------------------------
37 double Vd_ref = 0.0;
38 double Vq_ref = 0.0;
39 double Va_ref = 0.0;
40 double Vb_ref = 0.0;
41 double Vc_ref = 0.0;
42 double V_min  = 0.0;
43 double V_max  = 0.0;

45 #define PI      (3.14159265359)
46 //---------------------------------------------------------------------------------------

48 /*___
49         This function executes the control algorithms.
50         ___*/
51 void controlCalc(){

53         readResolver();

55         GpioDataRegs.GPACLEAR.bit.GPIO19 = 1;

57         /*___Space Vector Calculations___*/
58         mVdc < 1.00 ? mVdc = 1.00 : mVdc;                          //To prevent
               devision by zero in the SV calculations
59         imVdc = 1.00/mVdc;
                 //Inverse of the grid voltage used for the Space Vector
               Calculations

61         fIq_ref         = 0.9*fIq_ref + 0.1*Iq_ref;   //LPF accelerator input
               with oversampling only used for testing with POT
```

```
63    // Calculate Ialpha and Ibeta
64          Ialpha = Space3d(mIa,mIb,mIc);
65          Ibeta  = Space3q(mIa,mIb,mIc);

67        // DQ-Transformation
68                  Id = (Ialpha*cos(ePos_rad) + Ibeta*sin(ePos_rad));
69                  Iq = (Ibeta*cos(ePos_rad) - Ialpha*sin(ePos_rad));

71                  // D-axis Controller
72                  DFlux = (Lq*Iq*we);
73                  Vd_control = ((Id_ref - Id)*K) - DFlux;

75                  // Q-axis Controller
76                  QFlux = (Ld*Id*we);
77                  Vq_control = (((fIq_ref - Iq)*K)) + (PMFlux*we) - QFlux;

79    // Calculate Valpha and Vbeta
80    rValpha = -1*(Vq_control*sin(ePos_rad)) + (Vd_control*cos(ePos_rad));
          // Calculate Valpha
81    rVbeta  =    (Vq_control*cos(ePos_rad)) + (Vd_control*sin(ePos_rad));   //
          Calculate Vbeta

83          // Calculate PWM duty cycles
84          SpaceVectorPWM();

86          }
87  }
```

Bibliography

[1] Xue, X.D., Cheng, K.W.E. and Cheung, N.C.: "Selection of Electric Motor Drives for Electric Vehicles". *AUPEC, paper P-170*, 2008.

[2] "Design and Analysis of Dual-Rotor Radial Flux Permanent Magnet Generator for Direct Coupled Stand-Alone Wind Energy Systems". Available at: `http://scribd.com/doc/27911253/Design-and-Analysis-of-Dual-rotor-Radial-Flux`.

[3] Randewijk, P.J., Kamper, M.J. and Wang, R.J.: "Analysis and Performance Evaluation of Radial Flux Air-Cored Permanent Magnet Machines with Concentrated Coils". *Power Electronics and Drive Systems, 2007. PEDS '07. 7th International Conference on, pp 189 - 195*, 27-30 Nov 2007.

[4] Europe, T.I.: Field orientated control of 3-phase ac-motors. Tech. Rep., 1998. Literature Number: BPRA073.

[5] Groves, T.A.: *"Conversion of a Gasoline Powered Car to an Electrical Vehicle"*. Master's thesis, University of New South Wales at the Australian Defence Force Academy, 2006.

[6] Husain, I.: *"Electric and Hybrid Vehicles, Design Fundamentals"*. CRC Press, 2003. ISBN 0-8493-1466-6.

[7] Prins, P.: "Controller Area Network Instrument Cluster Controller (for 2006 Model OPEL Corsa Lite)". Tech. Rep., University of Stellenbosch, 2008.

[8] Rossouw, F.G.: *"Analysis and Design of Axial Flux Permanent Magnet Wind Generator System for Direct Battery Charging Applications"*. Master's thesis, Stellenbosch University, December 2008.

[9] Gieras, J.F., Wang, R.J. and Kamper, M.J.: *"Axial Flux Permanent Magnet Brushless Machines"*. Kluwer Academic Publishers, 2004. ISBN 1-4020-2661-7.

[10] Wolf, M., du T Mouton, H., van der Merwe, J.W. and Koeslag, F.: "An investigation of switching and conduction losses in inverters under varying inductor ripple current". *Proceedings of the IEEE Africon Conference*, Sep 2009.

[11] de Kock, H.W.: *"Dynamic Control of the Permanent Magnet Assisted Reluctance Synchronous Machine with Constant Current Angle"*. Master's thesis, Stellenbosch University, 2006.

[12] Franklin, G.F., Powell, J.D. and Workman, M.: *"Digital Control of Dynamic Systems"*. 3rd edn.

[13] Stegmann, J.A. and Kamper, M.J.: "Design Aspects of Double-Sided Rotor Radial Flux Aircored Permanent Magnet Wind Generator". *ECCE, San Francisco USA*, 2009.